COORDINATION NON-INNOCENCE AND REDOX CHEMISTRY OF ANTIMONY LIGANDS

A Dissertation

by

JAMES STUART JONES

Submitted to the Office of Graduate and Professional Studies of
Texas A&M University
in partial fulfillment of the requirements for the degree of

DOCTOR OF PHILOSOPHY

Chair of Committee,	François P. Gabbaï
Committee Members,	Donald J. Darensbourg
	Oleg. V. Ozerov
	Jaime C. Grunlan
Head of Department,	Simon W. North

December 2016

Major Subject: Chemistry

ABSTRACT

The coordination chemistry of antimony-containing ligands has been historically understudied relative to phosphines and arsines due to the widely held perception that their properties varied little from their lighter congeners. Recent developments, however, have found that antimony ligands can display unique coordination and redox behavior which mimics that known for organoantimony species. Coordinated antimony centers can engage in secondary bonding interactions in which the incoming ligand can bind *trans* to the Sb-M bond or the Sb-R bond. This coordination non-innocent behavior bears potential utility in anion-sensing and tuning of the coordinated transition metal center. Transition metal stibine complexes also undergo two-electron redox chemistry, which can be localized at the metal or the antimony center. In the latter case, the resulting Sb(V) species can serve as a Z-type ligand to activate the coordinated transition metal center for electrophilic reactivity. With the future goal of further incorporating antimony-containing ligands into functional main group-transition metal heterobimetallic platforms for anion-sensing, catalysis, and other behaviors, the origin and consequences of their unique behavior must be further investigated.

In an effort to systematically investigate the coordination non-innocent behavior of antimony ligands, their complexes were compared to the analogous phosphorous and arsenic complexes. The effect of coordination non-innocent behavior on the Sb-M bond was also systematically studied. The redox behavior of transition metal stibines was further elucidated in a series of case studies. Finally, we provide proof of concept that

coordination-non innocent behavior in antimony ligands can be utilized to activate adjacent transition metal centers for electrophilic catalysis.

DEDICATION

For BWT

ACKNOWLEDGEMENTS

I am indebted to my high school chemistry teacher Pauline Crowling for sparking my interest in chemistry and setting me on the path that led to my graduate studies at Texas A&M University. Her enthusiasm for teaching and willingness to indulge my curiosity left an indelible mark on me.I would also like to thank my two undergraduate advisors, Dr. David Kranbuehl and Dr. Robert Pike. I am grateful to Dr. Kranbuehl for allowing me to gain my first collegiate research experience during my freshman year, which led me to pursue additional research opportunities throughout my undergraduate education. I thank Dr. Pike for being an excellent mentor and for introducing me to X-ray crystallography, in addition to encouraging me to pursue my graduate studies. I also would like to acknowledge Prof. Don Darensbourg, Prof. Jaime Grunlan, and Prof. Oleg Ozerov for sitting on my committee.

I have been very fortunate to have worked with exceptional colleagues in the Gabbaï group: Dr. Casey Wade, Dr. Haiyan Zhao, Dr. Tzu-Pin Lin, Dr. Iou-Sheng Ke, Dr. Kantapat Chansaenpak, Dr. Masato Hirai, Dr. Haifeng Yang, Dr. Baofei Pan, Dr, Kewei Huang, Dr. Boris Vabre, Dr. Daniel Tofan, Dr. Guillaume Bélanger-Chabot, Dr. Sumit Sahu, Lauren Leamer, Srobona Sen, Anna Marie Christianson, Ahmed Ali, Chang-Hong Chen, Mengxi Yang, Elham Tabei, Ying-Hao Lo, Di You, Gregory Day, and Christina Lollar. I would especially like to thank Dr. Casey Wade, Dr. Tzu-Pin Lin, and Dr. Iou-Sheng Ke for their mentorship and for laying the foundation upon which my dissertation

was built upon. I am also grateful for the assistance and patience of Dr. Lisa Pérez, who was always willing to discuss computational challenges I encountered during my studies.

I would like to acknowledge Texas A&M University, the Welch Foundation and the NSF for research funding during my studies. I would also like to thank the Texas A&M University Department of Chemistry for funding travel grants.

Finally, I am beholden to my advisor Prof. François Gabbaï for providing me the opportunity to pursue my doctoral studies in his group. His mentorship and patience have allowed me to grow immensely as a scientist during my time at Texas A&M University and buoyed me during challenging times during the course of my studies.

TABLE OF CONTENTS

Page

ABSTRACT ii

DEDICATION iv

ACKNOWLEDGEMENTS v

TABLE OF CONTENTS vii

LIST OF FIGURES x

LIST OF TABLES xvi

1. INTRODUCTION TO THE COORDINATION CHEMISTRY OF ANTIMONY-BASED LIGANDS 1

1.1 Introduction 1
1.2 Bonding properties of stibines 2
1.3 Antimony-based Z-type ligands 3
1.4 Coordination-noninnocence in antimony-transition metal complexes 12
1.5 Redox chemistry of antimony-transition metal complexes 16
1.6 Objectives 28

2. ORIGINS OF COORDINATION NON-INNOCENCE IN TRANSITION METAL STIBINE COMPLEXES 30

2.1 Introduction 30
2.2 Structural characterization of nickel trisphosphinylpnictine lantern complexes 32
2.3 Computational studies 37
2.4 Conclusions 43
2.5 Experimental section 44

3. ELECTRONIC EFFECTS OF COORDINATION NON-INNOCENCE IN TRANSITION METAL STIBINES 48

3.1 Introduction 48
3.2 Synthesis and anion exchange reactivity of a Pt-Sb lantern complex 50
3.3 Synthesis of a series of Pt-Sb lantern complexes separated by sequential fluoride addition. 53

3.4 Theoretical investigation into the perturbation of the Pt-Sb bond by fluoride binding.....62
3.5 Conclusions.....68
3.6 Experimental section.....68

4. PREPARATION AND CHARACTERIZATION OF GOLD (I) COMPLEXES FEATURING AN AMBIPHILIC PHOSPHINE-CHLOROSTIBINE LIGAND.....75

4.1 Introduction.....75
4.2 Synthesis and characterization of a phosphine-dichloroarylstibine ligand.....77
4.3 Coordination chemistry.....79
4.4 Computational studies on **30**, **31**, and **33**.....89
4.5 Two electron oxidation of a pendant antimony center.....91
4.6 Catalytic propargylamide cyclization.....95
4.7 Conclusions.....102
4.8 Experimental section.....103

5. REDOX AND ANION EXCHANGE CHEMISTRY OF A NICKEL STIBINE COMPLEX.....113

5.1 Introduction.....113
5.2 Synthesis of a zerovalent nickel complex.....114
5.3 Redox and anion exchange chemistry of a nickel stibine complex.....115
5.4 NBO analyses of **36**, **23**-Cl, and **38**.....121
5.5 Conclusions.....124
5.6 Experimental section.....125

6. COORDINATION NON-INNOCENCE OF A PLATINUM STIBORANYL COMPLEX.....131

6.1 Introduction.....131
6.2 Oxidation and subsequent bond metathesis of a divalent platinum stibine complex.....132
6.3 Fluoride binding studies.....135
6.4 Computational studies.....143
6.5 Conclusions.....147
6.6 Experimental details.....148

7. FORMAL PHOTOREDUCTIVE ELIMINATION OF A C-X BOND FROM A SB-PT HETEROBIMETALLIC PLATFORM.....153

7.1 Introduction.....153
7.2 Photoreductive formation of a C-X bond.....155
7.3 Conclusions.....159
7.4 Experimental section.....159

8. SUMMARY 161

8.1 Origins of coordination non-innocence in transition metal stibine complexes 161
8.2 Electronic effects of coordination non-innocence in transition metal stibine complexes 162
8.3 Preparation and characterization of gold (I) complexes featuring an ambiphilic phosphine-chlorostibine ligand 162
8.4 Redox and anion exchange chemistry of a nickel stibine complex 163
8.5 Coordination non-innocence of a platinum stiboranyl complex 164
8.6 Formal photoreductive elimination of a C-X bond from an Sb-Pt heterobimetallic platform 165

REFERENCES 167

LIST OF FIGURES

Page

Figure 1. Known complexes of antimony ligands. 2

Figure 2. Known types of ambiphilic complexes. 4

Figure 3. Synthesis of 1 and [2][PF_6]. 5

Figure 4. Coordination chemistry at the mercury center in $[2]^+$. 6

Figure 5. Structures of $[2]^+$ (left) and 2-I(right). 6

Figure 6. ELF plots for 1, $[2]^+$, and 2-I. 8

Figure 7. (left) Solid-state XANES spectrum of the Au L_3-edge of 1 compared to Au(III) and Au(I) reference compounds. (right) Solid-state XANES spectrum of the Hg L_3-edge of 2-I compared to a Hg(II) reference. 8

Figure 8. Reactions of 1 and $[2]^+$ with F^-. 9

Figure 9. Crystal structures of 1 (left) and its fluoride adduct $[1\text{-}F]^-$ (right). 10

Figure 10. Complexation of 3-R with (tht)AuCl. 11

Figure 11. Front and side view of the crystal structures of (a) 4 and (b) 5. 12

Figure 12. Illustration of the isolobal relationship between $[R_3SbX]^+$ and $[(R_3Sb)M]^+$. . 13

Figure 13. Synthesis of [8][BPh_4] and [8][BPh_4]. 14

Figure 14. (a) Colorimetric and geometric changes in $[9]^+$ upon binding fluoride to form 9-F. (b) Changes in ^{31}P and ^{19}F NMR upon formation of 9-F. (c) Changes in the absorption spectra of $[9]^+$ upon incremental addition of TBAF. . 15

Figure 15. Examples of redox reactions of transition metal stibido compounds described by Malisch and coworkers. 17

Figure 16. Possible two-electron oxidation products of $(R_3Sb)[M]$. 17

Figure 17. Synthesis and subsequent oxidation of 10-Cl. 18

Figure 18. (a) Front and side views of the crystal structures of 10-Cl (top) and 11 (bottom). (b) NBO plots of the principal Sb-Au interactions in 10-Cl (top) and 11 (bottom). 19

Figure 19. Oxidation of 4 and 5 by *o*-chloranil. 20

Figure 20. Synthesis and photoredox chemistry of 14. 21

Figure 21. (a) Absorption spectra obtained during the photolysis of 15, with an inset plot of quantum yield vs. DMBD concentration. (b) ^{31}P NMR spectra of the photolysis of 15. 22

Figure 22. Proposed activation of an $[L_2Au]^+$ fragment by oxidation at antimony. 23

Figure 23. Synthesis of [16][SbF_6]. 23

Figure 24. Synthesis of [18][SbF_6]. 25

Figure 25. Crystal structures of [16][SbF_6] (left) and [18][SbF_6] (right). 26

Figure 26. Scope of alkyne hydroaminations catalyzed by [18][SbF_6] 27

Figure 27. Possible binding modes of donors (D) to coordinated stibines. 31

Figure 28. Venanzi's synthesis of lantern complexes 21-23. 31

Figure 29. Structures of [21][Cl] (left), [22][Cl] (center), and 23-Cl (right). Relevant structural features are compiled in Table 3. 34

Figure 30. Plots of the calculated Ψ_1, Ψ_2, and Ψ_3 orbitals in $[21]^+$, $[22]^+$, and $[23]^+$ (isodensity value = 0.02). 38

Figure 31. Diagrams illustrating the Pimentel-Rundle three center (left) and donor-acceptor model (right) for linear three center bonding. 39

Figure 32. NLMO plots (isodensity value = 0.05) of the E-Ni bonds in $[21]^+$, $[22]^+$, and $[23]^+$. Hydrogen atoms are omitted, and selected phenyl groups are drawn in wireframe. 41

Figure 33. Ball-and-stick model of the model complex $[ClNi(PH_3)_3(SbH_3)]^+$, showing front (left) and top (right) views. 42

Figure 34. Changes in the energy levels of the Ψ_1 (top left), Ψ_2 (top right), and Ψ_3 (bottom left) orbitals upon increasing ∢C-E-C in the cations $[ClNi(PH_3)_3(EH_3)]^+$, where E = P, As, Sb. Changes in the composition of the

E-Ni NLMO as determined by NBO analysis upon increasing ∢C-E-C. (bottom right) 43

Figure 35. Change in Sb-Pd bond composition in $[9]^+$ and 9-F *per* Boys localization analysis. 48

Figure 36. Synthesis and anion exchange of 25-Cl as previously described by C. R. Wade.[80] 50

Figure 37. NLMO and QTAIM plots for 25-Cl and 25-F. 52

Figure 38. Synthesis of $[26]^{2+}$, $[27]^+$, and 28. 54

Figure 39. Solid state structure of $[26][SbF_6]_2$. 56

Figure 40. Solid state structure of $[27][SbF_6]$. 57

Figure 41. ^{31}P (top) and ^{19}F NMR spectra (bottom) of 28 in CD_2Cl_2. 60

Figure 42. Solid state structure of 28. 61

Figure 43. Extreme bonding descriptions of $[26]^{2+}$, $[27]^+$, and 28. 62

Figure 44. NLMO and QTAIM plots for $[26]^{2+}$, $[27]^+$, 28. 63

Figure 45. Contributing resonance structures for compounds $[26]^{2+}$, $[27]^+$, and 28. 65

Figure 46. General structure of an ambiphilic compound, featuring a Lewis basic functionality (L) and a Lewis acidic functionality (Z) connected by a linker. 75

Figure 47. Observed coordination modes of ambiphilic ligands 76

Figure 48. Synthesis of 29-Cl by redistribution reaction of 7 with $SbCl_3$. 77

Figure 49. Solid state structures of 29-Cl (left) and 29-Ph (right). 78

Figure 50. Synthesis of compound 30. 79

Figure 51 Structure of compound 30 81

Figure 52. $^{31}P\{^1H\}$ NMR spectrum of the 1:1 reaction mixture of 29-Cl and (tht)AuCl in CH_2Cl_2. 82

Figure 53. Synthesis of compounds 31 and 32. 83

Figure 54. Crystal structure of 31.....83

Figure 55. Extended solid state structures of 30 and 31.....85

Figure 56. Solid state structure of compound 32, shown as a monomeric unit (left) and the corresponding short contact dimer structure (right). 87

Figure 57. Synthesis of compound 33.....88

Figure 58. Structure of compound 33.....89

Figure 59. Principal Sb→Au (top) and Au→Sb (bottom) donor-acceptor interactions in 30 (left), 31 (center), and 33 (right) obtained from NBO analysis.....90

Figure 60. *o*-chloranil oxidations of Au-Sb complexes previously described by Wade[80] and Ke.[37] 92

Figure 61. Oxidation of 30 by *o*-chloranil.....92

Figure 62. Structure of compound 35.....94

Figure 63. Principal Au→Sb donor-acceptor interactions in 35 obtained from NBO analysis (isodensity value = 0.05). Hydrogen atoms are omitted, and selected groups are drawn in wireframe for clarity.....95

Figure 64. Typical activations of electrophilic gold (I) catalysts.....96

Figure 65. $Ph_3PAuCl/Cu(OTf)_2$-catalyzed enyne cyclization reported by Gandon. 97

Figure 66. Catalytic cyclization of propargylic amides by a zwitterionic aluminate-phosphine gold complex reported by Bourissou. 98

Figure 67. General scheme for the substrate-assisted abstraction of a gold-bound halide by a pendant antimony Lewis acid. 99

Figure 68. Synthesis of 36.....114

Figure 69. Structure of compound 36.....115

Figure 70. Oxidation of 36 to form 23-Cl. 116

Figure 71. Synthesis of 37 and from 23-Cl. 117

Figure 72. Structure of compound 37.....118

Figure 73. Structure of compound 38. 120

Figure 74. Examples of known zerovalent nickel complexes featuring a Z-type ligand. 121

Figure 75. NBO plots of the major Sb-Ni bonding interactions in compounds 36 and 23-Cl 122

Figure 76. NBO plots (isodensity value = 0.05) of the major Ni→Sb donor-acceptor interactions and their corresponding calculated second-order perturbation energies in 38. Hydrogen atoms are omitted, and some phenyl and the cyclohexyl rings are drawn in wireframe for clarity. 124

Figure 77. Synthesis of 41 from 39 described by Ke.[214] 132

Figure 78 Reaction of 39 with *o*-chloranil at low temperature. 133

Figure 79 Crystal structure of compound 40. 134

Figure 80. Sequential fluoride binding to 41 proposed by Ke.[214] 135

Figure 81 Treatment of compound 41 with KF in unbuffered water under biphasic conditions. 136

Figure 82. Crystal structure of 43-OH (left) and its extended structure (right) 137

Figure 83 $^{31}P\{^{1}H\}$ NMR spectra of the biphasic reaction of 41 in $CDCl_3$ with aqueous (Millipore purified, pH 5) KF at progressive mixing times. 139

Figure 84 $^{31}P\{^{1}H\}$ NMR spectra of the biphasic reaction of 41 in $CDCl_3$ with water (borate buffer, pH 9) at progressive mixing times. 140

Figure 85 $^{31}P\{^{1}H\}$ NMR spectra of the biphasic reaction of 41 in $CDCl_3$ with KF (10 eq.) in 0.1 M HCl at progressive mixing times. 141

Figure 86 Crystal structure of 42-F. 142

Figure 87. HOMO and LUMO orbitals (isodensity value = 0.05) of compounds 41, 42-F, and 43-OH. 144

Figure 88. NBO plots for the Sb-Pt interactions in 41 and 42-F. 145

Figure 89. Major d(Pt)→p(Sb) and p(O)→p(Sb) donor-acceptor interactions in 43-OH 146

Figure 90. Experimental and calculated (TD-DFT) UV–visible spectra of 41 (left) and 42-F (right) 147

Figure 91. Oxidation and photoreductive regeneration of 14 as reported by Yang.[70] ...153

Figure 92. Oxidation and photoreductive regeneration of 39 as reported by Ke.[214] 154

Figure 93. $^{31}P\{^{1}H\}$ NMR spectra of the reaction mixture at progressive time points during the photolysis of 44. 156

Figure 94. Speculated identity of compound 46 produced during the photolysis of 44.159

LIST OF TABLES

Page

Table 1. Tolman electronic parameters for sample series of phosphines, arsines, and stibines. 3

Table 2. Activities of selected gold catalysts for hydroamination. 24

Table 3. Selected structural features of [21][Cl], [22][Cl], and 23-Cl. 35

Table 4. Selected structural features of ligands 19, 20, and 7. 36

Table 5. Atomic contributions from chlorine, nickel, and the basal pnictogen center to the three principal orbitals describing the E-Ni-Cl system in $[21]^+$ and $[22]^+$, $[23]^+$. 39

Table 6. Natural charges, NLMO contributions, and Wiberg Bond Indices (WBI) for the E-Ni interactions in $[21]^+$, $[22]^+$, and $[23]^+$. 41

Table 7. Crystal data, data collections, and structure refinements for 7, 20. 46

Table 8. Crystal data, data collections, and structure refinements for [21][Cl] and [22][Cl]. 47

Table 9. Ni-Cl bond lengths in selected Ni lantern complexes. 49

Table 10. Selected features of the electron distribution function at bond critical points of 25-Cl and 25-F. 53

Table 11. Natural charges, NLMO contributions, and Wiberg Bond Indices (WBI) for the Sb-Pt interactions in $[26]^{2+}$, $[27]^+$, and 28. 63

Table 12. Selected features of the electron density distribution function at bond critical points of $[26]^{2+}$, $[27]^+$, and 28. 67

Table 13. Crystal data, data collections, and structure refinements for [**26**][SbF_6]$_2$, [**27**][SbF_6] and **28**. 74

Table 14. NBO deletion energies for the Sb→Au and Au→Sb interactions in 30, 31, and 33. 91

Table 15. Activities of selected gold catalysts in the cyclization of *N*-(prop-2-yn-1-yl)adamantine-1-carboxamide. 100

Table 16. Activities of selected gold catalysts and additives in the cyclization of *N*-(prop-2-yn-1-yl)adamantine-1-carboxamide. 101

Table 17. Activity of compound 31 in the cyclization of various propargylic amides. . 102

Table 18. Crystal data, data collections, and structure refinements for 29-Ph and 29-Cl. 110

Table 19. Crystal data, data collections, and structure refinements for 30 and 31..... 111

Table 20. Crystal data, data collections, and structure refinements for 32, 33, and 35.. 112

Table 21. Crystal data, data collections, and structure refinements for 36, 37, and 38.. 130

Table 22. Crystal data, data collections, and structure refinements for 40, 42-F, and 43-OH. 152

1. INTRODUCTION TO THE COORDINATION CHEMISTRY OF ANTIMONY-BASED LIGANDS[1]

1.1 Introduction

Antimony-based ligands are historically understudied relative to their lighter congeners. In the case of stibines, which comprise the most common class of antimony-based ligands, this neglect can be attributed to their weaker donicity and more fragile bonds to carbon, as well as the prevailing belief that their properties were not fundamentally different relative to phosphines.[1] Within the past 15 years, however, new studies have shown that antimony ligands display unique coordination and redox behavior, which mirrors the rich redox and Lewis acid chemistry of organoantimony species. While several varieties of both trivalent and pentavalent antimony ligands are known (Figure 1), this introduction will focus principally on the coordination and redox chemistry of stibine ligands. Much of this introduction also serves to review previous work from the Gabbaï group on antimony coordination chemistry in the context of introducing the unusual properties that these ligands possess.

[1] Reprinted in part with permission from, "Coordination- and redox-noninnocent behavior of ambiphilic ligands containing antimony"; Jones, J. S.; Gabbaï, F. P. *Acc. Chem. Res.* **2016**, *49*, 857, Copyright 2016 by the American Chemical Society.

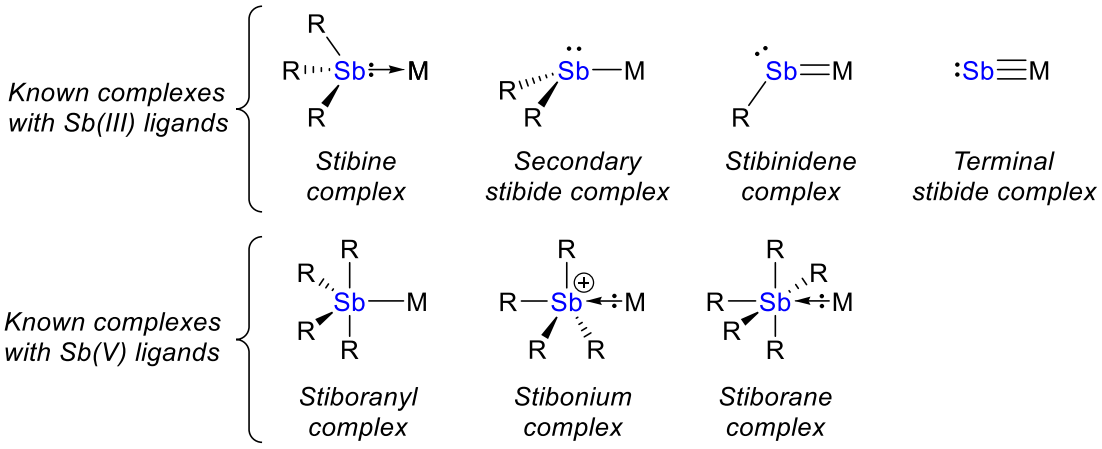

Figure 1. Known complexes of antimony ligands.

1.2 Bonding properties of stibines

Similar to phosphines, the Sb-M in transition metal stibine complexes is considered to be comprised of a σ component arising from the donation of the antimony lone pair into a vacant metal orbital and a π component arising from donation from the metal center into Sb-C σ* orbitals. On average, values of the Tolman electronic parameters found for stibines are higher than those found for the analogous phosphines (Table 1). This difference has been largely attributed to the higher s orbital character and diffuseness of the antimony lone pair. Additionally, the π-accepting abilities of stibines are weaker than that of phosphines and arsines, which is again attributed to the more diffuse nature of the Sb-C σ* orbitals.[1]

Table 1. Tolman electronic parameters for sample series of phosphines, arsines, and stibines.

Ligand	Tolman Electronic Parameter (cm^{-1})[a]
PPh_3	2070[2]
$AsPh_3$	2072[3]
$SbPh_3$	2074[4]
PEt_3	2066[5]
$AsEt_3$	2067[3]
$SbEt_3$	2067.4[4]

a: Measurements taken in hexadecane

In contrast to phosphines, which show little geometric perturbation upon coordination to a transition metal center,[6] coordinated stibines typically display a significant increase in ∠C-Sb-C and a shortening of Sb-C bond lengths relative to free stibines.[7, 8] Similar effects have been observed in adducts of stibines with Group 13 Lewis acids, which likely rules out any influence of the π-component of the Sb-M bond on the observed changes.[9-15] These geometric changes have instead been interpreted in terms of a hybridization of the antimony center upon coordination, in which s orbital character *increases* in the Sb-C bonds and *decreases* in the Sb-M bond. This hybridization, which has also been observed in bismuthines,[16] may serve to improve the directionality of antimony lone pair and thus enhance the Sb-M interaction.

1.3 Antimony-based Z-type ligands

Over the past decade, the field of Z-ligand chemistry[17] has experienced a renaissance prompted by the development of new ambiphilic ligand platforms combining both L-type

and Z-type ligands.[18-25] These new platforms have been used to generate complexes in which the L-type ligands serve to position a metal ion or atom in close proximity to the Lewis acidic, Z-type ligand site (Figure 2). The success of this approach is illustrated by a diverse series of complexes that incorporate a group 13 or a group 14 element as a Lewis acidic site. When appropriately designed, these molecules display a strong donor-acceptor interaction involving the metal as the donor and the Z-type ligand as the acceptor.

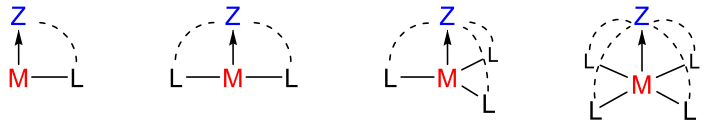

Figure 2. Known types of ambiphilic complexes.

The most developed class of complexes are undoubtedly those containing a tricoordinate boron atom as the Z-type ligand.[21, 23, 24, 26] In addition to displaying unique metal→boron donor-acceptor interactions, complexes supported by such ligands are also emerging in the domain of catalysis[26] where the boron center can promote heterolytic bond activation processes,[27] facilitate redox processes at the adjacent transition metal center[28] or simply increase the Lewis acidity of the latter by σ-inductive effects.[29] Fascinated by these advances, we questioned whether a related chemistry could be developed based on ambiphilic ligands that feature an antimony center as the Lewis acidic site.[30]

Our investigation into the coordination behavior of ambiphilic antimony ligands was initiated by a series of studies on compounds featuring Sb(V) centers tethered to mercury

or gold centers by rigid 1,8-naphthalenediyl linkers.[31-33] Having previously employed the 1,8-naphthalenediyl platform to enforce the proximity of Lewis acidic centers in bidentate Lewis acids,[34] our group questioned whether tethering a late, electron rich transition metal to a Lewis acidic Sb(V) center using this platform would promote the formation of otherwise unstable metal→Sb interactions. The gold- and mercury-stibonium species **1** and [**2**][PF_6] are prepared in one-pot syntheses by stepwise reaction of 1,8-dilithionaphthalene with Ph_3SbBr_2 and Au^I or Hg^{II} synthons (Figure 3).[31, 32] Structural studies showed that the Au-Sb distance in **1** (avg. 2.7616(8) Å) is significantly shorter than the Hg-Sb distance in [**2**][PF_6] (3.0601(7) Å) supporting the greater metallobasicity of gold(I) *vs.* mercury(II). The juxtaposition of an electron deficient tetraarylstibonium with an electron-rich, heavy d-block center results in an enhancement of the Lewis acidity of the d-block center.[33] The organomercury-stibonium compound $[\mathbf{2}]^+$, in contrast to typical organomercury species, is able to engage anionic (Cl^-, Br^-, I^-) and neutral ligands (N,N-dimethylaminopyridine, THF) at the mercury center (Figure 4, Figure 5).

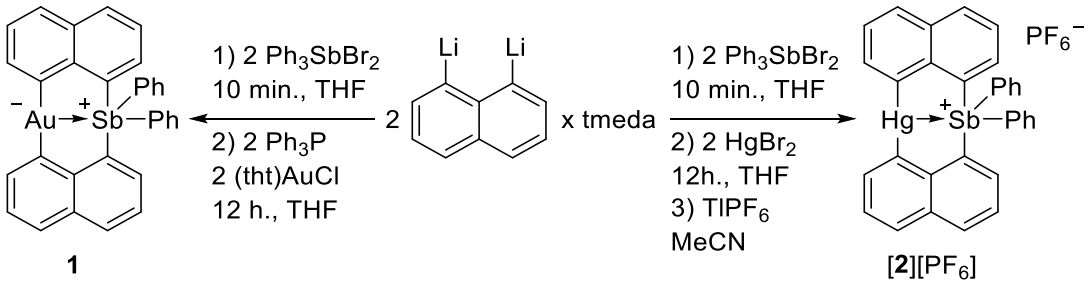

Figure 3. Synthesis of **1** and [**2**][PF_6].

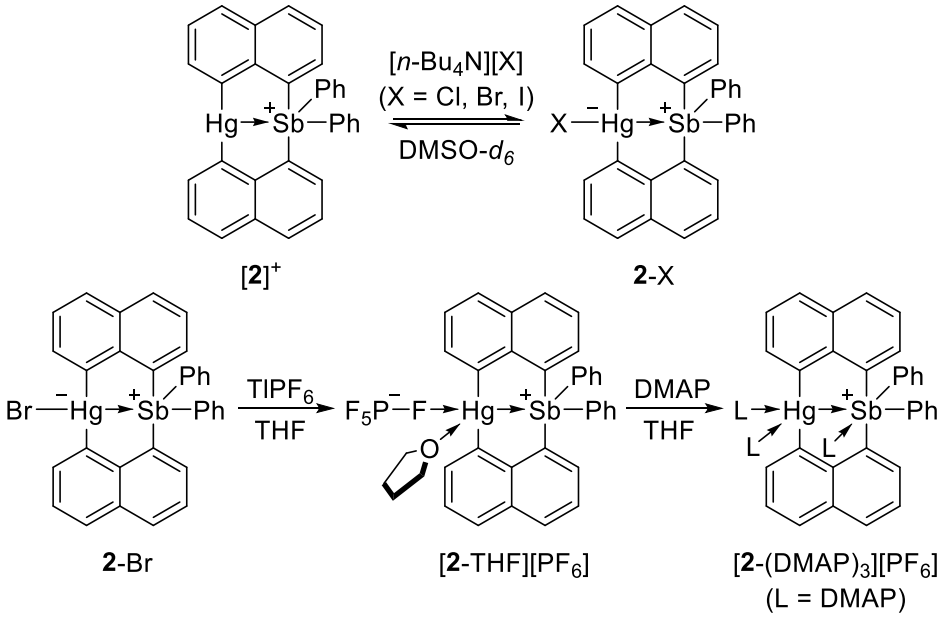

Figure 4. Coordination chemistry at the mercury center in [**2**]$^{+}$.

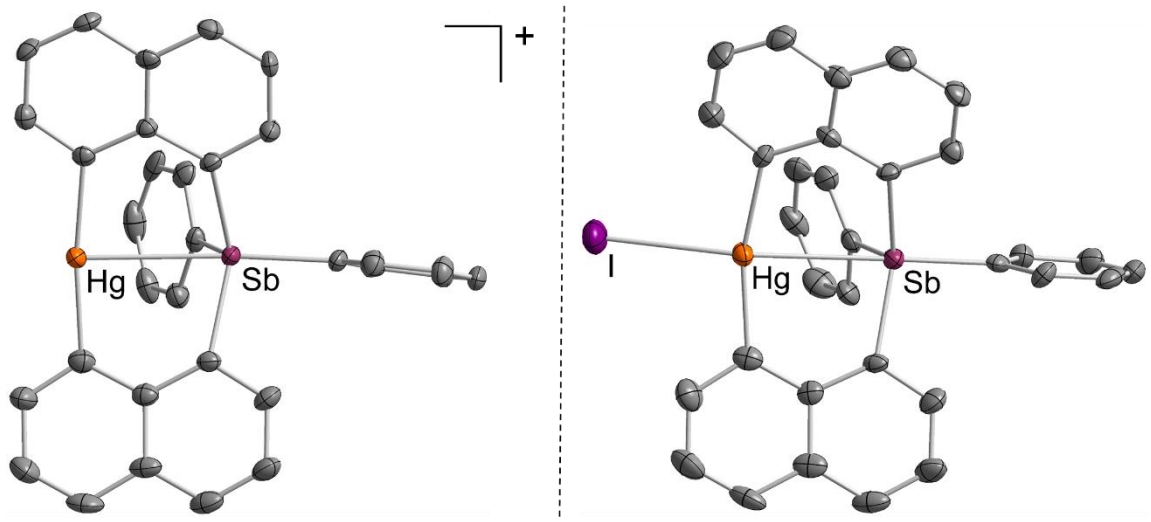

Figure 5. Structures of [**2**]$^{+}$ (left) and **2**-I(right).

Although electrostatic effects figure to be a strong component in the Sb-Au and Sb-Hg bonding in these compounds, we sought to investigate the extent of charge transfer between the antimony and metal centers. Electron localization function (ELF) studies on **1**[35] and derivatives of [**2**]$^+$ suggest that the stibonium moiety in these species engages the proximal metal center via orbital-based interactions (M→σ*(Sb-C_{Ph})), which are enhanced in the case of **2**-I upon binding of I^- *trans* to the antimony center (Figure 6). Despite computational evidence for bonding interactions between the antimony and metal centers in these compounds, the Au and Hg L_3-edge X-ray Absorption Near Edge Structure (XANES) spectra of **1** and **2**-I show no discernable oxidation of their respective metal centers relative to reference compounds (Figure 7).[32, 33] A similar lack of significant charge transfer has been observed in the XANES spectra of metal-only Lewis pairs between zerovalent group 10 isocyanides and Tl^+ cations.[36]

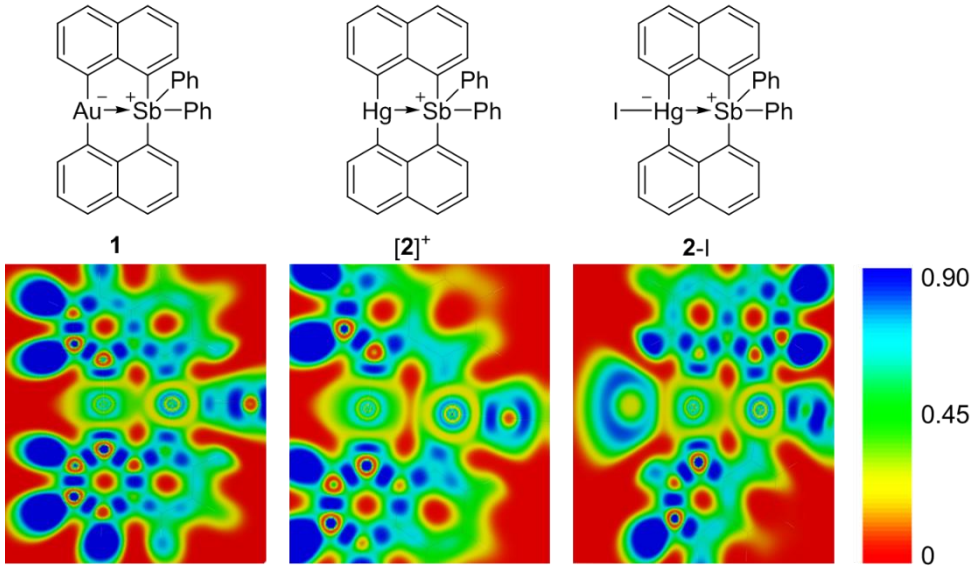

Figure 6. ELF plots for **1**, [**2**]$^{+}$, and **2**-I.

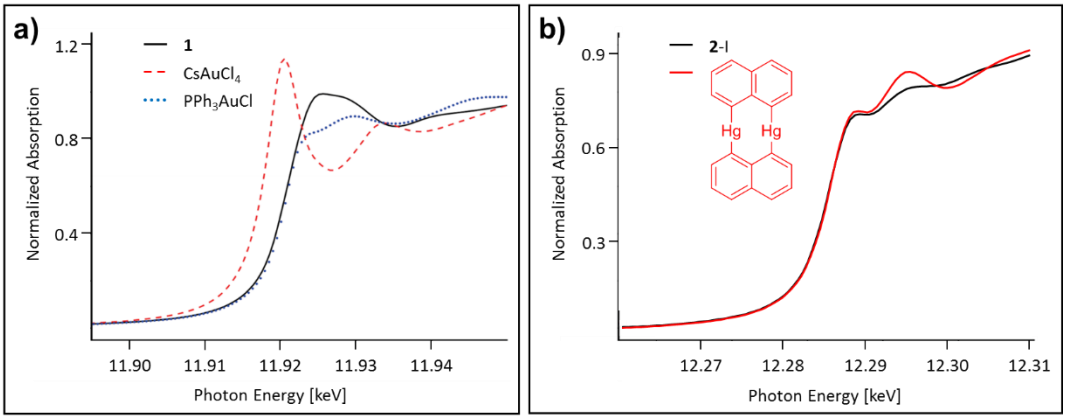

Figure 7. (left) Solid-state XANES spectrum of the Au L_3-edge of **1** compared to Au(III) and Au(I) reference compounds. (right) Solid-state XANES spectrum of the Hg L_3-edge of **2**-I compared to a Hg(II) reference.

In addition to their heavy d-block centers, the tetraarylstibonium groups in compounds **1** and [**2**]$^{+}$ are also readily engage Lewis basic substrates, including fluoride anions. Coordination of the latter affords the fluorostiborane complexes [**1**-F]$^{-}$ and **2**-F, respectively (Figure 8, Figure 9).[32, 33] The ability of the stibonium moiety to coordinate additional ligands suggests that despite being in the coordination sphere of the d-block center, the antimony center retains considerable Lewis acidity. It is also noteworthy that fluoride coordination does not affect the length of the Au-Sb (2.7694(8) Å in [**1**-F]$^{-}$) or Hg-Sb (3.0495(18) Å in **2**-F) bonds, which are almost equal to those in **1** (avg. 2.7616(8) Å) and [**2**][PF_6] (3.0601(7) Å), respectively.

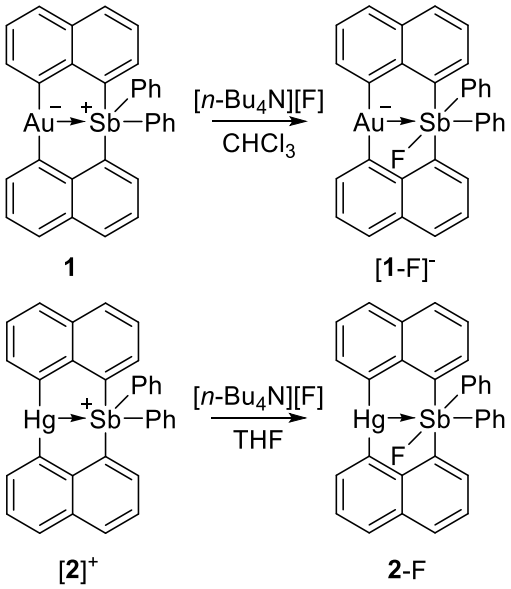

Figure 8. Reactions of **1** and [**2**]$^{+}$ with F^{-}.

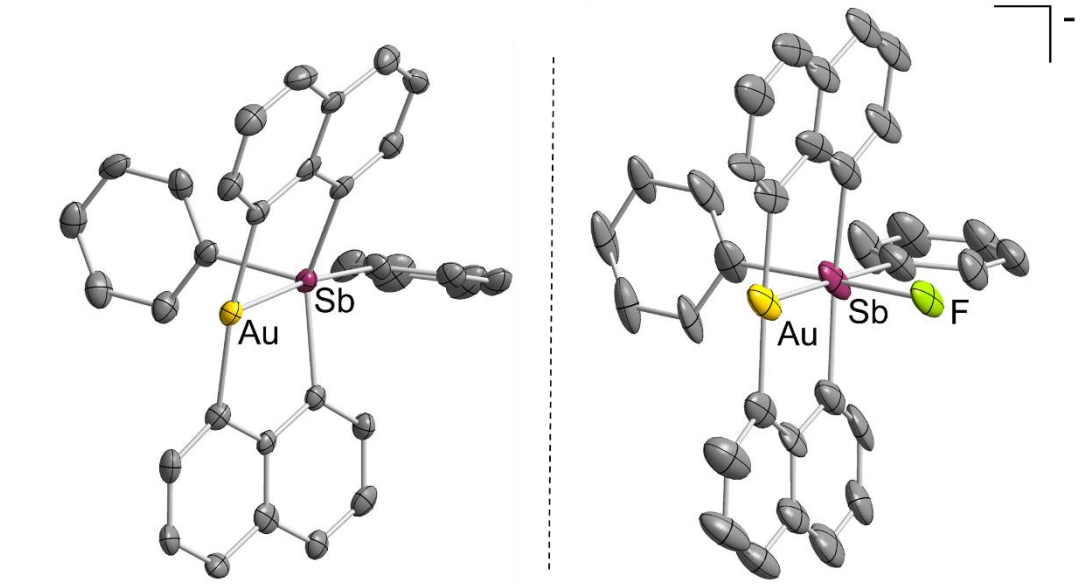

Figure 9. Crystal structures of **1** (left) and its fluoride adduct [**1**-F]$^-$ (right).

Taken together, these seminal studies demonstrated two important concepts: 1) Incorporation of a Lewis acidic antimony center into the coordination sphere of a d-block center modifies the behavior of the d-block metal by polarizing its electron density, 2) The antimony center itself may engage neutral and anionic Lewis bases, potentially allowing for modification of the main group-transition metal interaction.

In addition to oxidized antimony species acting as σ-acceptors towards metal centers, we have also demonstrated that Sb(III) moieties may act as Lewis acids towards late transition metal centers.[37, 38] Reaction of (tht)AuCl (tht = tetrahydrothiophene) with the bisphosphinylstibine ligands **3**-Ph and **3**-Cl affords complexes **4** and **5** (Figure 10).[37]

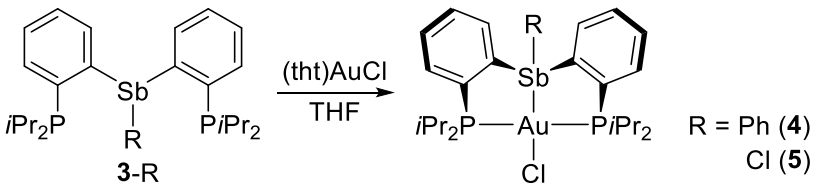

Figure 10. Complexation of **3**-R with (tht)AuCl.

The crystal structures of **4** and **5** show that the antimony centers in both complexes adopt disphenoid rather than tetrahedral geometries, indicating that the antimony center is not strongly engaged with the gold center as a Lewis base (Figure 11).[1] Despite the overall structural similarity between **4** and **5**, replacement of a phenyl ligand on antimony with a chloride results in a significant distortion of the geometry of the gold center, as indicated by their respective Sb-Au-Cl1 angles of 115.09(2)° (**4**) and 141.73(4)° (**5**). Such distortions towards square planar geometry in tetracoordinate gold(I) complexes are associated with the incorporation of a Z-ligand in the gold coordination sphere, as seen in ClAu[(*o*-(*i*Pr$_2$P)C$_6$H$_4$)$_2$BPh] (∠Cl-Au-B = 168.7 º).[39] Natural Bond Orbital (NBO) analysis of **4** breaks the Sb-Au bonding into distinct lp(Sb)→6p(Au) and lp(Au)→σ*(Sb-C$_{Ph}$) interactions. In contrast to the "confused" σ-donor/acceptor behavior displayed by the stibine ligand in **4**, NBO analysis of **5** finds only a lp(Au)→σ*(Sb-Cl2) interaction, indicating that the chlorostibine moiety acts as a pure Z-type ligand. Similar σ-acceptor behavior has also been documented in related bisphosphinylbismuthine complexes.[40, 41]

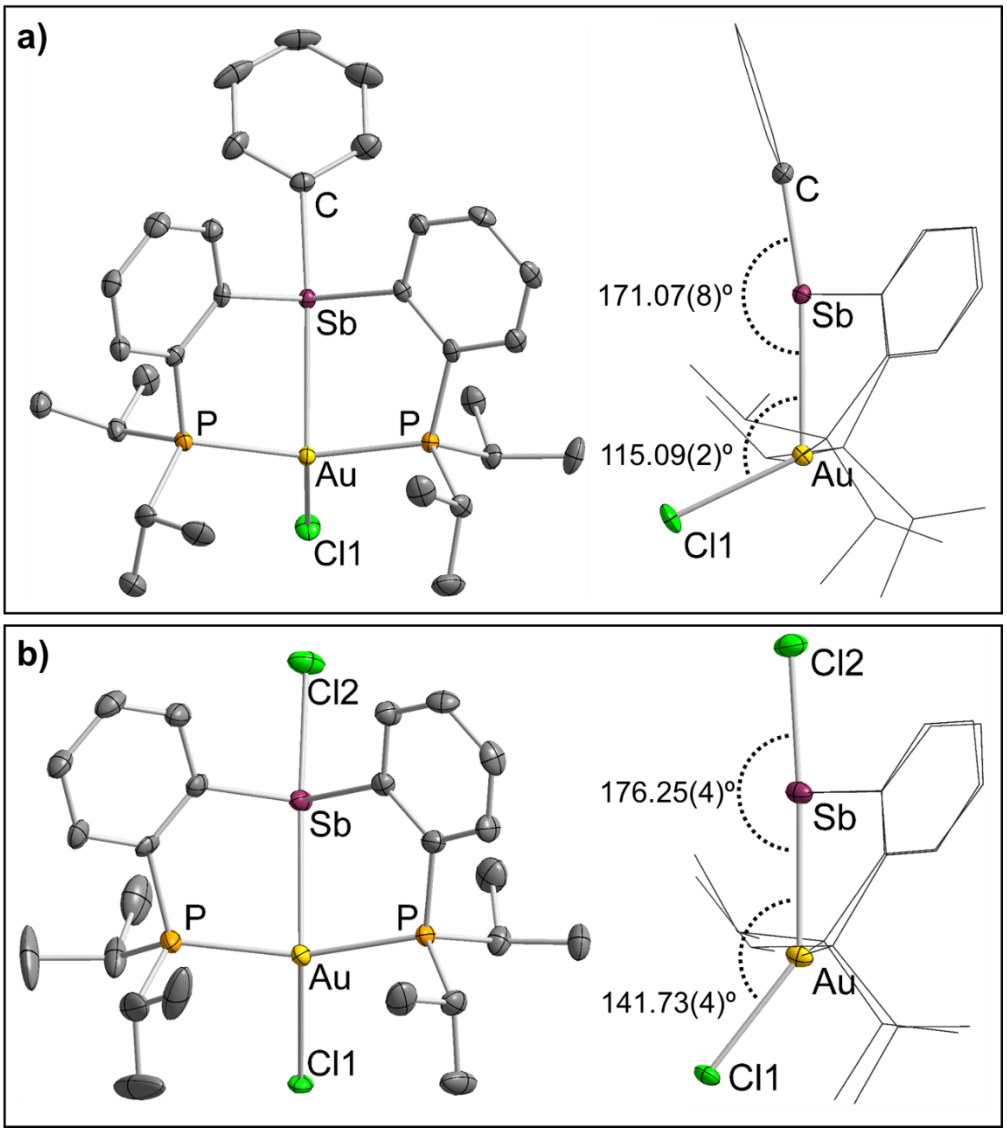

Figure 11. Front and side view of the crystal structures of (a) **4** and (b) **5**.

1.4 Coordination-noninnocence in antimony-transition metal complexes

As previously observed in the gold and mercury stibonium complexes **1** and [**2**]$^{+}$, organoantimony (V) species may retain residual Lewis acidity despite being in the coordination sphere of a transition metal. In addition to oxidized group 15 centers,

coordinated antimony centers in the (III) oxidation state have also been shown to engage in secondary interactions with Lewis basic substrates.[30, 42, 43] This phenomenon, which we term coordination non-innocence, typically manifests through the presence of low-lying E-X or E-C σ* orbitals. Drawing an analogy between four-coordinate stibonium species which are well-known Lewis acids[44-47] and four-coordinate, cationic transition metal coordinated stibines, we questioned whether an Sb-M σ* orbital could also impart Lewis acidic properties in a direction *trans* from the metal site (Figure 12).

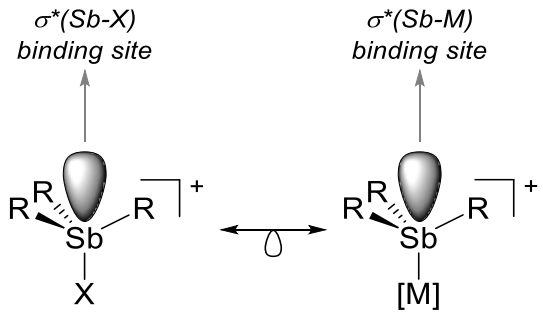

Figure 12. Illustration of the isolobal relationship between $[R_3SbX]^+$ and $[(R_3Sb)M]^+$.

As part of our ongoing interest in anion-sensing,[44, 47, 48] we have investigated the use of coordination non-innocent ligands for the sensing of aqueous fluoride. As binding of hard anions such as fluoride at coordination non-innocent antimony centers affects the electronics of the transition metals to which they are coordinated, we questioned whether this property could be harnessed to provide a "turn-on" response to anion binding. Our first effort towards this goal was the investigation of cationic palladium bis- and

trisphosphinylstibine species [**8**]$^+$ and [**9**]$^+$, prepared by complexation of (cod)$PdCl_2$ (cod = 1,5-cyclooctadiene) with the corresponding polyphosphinylstibine ligands **6**-Ph and **7**, followed by chloride abstraction with $NaBPh_4$ (Figure 13).[49]

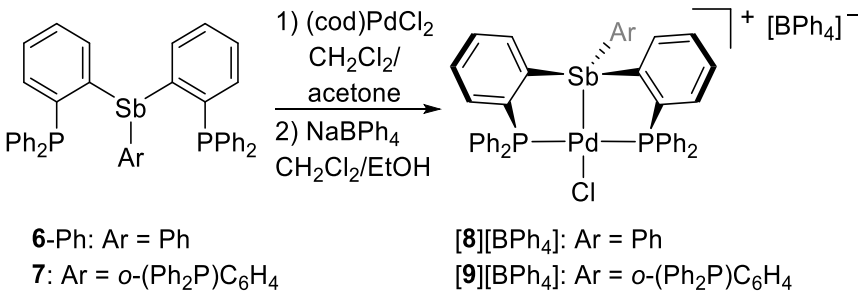

Figure 13. Synthesis of [**8**][BPh_4] and [**8**][BPh_4].

Inspection of the crystal structures of [**8**]$^+$ and [**9**]$^+$ shows that in both cases, the palladium center adopts a square planar geometry. Although the ^{31}P NMR spectrum of [**9**]$^+$ contains a single resonance, its crystal structure shows that the third phosphine arm is not coordinated in the solid state, suggesting that the coordination of the phosphine arms is fluxional in solution. Treatment of CH_2Cl_2 solutions of both [**8**][BPh_4] and [**9**][BPh_4] with TBAF results in the formation of fluoride complexes **8**-F and **9**-F, as indicated by the appearance of fluorine resonances featuring coupling to phosphorus in their ^{19}F NMR spectra (**8**-F: -121.61 ppm, $^3J_{F\text{-}P}$ = 26.7 Hz, **9**-F: -129.72 ppm, $^3J_{F\text{-}P}$ = 20.7 Hz). In the case of [**9**]$^+$, formation of the fluoride adduct is accompanied by a rapid color change from pale yellow to deep orange (Figure 14).

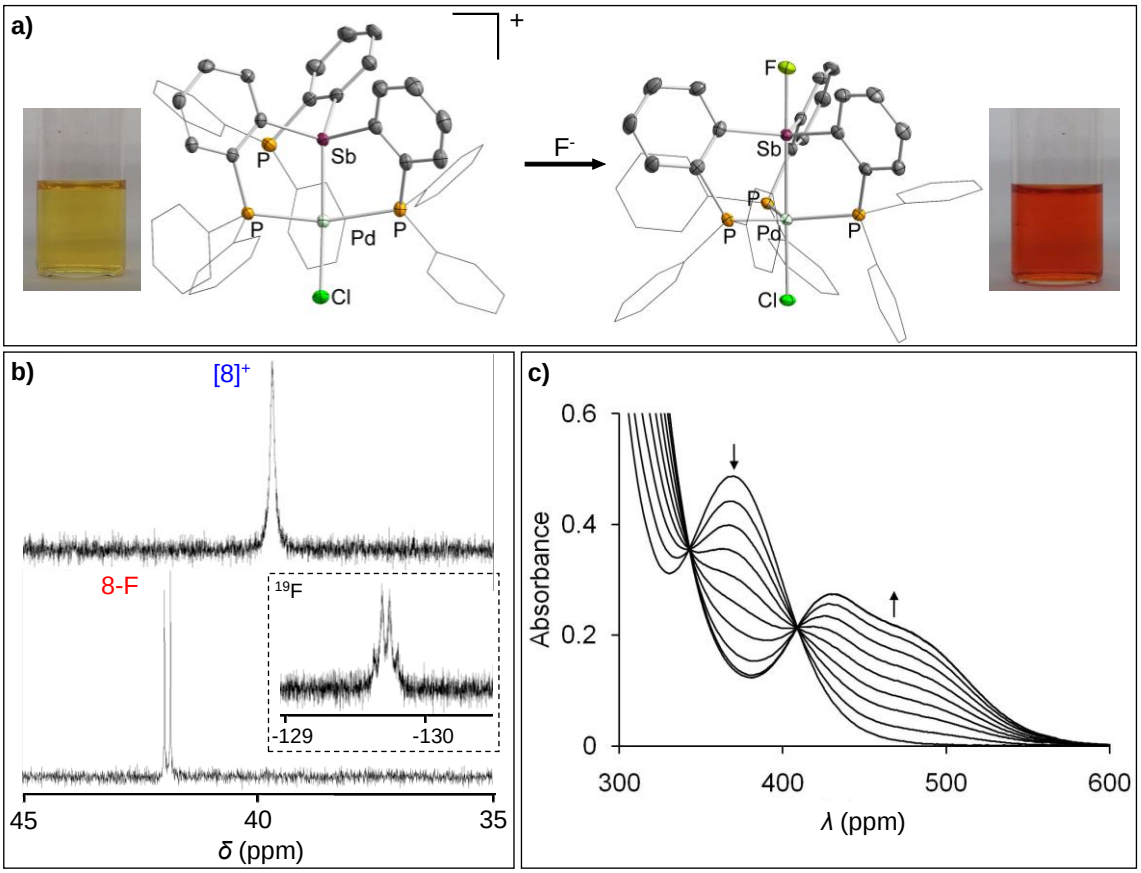

Figure 14. (a) Colorimetric and geometric changes in [**9**]$^+$ upon binding fluoride to form **9**-F. (b) Changes in ^{31}P and ^{19}F NMR upon formation of **9**-F. (c) Changes in the absorption spectra of [**9**]$^+$ upon incremental addition of TBAF.

Comparison of the crystal structures of **8**-F and **9**-F reveals that while the palladium center in **8**-F remains square planar, the palladium center of **9**-F attains a trigonal bipyramidal geometry *via* coordination of the third phosphine arm. It is this change in coordination geometry at palladium along with the corresponding change in ligand-field transitions, which is responsible for the colorimetric turn-on response to fluoride anion binding. The coordination non-innocent antimony center in [**9**]$^+$ thus acts as an allosteric

site, with fluoride coordination at antimony triggering coordination of the pendant third phosphine arm to the palladium center. While insolubility in water limits the use of [**9**]$^{+}$ in pure water, CH_2Cl_2 solutions layered with aqueous solutions of fluoride as low as 4 ppm in concentration display fluoride binding, as monitored by UV-vis and ^{31}P NMR spectroscopy.

1.5 Redox chemistry of antimony-transition metal complexes

In addition to exploring the Lewis acidity of coordinated antimony centers, we have undertaken an investigation of the redox properties of heterobimetallic antimony-transition metal complexes. Organoantimony compounds display a rich redox chemistry, which usually involves transitions from the Sb(III) to the Sb(V) state and *vice versa*.[50] Despite the well-known redox activity of antimony species, few attempts to transfer this reactivity to antimony-transition metal complexes prior to the past decade were made. A number of notable contributions to this field of study were, however, made by Malisch and coworkers, who investigated the synthesis and reactivity of transition metal stibido complexes. Such compounds were observed to undergo a variety of redox processes, including halogen oxidation (A)[51, 52], quaternization (B) [53], isomerization (C) [54], and reductive Sb-M bond cleavage (D)[52] (Figure 15).

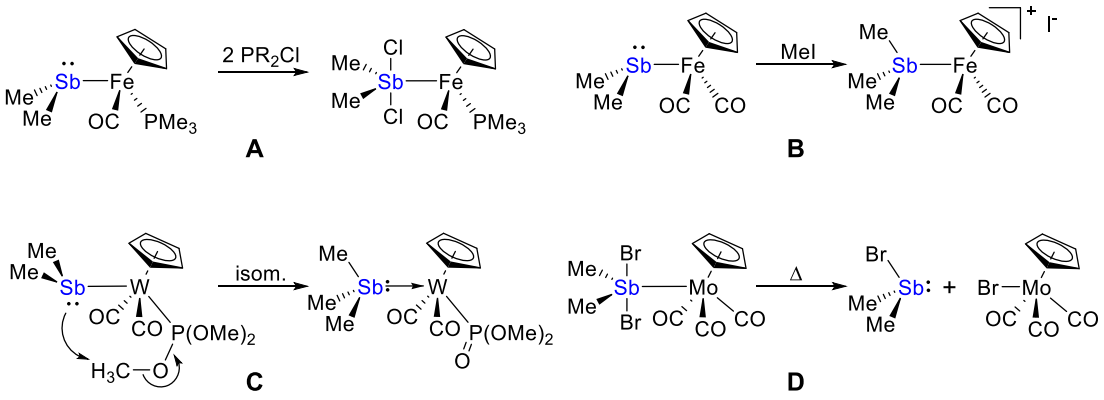

Figure 15. Examples of redox reactions of transition metal stibido compounds described by Malisch and coworkers.

While such redox reactions had been described for transition metal stibido complexes, no such reactivity had been ascribed to transition metal stibines prior to the initiation of our investigation. Upon treatment of a transition metal stibine complex with a two-electron oxidant, we surmised the possibility of three distinct modes of oxidation (Figure 16). In addition to localized oxidation of either the antimony or the transition metal center (A and C), we also hypothesized that oxidation across the heterobimetallic core may be feasible (B).

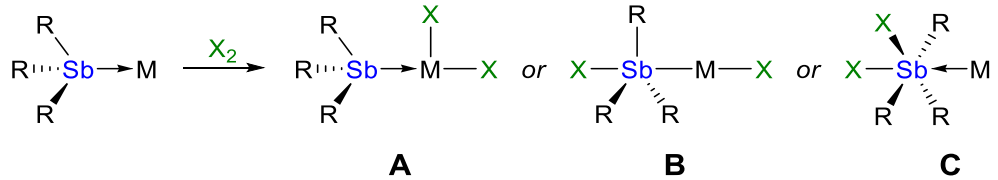

Figure 16. Possible two-electron oxidation products of (R_3Sb)[M].

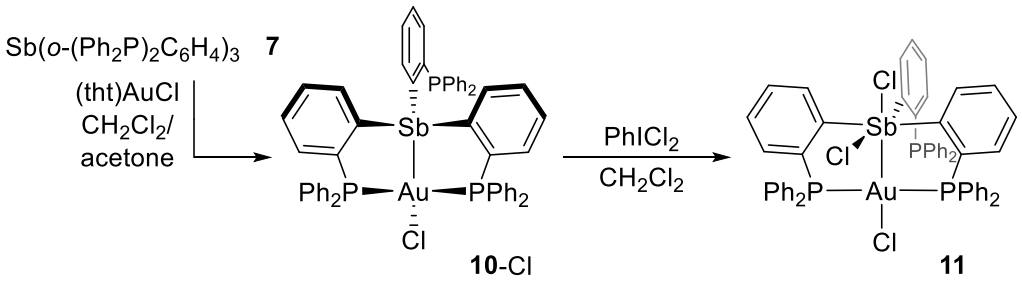

Figure 17. Synthesis and subsequent oxidation of **10**-Cl.

In our first attempt to access such species, we targeted a gold complex featuring the trisphosphinylstibine ligand **7**.[55] Reaction of (tht)AuCl with **7** afforded compound **10**-Cl (Figure 17) which underwent a clean antimony-centered oxidation upon treatment with $PhICl_2$, leading to complex **11**. Formation of **11** was found to be reversible by treatment with excess NaI as the reductant to afford the gold iodide **10**-I. The structure of **11** confirms that $PhICl_2$ oxidizes the stibine ligand to produce a dichlorostiborane moiety in the coordination sphere of gold. Although this oxidation is localized at the antimony center, the gold atom shows a noticeable response in its coordination geometry, changing from distorted tetrahedral in **10**-Cl to a square planar geometry in **11**. This geometry change occurs concomitant with a shortening of the Sb-Au separation from 2.8374(4) Å to 2.7086(9) Å. The square planar geometry of the gold center in **11**, which is typically associated with the trivalent state, suggests that oxidation of the coordinated stibine effects a significant electronic perturbation on the gold center. As indicated by NBO calculations, conversion of **10**-Cl into **11** is accompanied by an umpolung of the Au→Sb donor-acceptor interaction which switches from Sb→Au in **10**-Cl to Sb←Au in **11** (Figure 18).

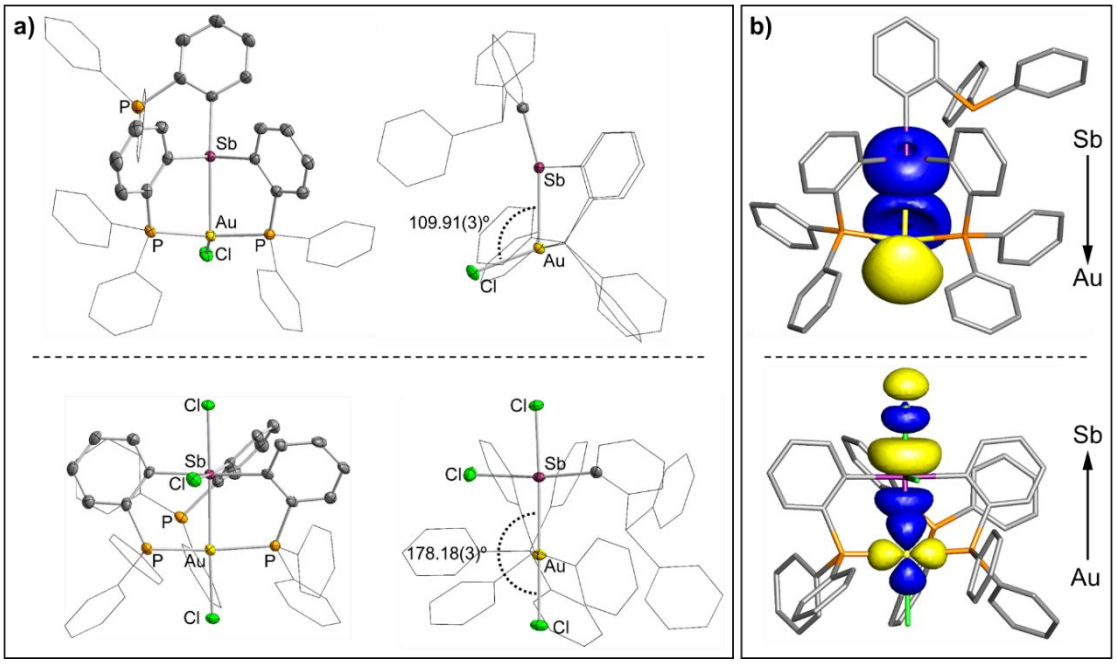

Figure 18. (a) Front and side views of the crystal structures of **10**-Cl (top) and **11** (bottom). (b) NBO plots of the principal Sb-Au interactions in **10**-Cl (top) and **11** (bottom).

Similar two-electron oxidations of gold-coordinated stibines were observed in the treatment of the bisphosphinylstibine gold complexes **4** and **5** with tetrachloro-1,2-benzoquinone (*o*-chloranil) to form the catecholatostiborane complexes **12** and **13**, respectively (Figure 19).[37] Congruent with the structural changes associated with the conversion of **10**-Cl to **11**, comparison of the crystal structures of **4** and **12** illustrates a significant shortening of the Au-Sb bond (2.8669(4) Å in **4** to 2.6833(3) Å in **12**), as well as a change in the coordination geometry of the gold center from trigonal pyramidal to distorted square planar. NBO analyses performed on **12** and **13** describe the Sb-Au bond in both cases as a natural localized molecular orbital (NLMO) with strongly elevated

orbital contributions from the gold atom (16.2% Sb/83.8% Au for **12**, 16.3% Sb/83.7% Au for **13**), consistent with the presence of a Au→Sb bond.

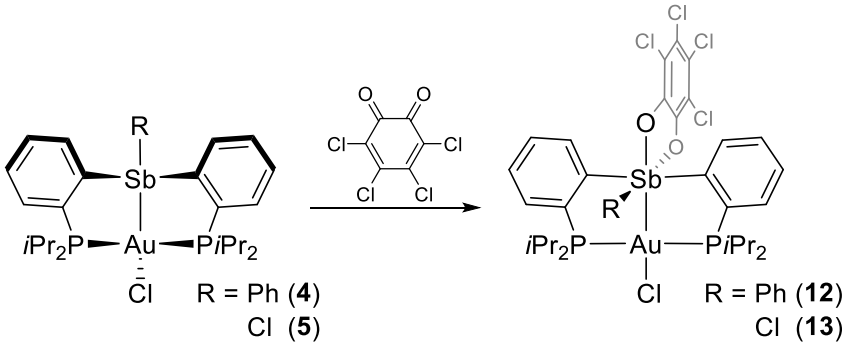

Figure 19. Oxidation of **4** and **5** by *o*-chloranil.

Complexes that support the photoreductive elimination of halogens are attracting an increasing interest because of the relevance of this elimination reaction to light driven HX splitting reactions. In this context, a number of binuclear transition metal species have been investigated due to their ability to sustain reversible, two electron oxidation.[56-66] As heavy main group elements readily undergo two electron redox processes,[50, 67, 68] our group has investigated the possibility that their incorporation into heterobimetallic transition metal-main group complexes may provide platforms that also sustain reversible two electron redox processes at their dinuclear cores.[37, 38, 55, 69-71] Complexation of $(Et_2S)_2PtCl_2$ with the bisphosphinylchlorostibine ligand **6**-Cl leads to the formation of the platinum pincer complex **14** (Figure 20).[70] Complex **14** sustains a two-electron oxidation by $PhICl_2$ to afford the corresponding tetravalent platinum species (**15**). This complex is

interesting in that the five electron withdrawing chlorine atoms decorating the central core may destabilize the complex and make it prone to photoreduction.

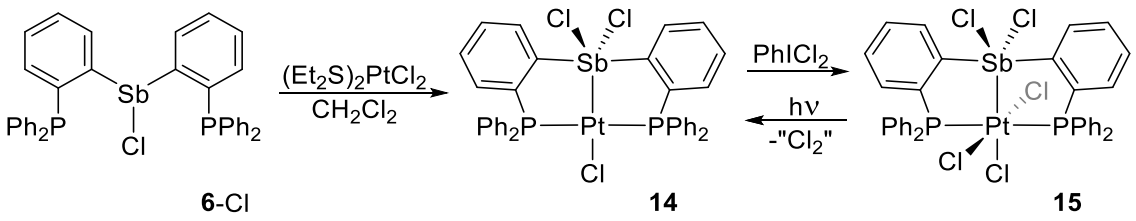

Figure 20. Synthesis and photoredox chemistry of **14**.

Upon irradiation at 320 nm in the presence of 2,3-dimethyl-1,3-butadiene (DMBD) as a radical trap, **15** undergoes clean elimination of a Cl_2 equivalent to regenerate the reduced species, as indicated by both UV-vis and ^{31}P NMR spectroscopy (Figure 21). Upon optimizing the DMBD concentration, the quantum yield of 13.8% was obtained for **15**, which is lower than the value of 38% obtained for a related Pt_2 complex.[62] Remarkably, complex **15** also evolves chlorine when irradiated in the solid state at atmospheric pressure in the absence of trap. Evolution of chlorine or chlorine radicals has been confirmed using sodium metal as a trapping agent, accounting for ~70% of the predicted chlorine released.

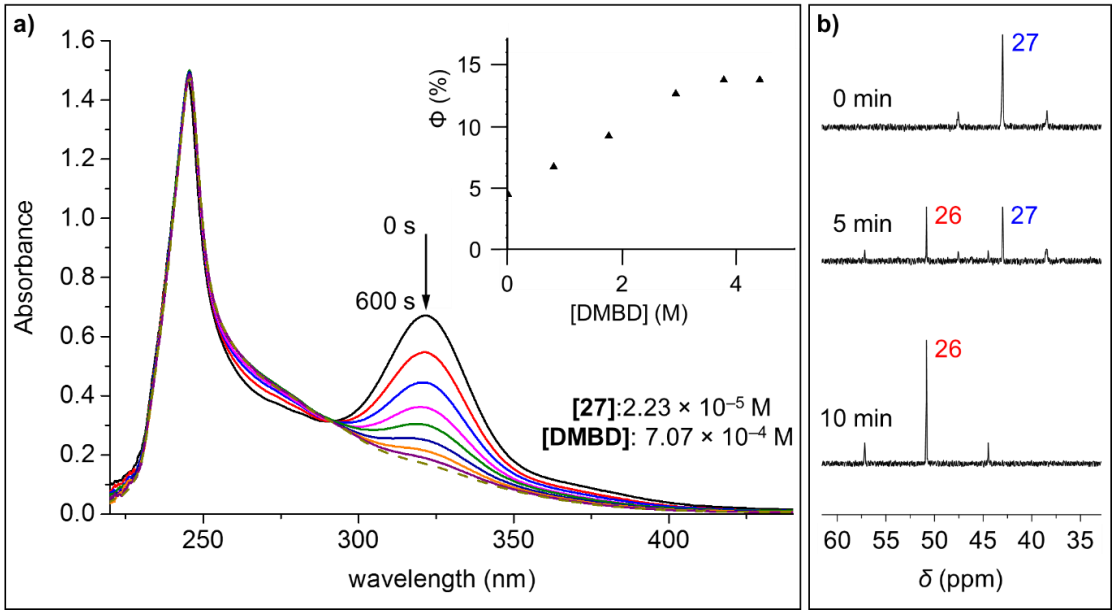

Figure 21. (a) Absorption spectra obtained during the photolysis of **15**, with an inset plot of quantum yield vs. DMBD concentration. (b) ^{31}P NMR spectra of the photolysis of **15**.

Having demonstrated that a change in the redox state of a main group center held in proximity to a transition metal center affects the electronics of the heterobimetallic bond, we surmised that redox changes in ligands containing heavy main group ligands may provide the means to control the Lewis acidity and reactivity of a catalytic transition metal center. Such a concept is illustrated by the report of a gold borane complex featuring a $[L_2Au{\rightarrow}BAr_3]^+$ interaction which acts as a catalyst for enyne cyclization.[29] As $[L_2Au]^+$ species are typically not active in catalysis, we questioned whether a redox active antimony fragment may provide similar activation of an otherwise inactive $[L_2Au]^+$ fragment (Figure 22).

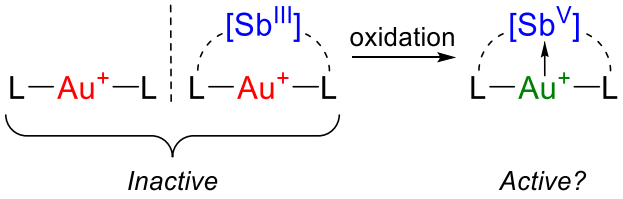

Figure 22. Proposed activation of an $[L_2Au]^+$ fragment by oxidation at antimony.

To this end, we chose to examine gold complexes featuring the bisphosphinylchlorostibine ligand **6**-Cl which, due to its inductively withdrawing chloride substituent, features a Lewis acidic antimony center even in the Sb(III) state.[38] Complexation of (tht)AuCl with **6**-Cl, followed by chloride abstraction with $AgSbF_6$ afforded the cationic gold species [**16**][SbF_6] (Figure 23).

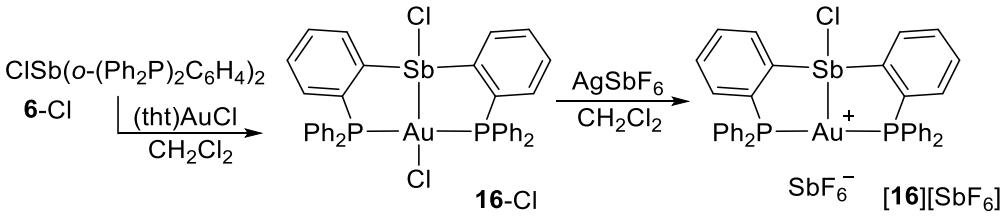

Figure 23. Synthesis of [**16**][SbF_6].

To investigate whether the mildly Lewis acidic Sb(III) center present in [**16**][SbF_6] is sufficient to activate the bisphosphinyl gold cation fragment for catalysis, its ability to catalyze the hydroamination of phenylacetylene with *p*-tolylaniline was tested (Table 2).[72]

Salt [**16**][SbF_6] displays poor but non-negligible activity in this hydroamination reaction relative to [$(Ph_3P)_2Au$][SbF_6] (no conversion), with only 2.7% conversion into the imine product after 3 hours. Although the catalytic activity of [**16**][SbF_6] demonstrates that a chlorostibine ligand may activate an otherwise inert gold center, we questioned whether oxidation of the antimony center might allow for stronger activation of the gold center and thus improve catalytic performance.

Table 2. Activities of selected gold catalysts for hydroamination.

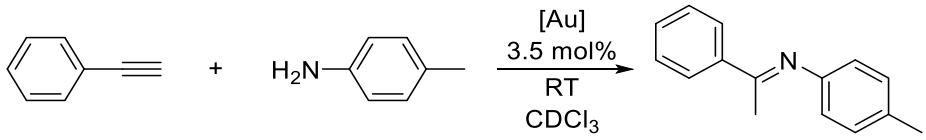

[Au]	Reaction Time	Conversion (%)
[$(Ph_3P)_2Au$][SbF_6]	3 h	0
[**16**][SbF_6]	3 h	2.7
[**18**][SbF_6]	40 min	98

Treatment of **16**-Cl with $PhICl_2$ cleanly afforded **17**-Cl, which was then converted into the more soluble **18**-Cl with TBAF (Figure 24). Subsequent chloride abstraction with $AgSbF_6$ afforded the cationic bisphosphinyl gold species [**18**][SbF_6].

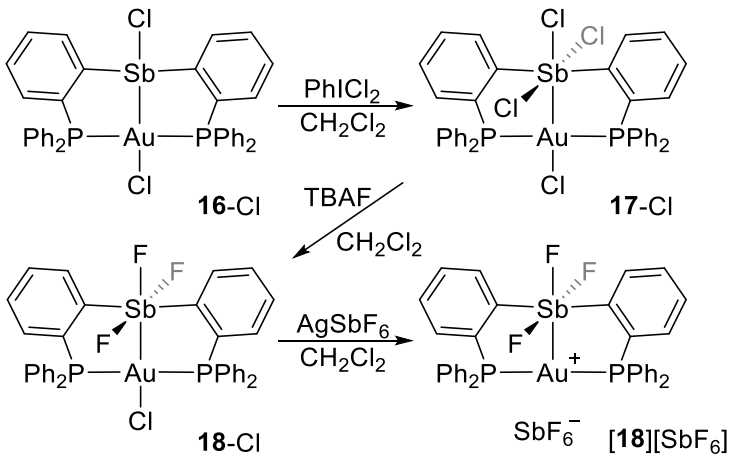

Figure 24. Synthesis of [**18**][SbF_6].

Comparison of the crystal structures of [**16**][SbF_6] and [**18**][SbF_6] reveals that oxidation of the antimony center results in a notable shortening of the Au-Sb separation from 2.9318(5) Å to 2.8196(4) Å, indicating the stronger Au→Sb interaction present in [**18**][SbF_6] (Figure 25). In line with the strengthening of the Au-Sb interaction, the acidity of the gold center in [**18**][SbF_6] increases, as evidenced by its ability to form adducts with adventitious water; a trait typically associated with trivalent gold species.[72]

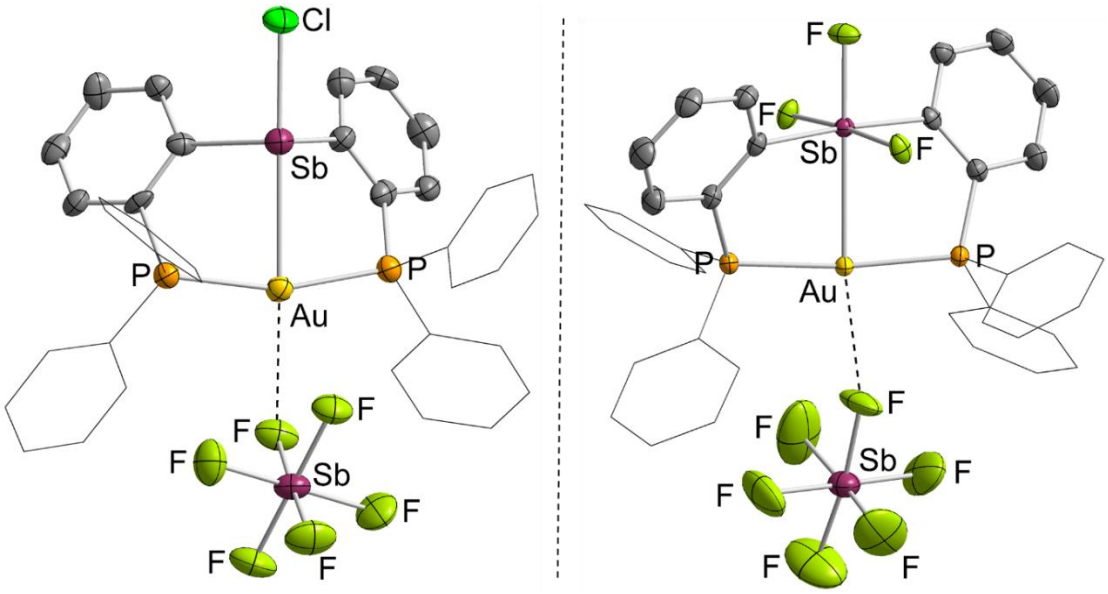

Figure 25. Crystal structures of [**16**][SbF_6] (left) and [**18**][SbF_6] (right).

In an attempt to quantify the acidity of these cations relative to typical bis(phosphine) gold(I) species, we carried out simple Gutmann-Beckett type measurements on [**16**][SbF_6], [**18**][SbF_6], and [$Au(PPh_3)_2$][SbF_6] using triphenylphosphine oxide (Ph_3PO, ^{31}P NMR (CH_2Cl_2): δ = 27.3 ppm) as the Lewis base. While no change in the chemical shift of Ph_3PO occurs upon mixing with [$Au(PPh_3)_2$][SbF_6], mixing of Ph_3PO with [**16**][SbF_6] and [**18**][SbF_6] causes the Ph_3PO resonance to shift downfield to 30.6 and 32.9 ppm, respectively. Taken collectively, these results suggest that the otherwise poorly acidic gold atoms in [**16**][SbF_6] and [**18**][SbF_6] are activated by their proximity to the Sb(III) and Sb(V) acids.

With the Sb(V) species [**18**][SbF_6] in hand, we next investigated its catalytic activity using the same model reaction employed for [**16**][SbF_6] (Table 2). In sharp contrast to the

activity of [**16**][SbF_6], hydroamination of phenylacetylene with *p*-tolylaniline by [**18**][SbF_6] affords virtually complete conversion after only 40 minutes reaction time at room temperature. As many transition metal-catalyzed hydroaminations require inert atmosphere, elevated temperatures, and extended reaction times, the ability of [**18**][SbF_6] to catalyze this reaction in air under mild conditions is noteworthy. Although [**18**][SbF_6]-catalyzed hydroaminations cannot be extended to alkylamines, the reactions proceed with a variety of arylamines, as well as phenylhydrazine (Figure 26).

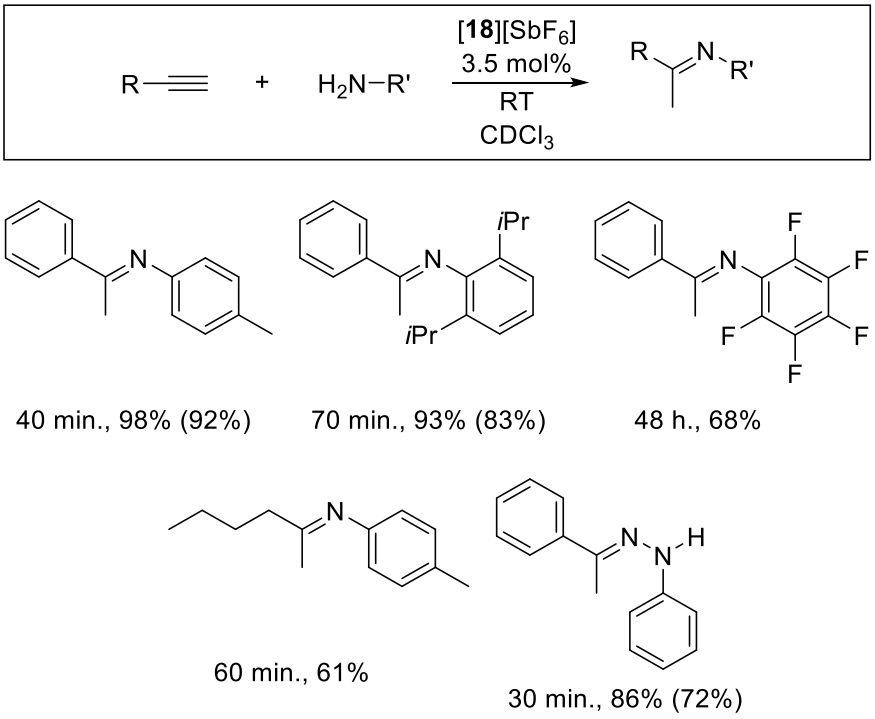

Figure 26. Scope of alkyne hydroaminations catalyzed by [**18**][SbF_6]. Reaction times, conversion percentages, and isolated yields (parentheses) are listed under each entry.

1.6 Objectives

Our prior work in this area demonstrates that the utilization of donor buttresses to enforce antimony-transition metal interactions allows for the observation of unique redox and coordination chemistry of the tethered antimony ligand. We have established that tethered Sb(III) and Sb(V) centers are capable of acting as Z-type ligands towards late transition metals. The antimony centers of such species may also display coordination non-innocent behavior, engaging in secondary interactions while in the coordination sphere of a metal. In order to understand the latter phenomenon, we have initiated a study aimed to elucidate the origin of the Lewis acidity of the antimony centers in such complexes. Additionally, in the hope of understanding how coordination non-innocence may be applied to tune a transition metal center, we have undertaken a systematic investigation into the effect of secondary coordination events on the antimony-transition metal bond.

In addition to our fundamental efforts to investigate the origin and consequences of coordination non-innocent behavior in antimony ligands, we have also sought to apply this behavior in the realm of catalysis. To this end, we have investigated the ability of coordination non-innocent antimony centers to facilitate electrophilic catalysis.

Having demonstrated in our prior efforts that coordinated antimony centers are redox active, we determined to further investigate this behavior by varying the identity of the transition metals employed. Furthermore, we have begun to explore the unique redox-switching behavior of coordinated antimony ligands, in which a coordinated antimony center acts as a dynamic partner towards a redox active metal by undergoing anion

metathesis. In addition to being of fundamental interest, this phenomenon may have applications in both anion sensing and catalysis.

2. ORIGINS OF COORDINATION NON-INNOCENCE IN TRANSITION METAL STIBINE COMPLEXES

2.1 Introduction

Interest in transition metal stibine complexes has been renewed in recent years due to the unusual properties of their coordinated antimony centers, including the ability to undergo two-electron redox processes and engage in secondary bonding interactions. The latter ability, which we refer to as coordination non-innocence, can be considered to manifest through the interaction of donor groups with accessible Sb-R or Sb-M σ* orbitals (Figure 27).[73] Electrostatic interactions are also likely to play a key role in such interactions, which places the coordination non-innocence of transition metal stibines within the spectrum of σ-hole interactions.[74, 75] Several examples of stibine complexes featuring antimony centers engaging in secondary bonding interactions where the donor binds *trans* to a Sb-R bond have been reported, and a recent review by Reid demonstrates the prevalence of this type of interaction in previously reported crystal structures.[43] Examples of secondary bonding interactions where a donor binds *trans* to a Sb-M bond, while considerably less common, are of special interest due to the possibility of modulating the electronics of the metal center *via* interactions at the antimony center.[49] Thus far, such interactions have only been observed in complexes of polydentate ligands in which the Sb-M interaction is buttressed by auxiliary donor ligands.

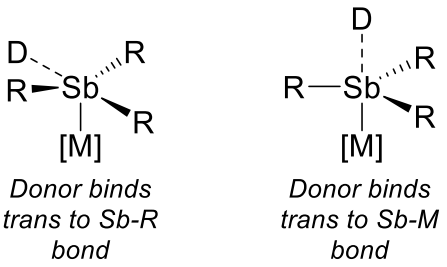

Figure 27. Possible binding modes of donors (D) to coordinated stibines.

The unusual coordination properties of polydentate stibine ligands were apparent from early studies of nickel complexes of the trisphosphinylstibine ligand (*o*-$(Ph_2P)C_6H_4)_3Sb$ (**7**) and its lighter analogues (*o*-$(Ph_2P)C_6H_4)_3P$ (**19**) and (*o*-$(Ph_2P)C_6H_4)_3As$ (**20**).[76, 77] Complexation of these ligands with $NiCl_2•6H_2O$, followed by subsequent chloride abstraction by $NaBPh_4$ afforded five-coordinate lantern complexes of the form [ClNi((*o*-$(Ph_2P)C_6H_4)_3E$)][BPh_4] (**21**-**23**) (Figure 28).

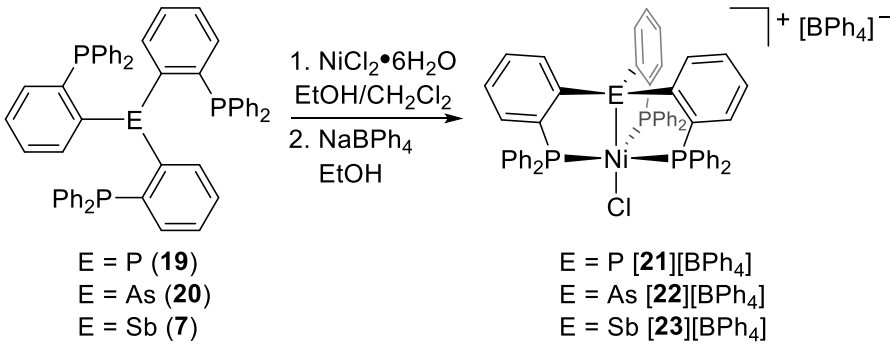

Figure 28. Venanzi's synthesis of lantern complexes **21**-**23**.

Assuming local C_{3v} symmetry about the nickel center, inspection of the UV-vis spectra of **21**-**23** found that the energy of the bands corresponding to the $(e_2)^4(e_1)^4 \rightarrow (e_2)^4(e_1)^3(a_1)^1$ and $(e_2)^4(e_1)^4 \rightarrow (e_2)^3(e_1)^4(a_1)^1$ transitions increased in the order As < Sb ≈ P. The observed order of ligand field strength markedly differs from the Sb < As < P order typically found in complexes of monodentate group 15 ligands.[78] Seeking to address these inconsistencies, Venanzi and coworkers performed a series of calculations based on known crystal structures of complexes featuring tetradentate ligands at the time.[79] By constraining the apical atom of the tetradentate ligand and the metal center together via the equatorial ligands, significant distortions in both the M-E distance relative to M-E distances observed in monodentate complexes and the position of the metal center relative to the equatorial plane are observed. Due to the large radius of the antimony atom, these distortions are expected to be greatest in [**23**][BPh_4]. The distortions present in these lantern complexes may be alleviated somewhat by increasing ∡C-E-C while concomitantly reducing ∡C-C-E along the *ortho*-phenylene backbones. With regard to the electronic spectra of **21**-**23** Venanzi predicted that the energy of the a_1 level would be sensitive to these geometric distortions, resulting in the experimentally observed differences. In an effort to further to understand the ramifications of these geometric distortions on both the main group and transition metal centers, we resolved to reopen Venanzi's original investigation and obtain additional structural and computational data.

2.2 Structural characterization of nickel trisphosphinylpnictine lantern complexes

Complexes [**21**][Cl], [**22**][Cl], and **23**-Cl were synthesized according literature methods.[76] Single crystals of [**21**][Cl] and [**22**][Cl] suitable for X-ray diffraction were

grown from $CHCl_3$ solution in air. The structure of **23**-Cl was previously determined by single crystal X-ray diffraction using crystals grown from $CHCl_3$ solution. Pertinent structural metrics for **23**-Cl and [**23**][BPh_4] are taken directly from a previously published dissertation by C. R. Wade and used in the context of comparison with the structures of [**21**][Cl] and [**22**][Cl].[80]

Inspection of the structures of [**21**][Cl] and [**22**][Cl] found that both feature chloride anions that interact with proximal chloroform molecules *via* hydrogen bonding interactions, with the closest E-Cl contacts being 5.1 Å and 5.2 Å for [**21**][Cl] and [**22**][Cl], respectively Figure 29. In stark contrast, the chloride anion in **23**-Cl binds at the coordination non-innocent antimony center *trans* to the Sb-Ni bond. The observed Sb-Cl distance of 2.6835(9) Å is similar to that found in the related pentacoordinate Ph_4SbCl (Sb-Cl = 2.668(1) Å).[81] The differences in chloride anion coordination within the series suggests that only in **23**-Cl is the Lewis acidity of the apical pnictogen center sufficient to overcome the solvation of the chloride anion within $CHCl_3$. This trend is analogous to that frequently observed in tetraphenylpnictonium salts of the form [Ph_4E][X] (X = Cl, Br), whose crystal structures feature separated ion pairs when E = P,[82, 83] As[84] and direct E-X coordination when E = Sb.[44, 81, 85]

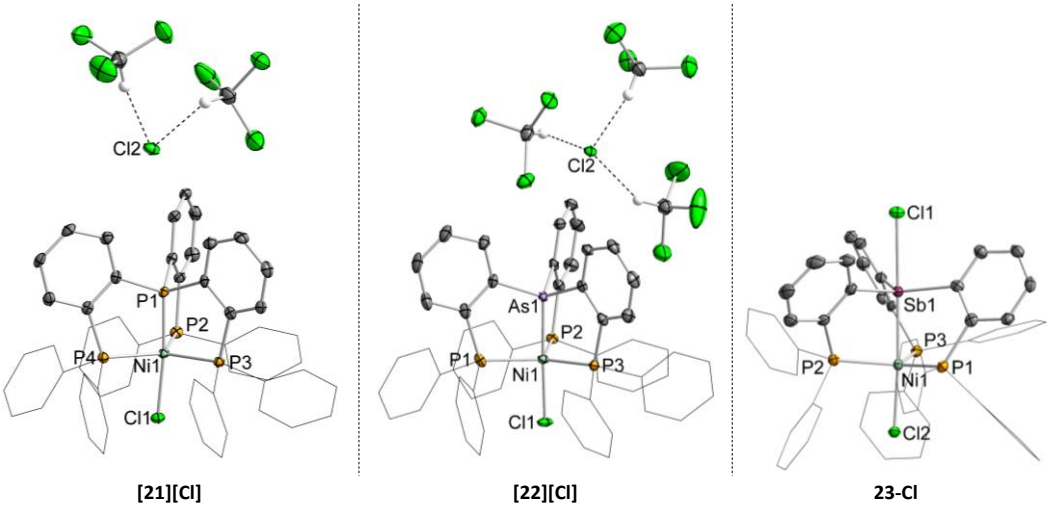

Figure 29. Structures of [**21**][Cl] (left), [**22**][Cl] (center), and **23**-Cl (right). Relevant structural features are compiled in Table **3**.

In order to better compare the geometric parameters of the Sb-Ni lantern complex with its lighter analogues, the crystal structure of [**23**][BPh_4] in which the [BPh_4]$^-$ anion does not interact with the Sb-Ni lantern is utilized.[80] Selected geometric parameters for compounds [**21**][Cl], [**22**][Cl], and [**23**][BPh_4] are compiled in Table 3.

Table 3. Selected structural features of [**21**][Cl], [**22**][Cl], and **23**-Cl.

Compound	E^a-Ni (FSR) (Å)	avg. E^a-C (Å)	Ni-P_3 plane (Å)	Ni-Cl (Å)	avg. ∡C-E^a-C (°)
[**21**][Cl][b]	2.1102(9) (0.938), 2.1122(9) (0.939)	1.824(3), 1.825(3)	0.10, 0.10	2.2184(9), 2.225(1)	107.0(1), 106.9(1)
[**22**][Cl]	2.1981(8) (0.931)	1.923(3)	0.16	2.2184(10)	108.15(13)
[**23**][BPh_4]	2.3549(9) (0.920)	2.110(7)	0.23	2.242(2)	111.2(2)

a: Listed parameters correspond to the apical pnictogen atom.
b: The crystal structure of [**21**][Cl] contains two crystallographically independent molecules within its unit cell.

In order better compare the E-Ni distances within the series, the formal shortness ratio (FSR) was calculated by dividing the observed bond distances by the sum of their constituent single-bond radii. The calculated FSR values increase with the increasing atomic number of the apical pnictogen center. In line with Venanzi's prediction, the distortion of the E-Ni FSR values from those found for sample pentacoordinate nickel complexes ligated by monodentate EPh_3 is largest when E = Sb (Table 3). Also in line with the previously predicted geometric distortions, the distance between the nickel atom and the equatorial P_3 plane increases with the atomic number of the apical pnictogen atom. The observed Ni-Cl distances increase along the series, indicating that the *trans* influence of the apical pnictogen atom is highest in the Ni-Sb compound [**23**][BPh_4].

Inspection of the average ∡C-E-C values finds that the average ∡C-Sb-C value is the largest in the series, consistent with the fact that stibines tend to undergo greater

pyramidalization than their lighter congeners. In order to assess the degree of pyramidalization of the apical pnictogen center, the Ni-Sb structures were compared to those of the free ligands (Table 4). While ligands **19**, **20**, and **7** have previously been described in the literature, **20** and **7** were not structurally characterized prior to the current investigation. Ligand **19** was previously structurally characterized by Beller[86] and coworkers, and geometric parameters from this report are used for the purpose of comparison with [**21**][Cl].

Table 4. Selected structural features of ligands **19**, **20**, and **7**.

Compound	avg. E[a]-C (Å)	avg. ∡C-E[a]-C (°)
19[b]	1.848(1)	100.57(5)
20	1.973(3)	97.7(1)
7[c]	2.171(7), 2.165(6)	94.8(3), 94.9(2)

a: Listed parameters correspond to the apical pnictogen atom.
b: Geometric parameters obtained from reference [86]
c: The crystal structure of **7** contains two crystallographically independent molecules within its unit cell.

Comparison of the crystal structures of the free ligands **19**, **20**, and **7** to those of their nickel lantern complexes finds a pair of significant changes in the geometries of their apical pnictogen atoms upon coordination. Firstly, the average apical E-C bond length decreases, with the magnitude of the decrease following the series P (Δ = 0.022-0.023 Å) < As (Δ = 0.050 Å) < Sb (Δ = 0.055-0.061 Å). Second, the average ∡C-E-C angle of the apical pnictogen atom increases, with the magnitude of the increase following the series P (Δ = 6.3-6.4°) < As (Δ = 10.5°) < Sb (Δ = 16.3-6.5°). Both of these structural changes

are consistent with the rehybridization of the apical pnictogen centers to increase p-orbital character in the E-Ni bond and consequently increase s-orbital character in the E-C bonds upon coordination to the nickel atom.[1, 87] In the context of the ability (or lack thereof) of the central pnictogen atom to engage a chloride anion in a secondary bonding interaction, the expansion of ∡C-E-C likely plays a key role, with greater distortion towards a trigonal pyramidal geometry possibly lessening the rearrangement required to accept a fifth atom into the central pnictogen atom's coordination sphere.

2.3 Computational studies

In order to further investigate the effects of the geometric distortions of the apical pnictogen atoms on the electronics of the E-Ni lantern complexes, the cations [**21**]$^+$, [**22**]$^+$, and [**23**]$^+$ were optimized by DFT methods. For each compound in the series, three principle molecular orbitals (MOs) corresponding to the axial E-Ni-Cl system were found (Figure 30). The first and lowest energy of these (Ψ_1) primarily consists of Ni-Cl and Ni-P character, with minimal contribution from the pnictogen atom. The second of these orbitals (Ψ_2) contains significant contributions from the pnictogen, nickel, and chlorine atoms, with the contributing chlorine and pnictogen orbitals being out of phase with respect to each other. Finally, the LUMO in each case (Ψ_3) consists of the fully antibonding combination of pnictogen, nickel, and chloride orbitals. The energy level of the LUMOs in the series, while similar, decrease in the order Sb (-4.317 eV) > As (-4.353 eV) ≈ P (-4.354 eV).

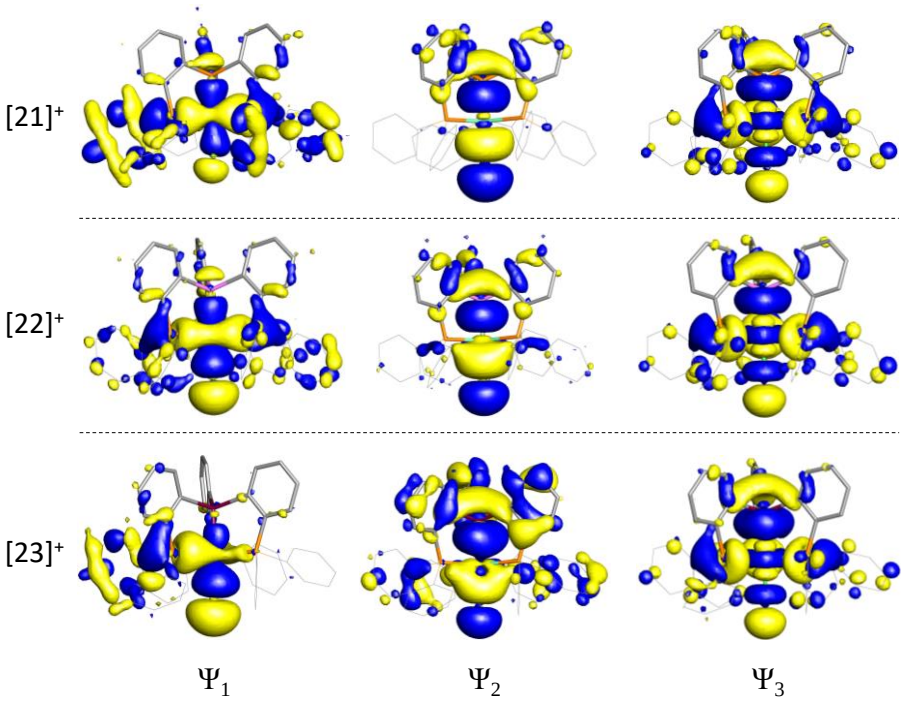

Figure 30. Plots of the calculated Ψ_1, Ψ_2, and Ψ_3 orbitals in [**21**]$^+$, [**22**]$^+$, and [**23**]$^+$ (isodensity value = 0.02).

Taken together, the character of these orbitals suggests that the axial E-Ni-Cl system may be viewed as a three-center, four-electron bond. Such systems may be viewed through the Pimentel-Rundle three center model[88, 89] or a donor-acceptor model in which the apical pnictine interacts with an antibonding combination of the nickel and chlorine atoms (Figure 31).[90] For the purpose of the following discussion, the donor-acceptor model will be utilized.

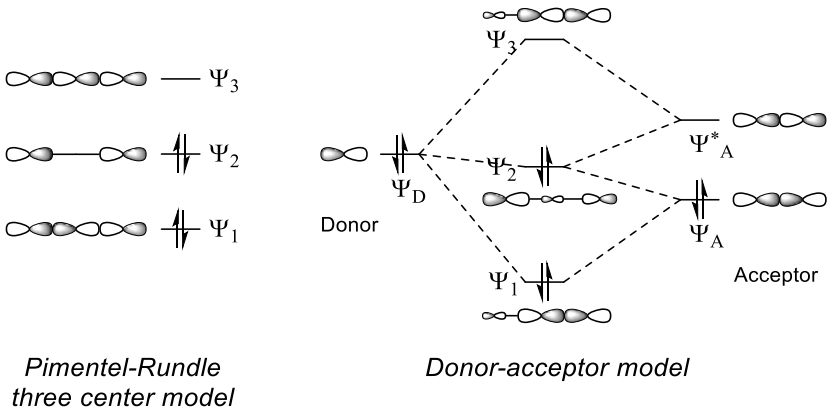

Figure 31. Diagrams illustrating the Pimentel-Rundle three center (left) and donor-acceptor model (right) for linear three center bonding.

Inspection of the atomic contributions to these MOs finds that in comparison to [**21**]$^+$ and [**22**]$^+$, [**23**]$^+$ bears markedly higher contributions from its basal pnictogen atom to Ψ_2 and Ψ_3. This trend is principally attributed to lower electronegativity and greater polarizability of antimony relative to phosphorus and arsenic, although the difference in the geometries of the pnictogen centers may also play a role. In asymmetric trihalides of the form $XICl^-$ (X = Cl, Br, I) the increasing polarizability and decreasing electronegativity of X is associated with a weakening of the I-Cl bond.[91]

Table 5. Atomic contributions from chlorine, nickel, and the basal pnictogen center to the three principal orbitals describing the E-Ni-Cl system in [**21**]$^+$ and [**22**]$^+$, [**23**]$^+$.

	Ψ_1			Ψ_2			Ψ_3		
Compound	E (%)	Ni (%)	Cl (%)	E (%)	Ni (%)	Cl (%)	E (%)	Ni (%)	Cl (%)
[**21**]$^+$	5.9	37.8	4.3	13.5	30.6	35.6	14.2	26.3	7.7
[**22**]$^+$	5.0	37.8	19.2	20.9	22.6	31.5	20.9	22.6	7.5
[**23**]$^+$	7.6	46.7	23.6	45.3	19.6	8.1	32.8	21.0	7.2

In an effort to further elucidate the differences in E-Ni bonding in the series, each compound was subjected to NBO analysis at the DFT-optimized geometry. In each case, a natural localized molecular orbital (NLMO) was found between the basal pnictogen and nickel atoms. The Ni-Cl bonds in these complexes are treated as ionic, as evidenced by the presence of donor-acceptor interactions from a formally dissociated chloride ligand to the nickel atom. Plots of the NLMOs corresponding to the E-Ni bond in [**21**]$^+$, [**22**]$^+$, and [**23**]$^+$ are qualitatively similar in appearance, being strongly localized to the pnictogen and nickel centers (Figure 32). Inspection of the NLMO composition in the natural atomic orbital (NAO) basis in [**21**]$^+$ and [**22**]$^+$ finds that the contributions from the basal pnictogen atoms are greater than those found for the nickel centers, in line with classical dative bonding (Table 6). The Sb-Ni NLMO in [**23**]$^+$, however, features a notable polarization towards the nickel center. This polarization may also be observed in the natural charge of the antimony and nickel centers, which are respectively more positive and more negative than the corresponding charges found in [**21**]$^+$ and [**22**]$^+$. While these polarization trends may be rationalized by invoking the increased electropositivity of antimony relative to phosphorus and arsenic, this polarization can also be traced to the unusual orbital makeup of the antimony contribution (45.69% s, 53.92% p) to the Sb-Ni NLMO relative to the antimony contribution to the lone pair calculated for $SbPh_3$ (68.23% s, 31.75% p).

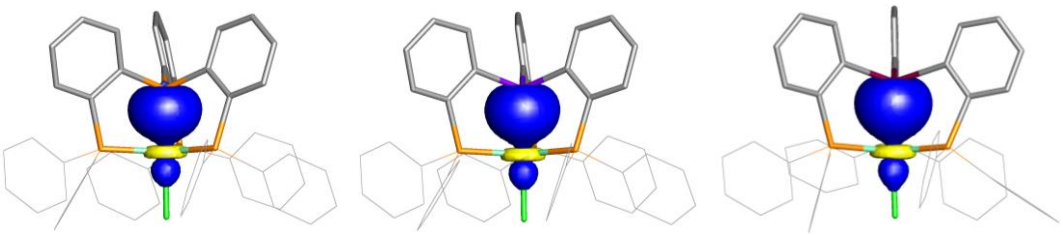

[21]$^+$ [22]$^+$ [23]$^+$

Figure 32. NLMO plots (isodensity value = 0.05) of the E-Ni bonds in [**21**]$^+$, [**22**]$^+$, and [**23**]$^+$. Hydrogen atoms are omitted, and selected phenyl groups are drawn in wireframe.

Table 6. Natural charges, NLMO contributions, and Wiberg Bond Indices (WBI) for the E-Ni interactions in [**21**]$^+$, [**22**]$^+$, and [**23**]$^+$.

Compound	E-Ni NLMO Composition (E%, Ni%)	E-Ni WBI	q_E	q_{Ni}
[**21**]$^+$	53.6% P (36.61% s, 63.01% p), 43.3% Ni	0.47	1.14	0.31
[**22**]$^+$	52.6% As (40.60% s, 59.09% p) 43.9% Ni	0.46	1.21	0.30
[**23**]$^+$	45.9% Sb (45.69% s, 53.92% p), 49.8% Ni	0.47	1.49	0.26

While the above computational studies demonstrate that the E-Ni bond is considerably more polarized towards the nickel center in [**23**]$^+$ relative to [**21**]$^+$ and [**22**]$^+$, it is unclear whether this effect is solely attributable to the greater polarizability of antimony or if the greater geometric distortion of the antimony center plays a role. In order to generalize the effects of the compression of the axial pnictogen group on the E-Ni bonding, we next examined using DFT methods a series of cations of the general form $[ClNi(PH_3)_3(EH_3)]^+$. These cations were constrained to trigonal bipyramidal geometry and the Ni-E distances to the corresponding distances found in [**21**]$^+$, [**22**]$^+$, and [**23**]$^+$ (Figure 33). By

systematically altering the value of ∡C-E-C in addition to the identity of the pnictogen atom, these systems may be used as a rudimentary model to determine how the geometric distortions observed in [**21**]$^+$, [**22**]$^+$, and [**23**]$^+$ electronically perturb the E-Ni bonds.

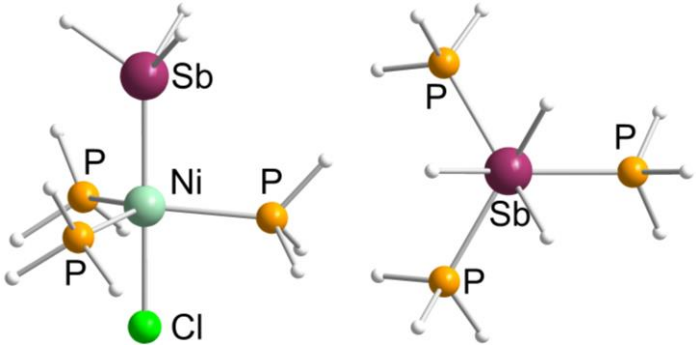

Figure 33. Ball-and-stick model of the model complex $[ClNi(PH_3)_3(SbH_3)]^+$, showing front (left) and top (right) views.

As ∡C-E-C transitions from 90° to 120°, the energy levels of Ψ_1, Ψ_2, and Ψ_3 (LUMO) show a general increase in energy level (Figure 34). While both Ψ_1 and Ψ_2 show a consistent energy level ordering of Sb > As > P, the energy level progression of ∡C-E-C of Ψ_3 is more nuanced, showing a change from P > As > Sb to Sb > As > P before finally reverting back to the original order when ∡C-E-C = 120°. This result demonstrates that as ∡C-E-C expands, the LUMO of the E-Ni-Cl system becomes a poorer acceptor from an energetic standpoint. The flip in energy level ordering of Ψ_3 upon expansion, however, does indicate a significant perturbation of the E-Ni-Cl bond system upon increasing ∡C-E-C, especially in the case of antimony. This phenomenon may indeed play a role in the anomalous electronic spectra orginially observed by Venanzi and coworkers.[77] Finally,

we note that NBO analysis finds that expansion of ∡C-E-C results in polarization of the E-Ni bond towards the nickel center, as indicated by the increasing ratio of nickel to pnictogen contributions to the E-Ni NLMO.

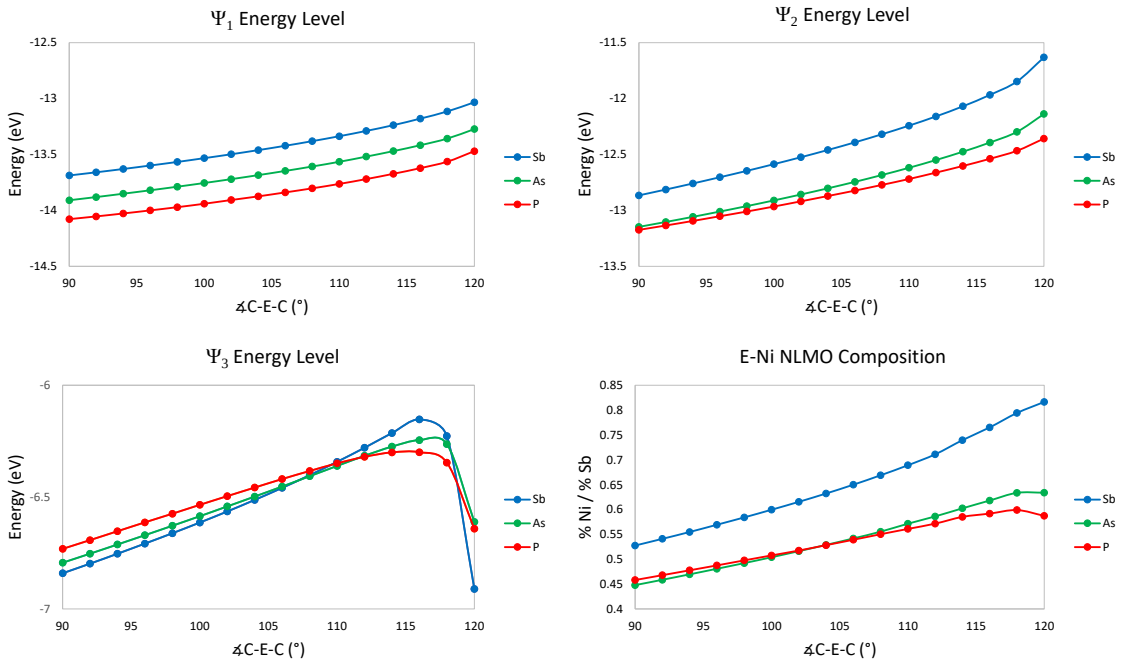

Figure 34. Changes in the energy levels of the Ψ_1 (top left), Ψ_2 (top right), and Ψ_3 (bottom left) orbitals upon increasing ∡C-E-C in the cations $[ClNi(PH_3)_3(EH_3)]^+$, where E = P, As, Sb. Changes in the composition of the E-Ni NLMO as determined by NBO analysis upon increasing ∡C-E-C. (bottom right)

2.4 Conclusions

A reinvestigation into a series of nickel lantern complexes first described by Venanzi featuring basal pnictines was undertaken. Crystal structures obtained for the previously described complexes $[ClNi((o\text{-}(Ph_2P)C_6H_4)_3E)][Cl]$ (E = P, As, Sb) found that only the

antimony derivative features a coordinated chloride ligand, in line with trends observed in the structures of tetraphenylpnictonium salts. Comparison of the structures of these complexes with those of the free ligands finds that the antimony derivative is the most distorted from its original geometry.

DFT analysis of these complexes finds that the LUMO energies of these complexes decreases in the order Sb > As ≈ P. Both DFT and NBO analysis finds that the E-Ni bond in the antimony derivative is considerably more polarized towards the nickel center relative to its phosphine and arsine analogues.

In an effort to determine the effect of changing the basal ∡C-E-C on the electronics of the lantern complexes, model complexes of the form $[ClNi(PH_3)_3(EH_3)]^+$ were employed. Expansion of ∡C-E-C is associated with a raising of the LUMO energy level and polarization of the E-Ni bond towards Ni. Thus while the geometric distortions of the basal pnictogen center may account for unusual electronic spectra previously observed by Venanzi, the ability of the antimony-based lantern complex to incorporate a fifth ligand into its coordination sphere is likely predicated on the steric effects of this distortion in addition to electrostatic considerations.

2.5 Experimental section

General Considerations. *Antimony compounds should be handled cautiously.* **19**,[92] **20**,[76] **7**,[93] [**21**][Cl],[76] **[22**][Cl],[76] and **23**-Cl[76, 80] were prepared according to previously reported procedures. All solvents were used as received.

Computational Details. Density functional theory (DFT) calculations (full geometry optimizations) were carried out on [**21**][Cl], **[22**][Cl], and **23**-Cl starting from their

respective crystal structure geometries with the Gaussian09[94] program (MPW1PW91[95] functional, with 6-31G for H, C, P, aug-ccpVTZ for P, Cl, Ni, Sb,[96] and Stuttgart relativistic small core ECPs for Sb[97]). Model complexes $[ClNi(PH_3)_3(EH_3)]^+$ were optimized at the same level of theory outlined above. The optimized structures were also subjected to natural bond orbital (NBO)[98] analysis. Calculated molecular orbitals and natural localized molecular orbitals (NLMOs) were plotted using the Jimp 2[99] program.

Crystallography. Single crystals of **7**, [**21**][Cl], and **[22**][Cl] suitable for X-ray diffraction were obtained by vapor diffusion of Et_2O into a solution of the compound in $CHCl_3$. Single crystals of **20** suitable for X-ray diffraction were obtained by vapor diffusion of Et_2O into a solution of the compound in CH_2Cl_2. Crystal data, details of data collection, and structure refinement parameters for compounds **7** and **20** are compiled in Table 7. Crystal data, details of data collection, and structure refinement parameters for compounds [**21**][Cl] and **[22**][Cl] are compiled in Table 8. The crystallographic measurements were performed at 110(2) K using a Bruker APEX-II CCD area detector diffractometer, with a graphite-monochromated Mo-Kα radiation (λ = 0.71069 Å). In each case, a specimen of suitable size and quality was selected and mounted onto a nylon loop. The semi-empirical method SADABS[100] was applied for absorption correction. The structure was solved by direct methods and refined by the full-matrix least-square technique against F^2 with the anisotropic temperature parameters for all non-hydrogen atoms. All H atoms were geometrically placed and refined in riding model approximation. Data reduction and further calculations were performed using the Bruker SAINT+[101] and SHELXTL NT[102] program packages.

Table 7. Crystal data, data collections, and structure refinements for **7**, **20**.

	$(\mathbf{7})_2$•3$CHCl_3$	**20**
Formula	$C_{111}H_{87}Cl_9P_6Sb_2$	$C_{54}H_{42}AsP_3$
Formula Weight	2169.17	858.70
Crystal Size (mm)	0.45 x 0.37 x 0.28	0.30 x 0.21 x 0.04
Crystal System	Triclinic	Triclinic
Space Group	P-1	P-1
a (Å)	15.442(5)	10.438(2)
b (Å)	15.443(5)	13.155(3)
c (Å)	22.924(8)	15.671(3)
α (°)	89.098(18)	102.724(14)
β (°)	87.977(18)	90.398(14)
γ (°)	60.383(14)	92.371(14)
V ($Å^3$)	4750(3)	2097.0(7)
Z	2	2
ρ_{calc} (g/cm^3)	1.517	1.360
μ (mm^{-1})	0.974	0.963
F(000)	2196	888
T (K)	110(2)	110(2)
Scan mode	ω, φ	ω, φ
hkl Range	-19 → 17	-14 → 14
	-19 → 19	-18 → 18
	-29 → 32	-22 → 22
Reflections collected	65695	42880
Unique reflections [Rint]	19868 [0.0489]	12481 [0.0807]
Reflns. used for refinement	19868	12481
Refined parameters	1184	523
GooF	1.058	1.005
R1[a], *w*R2[b] (all data)	0.0839, 0.2377	0.1084, 0.1654
ρ_{fin} (max., min.) (eA^{-3})	4.379, -2.737	2.352, -0.964

[a]$R1 = \sum||F_o| - |F_c||/\sum|F_o|$. [b] $wR2 ([w(F_o^2 - F_c^2)^2]/[\sum w(F_o^2)^2])^{1/2}$; $w = 1/[\sigma^2(F_o^2) + (ap)^2 + bp]$; $p = (F_o^2 + 2F_c^2)/3$ with $a = 0.1312$ for **7**, and 0.0823 for **20**; and $b = 49.1873$ for **7**, 0.0000 for **20**, and 22.8733 for **21**.

Table 8. Crystal data, data collections, and structure refinements for [**21**][Cl] and [**22**][Cl].

	([**21**][Cl])$_2$•4CHCl$_3$	([**22**][Cl]) •5CHCl$_3$
Formula	$C_{112}H_{88}Cl_{16}Ni_2P_8$	$C_{59}H_{47}AsCl_{17}NiP_3$
Formula Weight	2366.31	1585.14
Crystal Size (mm)	0.87 x 0.33 0.09	0.20 x 0.17 x 0.05
Crystal System	Monoclinic	Triclinic
Space Group	P2(1)/c	P-1
a (Å)	16.6557(13)	13.651(5)
b (Å)	21.8350(18)	15.423(5)
c (Å)	33.334(2)	16.459(6)
α (°)	90	76.245(4)
β (°)	95.711(4)	81.548(4)
γ (°)	90	87.124(4)
V (Å^3)	12062.6(16)	3329(2)
Z	8	2
ρ_{calc} (g/cm^3)	1.566	1.581
μ (mm^{-1})	1.088	1.577
F(000)	5760	1592
T (K)	110(2)	110(2)
Scan mode	ω, φ	ω, φ
hkl Range	-20 → 21	-17 → 17
	-27 → 23	-19 → 19
	-42 → 42	0 → 21
Reflns. collected	178117	38868
Unique reflns. [Rint]	25687 [0.0534]	15051 [0.0356]
Reflns. used for refinement	25687	9874
Refined parameters	1243	730
GooF	1.055	1.044
R1[a], *w*R2[b] (all data)	0.0678, 0.1444	0.0643, 0.1386
ρ_{fin} (max., min.) (eA^{-3})	2.174, -1.441	2.735, -1.719

[a] $R1 = \sum||F_o| - |F_c||/\sum|F_o|$. [b] $wR2 = ([w(F_o^2 - F_c^2)^2]/[\sum w(F_o^2)^2])^{1/2}$; $w = 1/[\sigma^2(F_o^2) + (ap)^2 + bp]$; $p = (F_o^2 + 2F_c^2)/3$ with $a = 0.0694$ for [**21**][Cl], and 0.0621 for [**22**][Cl]; and $b = 22.8733$ for [**21**][Cl], and 10.4687 for [**22**][Cl].

3. ELECTRONIC EFFECTS OF COORDINATION NON-INNOCENCE IN TRANSITION METAL STIBINES[2]

3.1 Introduction

Having established the properties which facilitate the ability of complexes of polydentate stibines to engage in coordination non-innocent behavior at their antimony centers, we next sought to better understand the effect of such secondary interactions on the Sb-M bond. Previously our group had investigated the effects of fluoride coordination on the Sb-Pd bond in the cationic Pd-Sb complex [**9**][BPh_4].[49] Boys localization analysis[103] of the Sb-Pd bond in [**9**]$^+$ and its fluoride adducts **9**-F at the ADF/BP86/TZP+ZORA level of theory found that fluoride coordination induces a strong polarization of the Sb-Pd bond towards the palladium center.

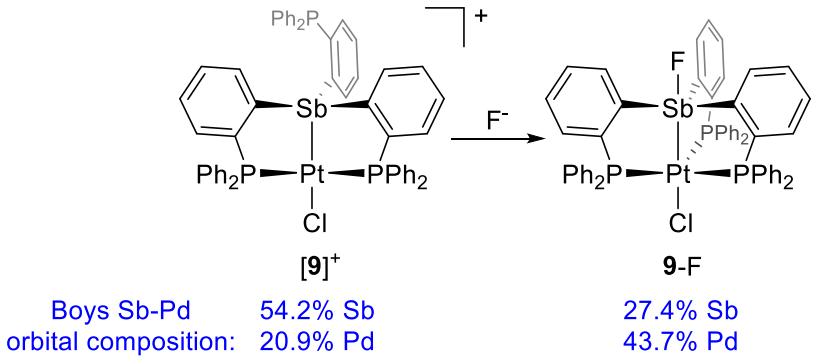

Figure 35. Change in Sb-Pd bond composition in [**9**]$^+$ and **9**-F *per* Boys localization analysis.

[2] Reprinted in part with permission from, "Guilty on two counts: stepwise coordination of two fluoride anions to the antimony atom of a noninnocent stibine ligand"; Jones, J. S.; Wade, C. R.; Gabbaï, F. P. *Organometallics* **2015**, *54*, 2647, Copyright 2015 by the American Chemical Society.

Building upon the this work, a more detailed computational study by Sakaki and coworkers on [**8**][BMe_4] and [**9**][BMe_4], and their fluoride adducts **8**-F and **9**-F found that upon fluoride coordination, the electron populations of the Pd-Cl subunits increase.[104] The electron populations of the antimony centers decrease upon fluoride coordination, in line with the increased donicity of the antimony ligand upon attaining a hypervalent configuration. Further evidence for the enhanced donicity of antimony ligand upon fluoride binding is found in the structures of a series of nickel lantern complexes which vary by their apical donor atoms (Table 9). Utilizing the length of the Ni-Cl bond *trans* to the apical donor atom as a measure of its *trans* influence, the *trans* influence of the antimony ligands in **23**-Cl and **23**-F[80] are comparable to that found in the trisphosphinylsilyl nickel lantern complex ClNi((*o*-(Ph_2P)C_6H_4)$_3$Si) **24** containing the strong *trans* influence ligand $[SiPh_3]^-$.[105]

Table 9. Ni-Cl bond lengths in selected Ni lantern complexes.

Compound	Apical Donor Atom	Ni-Cl distance (Å)
[ClNi((*o*-(Ph_2P)C_6H_4)$_3$P)][BPh_4] ([**21**][BPh_4])	P	2.2183(8)
[ClNi((*o*-(Ph_2P)C_6H_4)$_3$As)][BPh_4] ([**22**][BPh_4])	As	2.2184(10)
[ClNi((*o*-(Ph_2P)C_6H_4)$_3$Sb)][BPh_4] ([**23**][BPh_4])	Sb	2.2423(16)
ClNi((*o*-(Ph_2P)C_6H_4)$_3$Sb)-Cl (**23**-Cl)	Sb	2.2813(9)
ClNi((*o*-(Ph_2P)C_6H_4)$_3$Sb)-F (**23**-F)	Sb	2.2684(12)
ClNi((*o*-(Ph_2P)C_6H_4)$_3$Si) **24**	Si	2.2806(5)

In an effort to further systematically probe the effects of antimony ligand coordination non-innocence on the properties of the coordinated metal, we describe a series of three Pt-Sb lantern complexes that differ by sequential coordination of fluoride at their antimony centers.

3.2 Synthesis and anion exchange reactivity of a Pt-Sb lantern complex

As a starting point in our investigation, we turned our attention to the Sb-Pt lantern complexes **25**-Cl and **25**-F previously described in a dissertation by C. R. Wade (Figure 36).[80] Pertinent spectroscopic and structural metrics for **25**-Cl and **25**-F are taken directly from the aforementioned dissertation used in the context of comparison with original computational data and compounds subsequently derived from **25**-Cl.

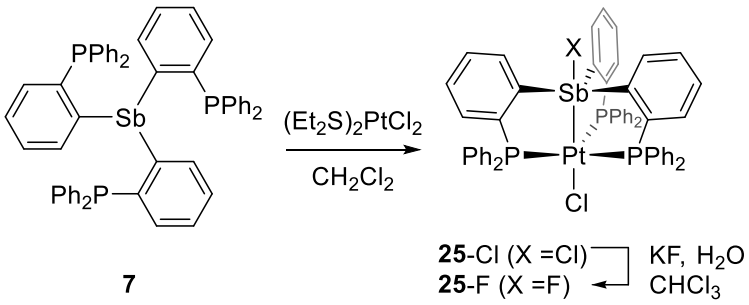

Figure 36. Synthesis and anion exchange of **25**-Cl as previously described by C. R. Wade.[80]

Despite undergoing chloride-for-fluoride anion metathesis at its antimony center, the crystal structures of **25**-Cl and **25**-F show little variation in their Sb-Pt (**25**-Cl: 2.5732(5) Å, **25**-F: 2.5783(7) Å) or Pt-Cl (**25**-Cl: 2.472(2) Å, **25**-F: 2.4493(12) Å) distances. To

further investigate whether the anion exchange at the coordinated antimony center induces an electronic perturbation of the Sb-Pt bond, both **25**-Cl and **25**-F were optimized by DFT methods, and subsequently subjected to natural bond orbital (NBO) analysis.

For both **25**-Cl and **25**-F, NBO analysis finds a natural localized molecular orbital (NLMO) corresponding to the Sb-Pt interaction (Figure 37). Inspection of the atomic contributions to the NLMO indicates that chloride-for-fluoride exchange at the antimony center results in a marked polarization of the bonding pair towards the platinum center (38.0% Sb/ 53.7% Pt in **25**-Cl, 29.1% Sb/ 66.5% Pt in **25**-F). Although the Sb-Pt core undergoes a change in polarization, the Wiberg bond index (WBI) of the Sb-Pt bond remains nearly unchanged (0.43 in **25**-Cl, 0.44 in **25**-F). In contrast, the WBI of the Pt-Cl bond changes from 0.2689 in **25**-Cl to 0.2569 in **25**-F, reflecting a slight weakening of the bond in response to the polarization of the Sb-Pt bond. The change in bonding from **25**-Cl to **25**-F was also investigated by a Quantum Theory of Atoms in Molecules (QTAIM) analysis, which identifies bond critical points (BCPs) between the antimony and platinum atoms in both **25**-Cl and **25**-F (Figure 37). Consistent with the overall lack of change in the strength of the Sb-Pt interaction upon conversion of **25**-Cl to **25**-F, the values of the electron density at the bond critical point (ρ_{BCP}) and the integrations of the electron density across the Sb-Pt interatomic surfaces ($\oint_{Sb \cap Pt} \rho(r)$) vary little between the two compounds (Table 10).

Despite the above computational data suggesting that chloride-for-fluoride exchange at the antimony centers in **25**-Cl to **25**-F, there remains a discrepancy in the $^{1}J_{Pt\text{-}P}$ coupling constants observed in their solution phase $^{31}P\{^{1}H\}$ NMR spectra ($CDCl_3$, **25**-Cl: $^{1}J_{Pt\text{-}P}$ =

2305 Hz, **25**-F: $^{1}J_{Pt\text{-}P}$ = 3204.6 Hz, Such variations in $^{1}J_{Pt\text{-}P}$ coupling constants are typically observed upon changes in the oxidation state of the platinum atom, and in this case indicate a significant electronic perturbation upon chloride-for-fluoride exchange.[69, 106-110] The computational data derived from the solid state structures may be reconciled with the observed $^{1}J_{Pt\text{-}P}$ coupling constants by invoking the weaker binding of the chloride anion to the antimony relative to the fluoride anion in solution, with **25**-Cl being considerably more dissociated in solution than **25**-F.

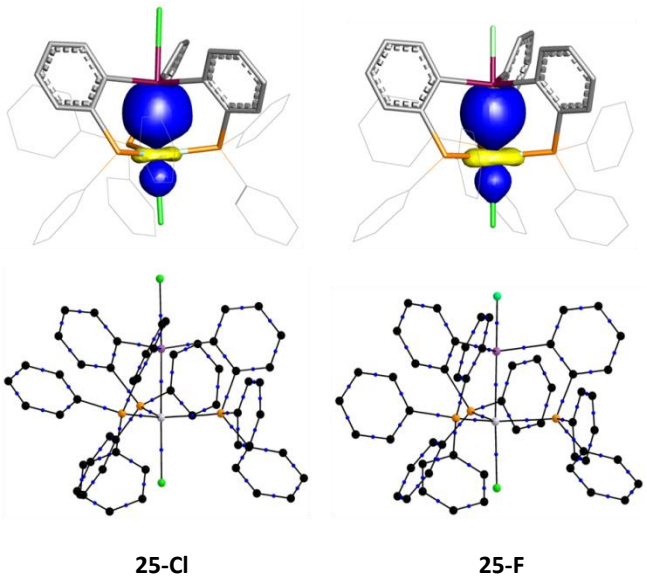

Figure 37. NLMO and QTAIM plots for **25**-Cl and **25**-F. Above: NLMO plots (isodensity value = 0.05) of the Sb-Pt bonds in **25**-Cl and **25**-F. Hydrogen atoms are omitted, and selected phenyl groups are drawn in wireframe. Below: DFT-optimized structures of **25**-Cl and **25**-F. Bond critical points located *via* QTAIM analysis are shown as blue dots. Hydrogen atoms and bond critical points featuring ρ values less than 0.20 e Å^{-3} and their corresponding bond paths are omitted.

Table 10. Selected features of the electron distribution function at bond critical points of **25**-Cl and **25**-F.

Bond (A-B)	d (Å)	$d_{A\text{-}BCP}$ (Å)	$d_{B\text{-}BCP}$ (Å)	ρ_{BCP} (e Å^{-3})	δ(A,B)	$\oint_{A\cap B}\rho(r)$ (e Å^{-1})
Compound **25**-Cl						
Sb-Pt	2.596	1.232	1.364	0.58	0.79	1.81
avg. Sb-C	2.163	1.101	1.062	0.74	0.77	1.57
Sb-Cl	2.641	1.250	1.391	0.36	0.45	1.02
Pt-Cl	2.452	1.211	1.241	0.51	0.76	1.50
Compound **25**-F						
Sb-Pt	2.597	1.231	1.366	0.57	0.79	1.71
avg. Sb-C	2.148	1.087	1.061	0.76	0.74	1.63
Sb-F	2.044	1.053	0.991	0.61	0.46	1.35
Pt-Cl	2.461	1.216	1.245	0.50	0.74	1.46

3.3 Synthesis of a series of Pt-Sb lantern complexes separated by sequential fluoride addition.

Interested in the possibility of generating a dicationic, highly Lewis acidic derivative, we next examined the reactivity of **25**-Cl with $AgSbF_6$ as a halide abstracting agent. To facilitate this process, the reaction was carried out in the presence of an isonitrile donor ligand which we envisioned would help stabilized the platinum center. Treatment of **25**-Cl with two equivalents of $AgSbF_6$ in the presence of one equivalent of CyNC produced the dicationic complex [**26**]$^{2+}$ as the hexafluoroantimonate salt (Figure 38). The ^{31}P NMR spectrum of [**26**]$^{2+}$ in $CDCl_3$ shows a singlet at 28.86 ppm bordered by ^{195}Pt satellites ($^1J_{Pt\text{-}P}$ = 2330 Hz). The corresponding ^{195}Pt NMR resonance appears as a quartet at -5381 ppm. The relatively high C-N stretching frequency of 2214 cm^{-1} observed in the solid state IR spectrum of [**26**][SbF_6]$_2$ (free ν_{CyNC} = 2140 cm^{-1})[111] is comparable to that found in *cis*-

$PtCl_2(CNCy)_2$ (ν_{CyNC} = 2227 cm^{-1}),[112] suggesting that the isocyanide ligand predominately acts as a σ donor towards the cationic platinum center. The absence of significant π-back-bonding may be assigned to the dicationic nature of the complex.

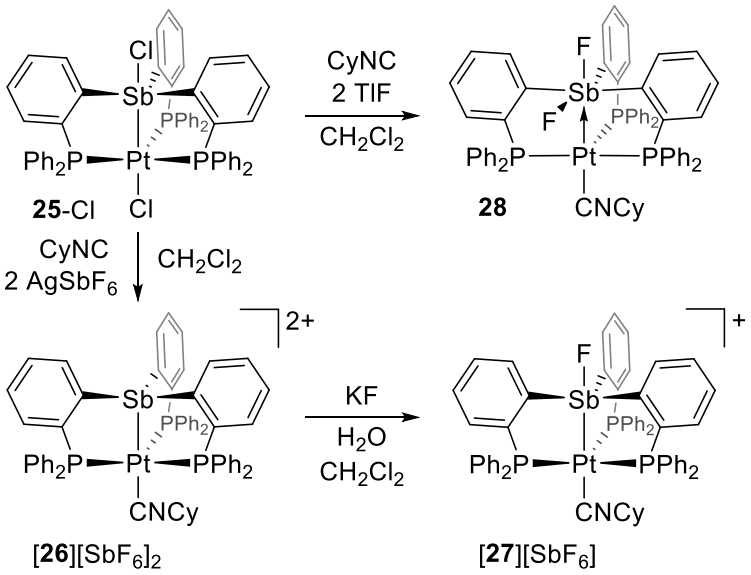

Figure 38. Synthesis of [**26**]$^{2+}$, [**27**]$^{+}$, and **28**.

The crystal structure of [**26**][SbF_6]$_2$ revealed that the antimony center adopts a distorted tetrahedral geometry (Figure 3). The large sum of C-Sb-C angles (Σ∢= (C-Sb-C) = 339.6 °) indicates a low degree of pyramidalization at the antimony center, which is consistent with the increased hybridization of the antimony center upon formation of a classical $R_3Sb\rightarrow Pt$ coordination bond.[113] The platinum center shows a trigonal bipyramidal geometry, as indicated by the sum of the P-Pt-P angles (Σ∢= (P-Pt-P) = 357.4(2) °). The coordination of all three phosphine arms of the ligand **7** to the platinum center in [**26**]$^{2+}$

stands in contrast to the related monocationic [(*o*-(Ph_2P)C_6H_4)$_3$SbPdCl][BPh_4] ([**9**][BPh_4]),[49] in which one of the phosphine arms does not coordinate in the solid state. The Sb-Pt separation of 2.4706(5) Å is shorter than that found in **25**-Cl (2.5732(5) Å), which may be attributed to the lower coordination number and the octet configuration of the antimony center in [**26**]$^{2+}$. The isonitrile ligand is coordinated axially to the platinum center via a Pt-C55 bond of 1.993(6) Å. The N1-C55 distance of 1.144(8) Å shows no notable lengthening when compared to that of the free 1,4-dicyanocyclohexane (1.141(2) Å),[114] and the C55-N1-C56 angle of 174.0(7)° deviates only slightly from linearity, in agreement with the absence of strong back-bonding. Finally, in contrast to **25**-Cl, [**26**]$^{2+}$ exhibits low helicity, as indicated by the average P-Pt-Sb-C torsion angle of 5.3 °.

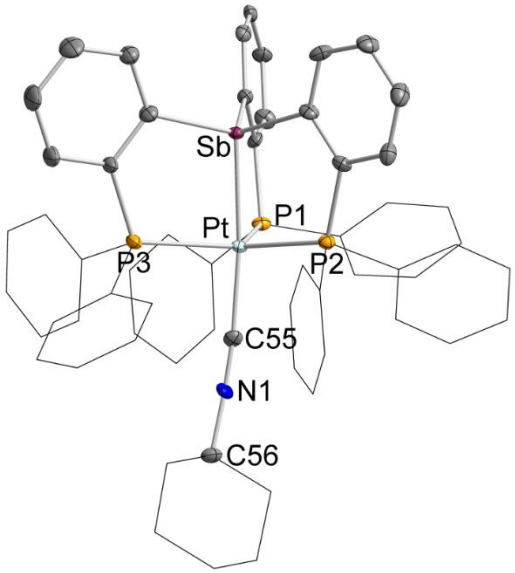

Figure 39. Solid state structure of [**26**][SbF_6]$_2$. Thermal ellipsoids are drawn at the 50% probability level. Selected phenyl groups and the cyclohexyl group are drawn in wireframe, and hydrogen atoms, solvent molecules, and SbF_6 anions are omitted for clarity. Selected bond lengths (Å) and angles (°): Sb-Pt 2.4706(5), Pt-C55 1.993(6), N1-C55 1.144(8), Sb-Pt-C55 173.0(2), P1-Pt-P2 113.77(6), P1-Pt-P3 114.97(6), P2-Pt-P3 128.69(6), C55-N1-C56 174.0(7).

With [**26**]$^{2+}$ in hand, we decided to probe the Lewis acidic behavior of this molecule with fluoride anions. Layering a CH_2Cl_2 solution of [**26**][SbF_6]$_2$ with an aqueous KF solution and agitating the resulting biphasic reaction mixture afforded the cationic monofluoro complex [**27**]$^+$ as the hexafluoroantimonate salt (Scheme 2). The ^{31}P NMR spectrum of [**27**]$^+$ in $CHCl_3$ displays a doublet ($^3J_{P\text{-}F}$ = 12.82 Hz) at 39.67 ppm, which is flanked by ^{195}Pt satellites ($^1J_{Pt\text{-}P}$ = 2964 Hz). The corresponding ^{195}Pt NMR resonance is found as a quartet at -5143 ppm. Similar to that observed in the conversion of **25**-Cl to **25**-F, the magnitude of the $^1J_{Pt\text{-}P}$ coupling constant in [**27**]$^+$ is notably larger than in [**26**]$^{2+}$ ($^1J_{Pt\text{-}P}$ = 2330 Hz), suggesting that the platinum center in [**27**]$^+$ is more reduced relative to

[**26**]$^{2+}$.[69, 106-110] The ^{19}F NMR spectrum of [**27**]$^{+}$ exhibits a resonance at -128.59 ppm, which occurs as a mutliplet due to unresolved coupling. The solid state CyNC C-N stretching frequency of 2196 cm^{-1} in [**27**]$^{+}$ is noticeably lower than that found for [**26**]$^{2+}$ (ν_{CyNC} = 2214 cm^{-1}), again suggesting that the platinum center is more electron rich. Presumably, coordination of the fluoride to the antimony center increases the σ-donor properties of the antimony ligand, leading to a greater shift of electron density toward platinum.

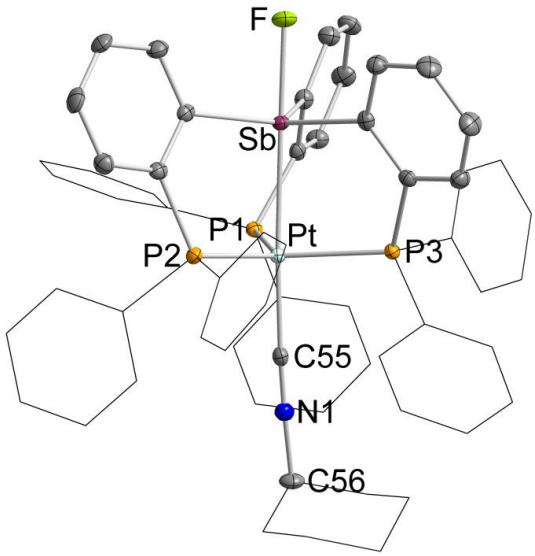

Figure 40. Solid state structure of [**27**][SbF_6]. Thermal ellipsoids are drawn at the 50% probability level. Selected phenyl groups and the cyclohexyl group are drawn in wireframe, and hydrogen atoms and the SbF_6 anion are omitted for clarity. Selected bond lengths (Å) and angles (°): Sb-Pt 2.6236(3), Sb-F 2.043(2), Pt-C55 2.016(4), N1-C55 1.141(5), Sb-Pt-C55 174.3(1), P1-Pt-P2 122.72(3), P1-Pt-P3 116.56(3), P2-Pt-P3 118.47(3), C55-N1-C56 176.1(4).

A single crystal X-ray diffraction study of [**27**][SbF_6] confirmed the coordination of fluoride at the antimony center (Figure 40). The antimony center assumes a trigonal

bipyramidal geometry, as indicated by the sum of the C-Sb-C angles ($\Sigma\measuredangle$(C-Sb-C) = 356.0(4) °). The Sb-F distance of 2.043(2) Å is similar to those found in the pentacoordinate antimony derivatives such as Ph_4SbF (2.0530(8) Å)[115] or [(*o*-$(Ph_2P)C_6H_4)_3FSbPdCl$] (2.0320(19) Å, **9**-F), yet slightly longer that found in Ph_3SbF_2 (1.969(2)-1.978(2) Å).[116] Coordination of fluoride at the antimony center also induces an increase in the Sb-Pt separation from 2.4705(5) Å in $[\mathbf{26}]^{2+}$ to 2.6236(3), which is attributed to the increased coordination number and hypervalence of the Sb center. Fluoride coordination at the antimony center also results in increased helicity of the lantern complex, as evidenced by the average P-Pt-Sb-C torsion angle of 21.0 °. The metrical parameters of the isonitrile ligand are comparable to those in $[\mathbf{26}]^{2+}$, possibly indicating that the electronic changes at platinum are not sufficient to impact the structure of this ligand.

With compound $[\mathbf{27}]^+$ in hand, we next sought to explore whether the antimony or platinum centers could coordinate an additional equivalent of fluoride. The ^{31}P NMR spectrum of a solution containing $[\mathbf{27}]^+$ and $[Ph_3SiF_2][n\text{-}Bu_4]$ in CH_2Cl_2 showed the appearance of a new species (**28**) characterized by a triplet at 27.44 ppm and a doublet at 47.40 ppm ($^2J_{P\text{-}P}$ = 132.61 Hz). The appearance of the two coupled resonances suggested a break in the C_3 symmetry of the core and formation of a new species (**28**). Compound **28** was isolated from the reaction of **25**-Cl with CyNC and two equivalents of TlF in CH_2Cl_2 (Scheme 2). Compound **28** is a moisture-sensitive solid that decomposes slowly in CH_2Cl_2 and $CHCl_3$ solutions. The ^{31}P NMR spectrum recorded for the isolated compound shows that the resonances at 27.55 ppm and 47.40 ppm feature ^{195}Pt NMR

satellites with respective $^{1}J_{Pt\text{-}P}$ coupling constants of 2888 and 3351 Hz (Figure 41). These elevated coupling constants, which are either comparable or larger than that in [**27**]$^{+}$, again speak to the apparent reduced state of the platinum center. A closer inspection of the ^{31}P NMR spectrum shows further unresolved splitting which arises from coupling with the antimony bound fluoride atoms. The ^{19}F NMR spectrum displays two resonances at -20.73 and -135.97 ppm which appear in a 1:1 ratio. As in the case of the ^{31}P NMR spectrum, both signals show further coupling which could not be fully resolved. The peak at -135.97 ppm can be described as a doublet with a $^{2}J_{F\text{-}F}$ of 67.39 Hz. Based on a comparison with the chemical shift of the fluorine nucleus in [**27**]$^{+}$, this peak is assigned to the fluorine atom *trans* from the platinum atom. The fluorine resonance at -20.73 is split into a doublet ($^{2}J_{F\text{-}F}$ = 67.39 Hz) and bordered by ^{195}Pt satellites ($^{2}J_{F\text{-}F}$ = approx. 66 Hz). The corresponding ^{195}Pt NMR signal of **28** appears as a broad triplet of doublets at -5136 ppm. The observed CyNC C-N stretching frequency of 2181 cm^{-1} in **28** is lower than that observed for both [**26**]$^{2+}$ (ν_{CyNC} = 2214 cm^{-1}) and [**27**]$^{+}$ (ν_{CyNC} = 2196 cm^{-1} cm^{-1}) again suggesting an increase in electron density at the platinum center.

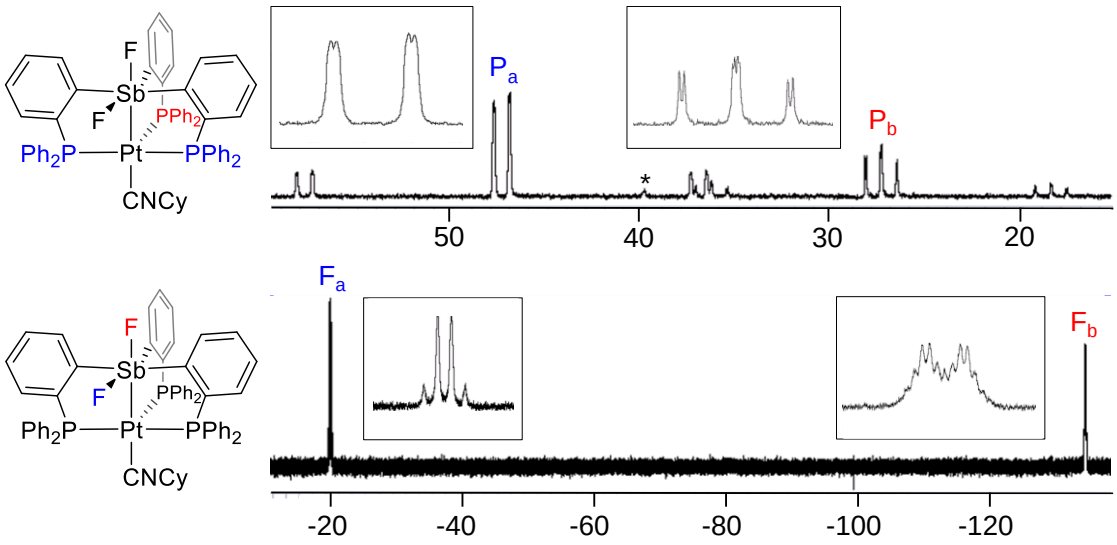

Figure 41. ^{31}P (top) and ^{19}F NMR spectra (bottom) of **28** in CD_2Cl_2. The peak marked by an asterisk shows the presence of a decomposition product. Insets show magnified views of individual resonances.

The solid state structure of **28** confirmed that the formation of a difluorostiborane (Figure 6). The antimony center in **28** adopts a distorted octahedral geometry (∡(C19-Sb-C37) = 163.8(2), ∡(C1-Sb-F2) = 168.6(2)°, ∡(F1-Sb-Pt) = 178.2(1)°) reminiscent of that in the core-isoelectronic gold complex **11**. The Sb-F bonds lengths of 2.027(4) and 2.011(4) Å are similar to the Sb-F bond found in [**27**]$^+$, again indicating relatively strong coordination of the two fluoride ligands to the antimony center. The Sb-Pt separation in **28** increases only slightly to 2.6568(6) Å from 2.6236(3) Å in [**27**]$^+$. Despite the geometry change at the antimony center, the trigonal bipyramidal geometry of the Pt center remains unperturbed, as indicated by the sum of the P-Pt-P angles (Σ∡(P-Pt-P) = 357.6(2)°). The metrical parameters of the isonitrile ligand again are comparable to those in [**26**]$^{2+}$ and

[**27**]$^{+}$ indicating that the electronic changes at platinum are not sufficient to impact the structure of this ligand.

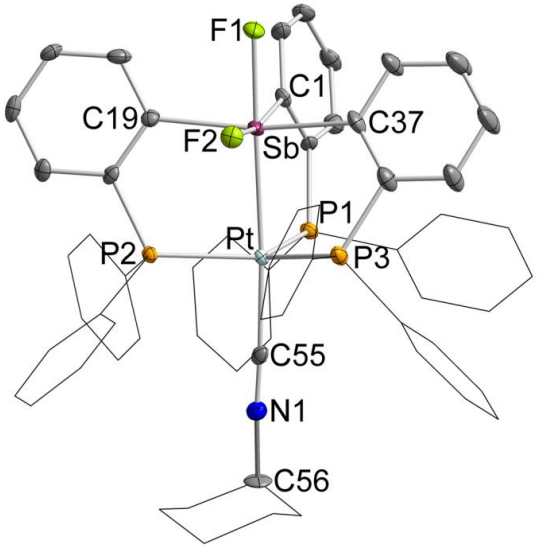

Figure 42. Solid state structure of **28**. Thermal ellipsoids are drawn at the 50% probability level. Selected phenyl groups and the cyclohexyl group are drawn in wireframe, and hydrogens and solvent molecules are omitted for clarity. Selected bond lengths (Å) and angles (°): Sb-Pt 2.6568(6), Sb-F1 2.027(4), Sb-F2 2.011(4), Pt-C55 2.013(6), N1-C55 1.154(8), Sb-Pt-C55 176.59(18), P1-Pt-P2 111.96(6), P1-Pt-P3 124.21(6), P2-Pt-P3 121.48(6), Pt-Sb-F1 178.2(1), C1-Sb-F2 168.6(2), C19-Sb-C37 163.8(2), C55-N1-C56 175.4(7).

3.4 Theoretical investigation into the perturbation of the Pt-Sb bond by fluoride binding.

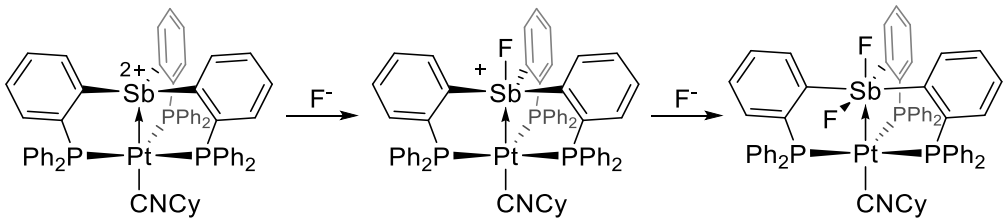

Figure 43. Extreme bonding descriptions of [**26**]$^{2+}$, [**27**]$^{+}$, and **28**.

The stepwise coordination of two fluoride anions to the antimony center of [**26**]$^{2+}$ indicates that this center is the most Lewis acidic in the molecule. In one extreme, this reactivity could be interpreted on the basis of a structure in which the antimony atom is a dication stabilized by a dative interaction with a reduced platinum center (Figure 43).[117] To probe this idea and better understand the polarization of the electron density at the core of these complexes, we carried out a series of DFT calculations. Complexes [**26**]$^{2+}$, [**27**]$^{+}$, and **28** were subjected to optimization by DFT methods and analyzed using the NBO method. Selected properties of the Sb-Pt interactions derived from the NBO analyses are compiled in Table 11. For each compound in the series, a NLMO corresponding to the Sb-Pt interaction was found (Figure 44). These NLMOs all feature significant polarization of the bonding pair towards the platinum center, as evidenced by the elevated contribution from platinum towards the NLMO makeup.

Table 11. Natural charges, NLMO contributions, and Wiberg Bond Indices (WBI) for the Sb-Pt interactions in [**26**]$^{2+}$, [**27**]$^{+}$, and **28**.

Compound	q_{Sb}	q_{Pt}	NLMO %Sb/%Pt	WBI
[**26**]$^{2+}$	1.59	0.28	38.4/57.8	0.58
[**27**]$^{+}$	1.84	0.23	34.8/56.1	0.46
28	2.08	0.24	29.9/60.2	0.42

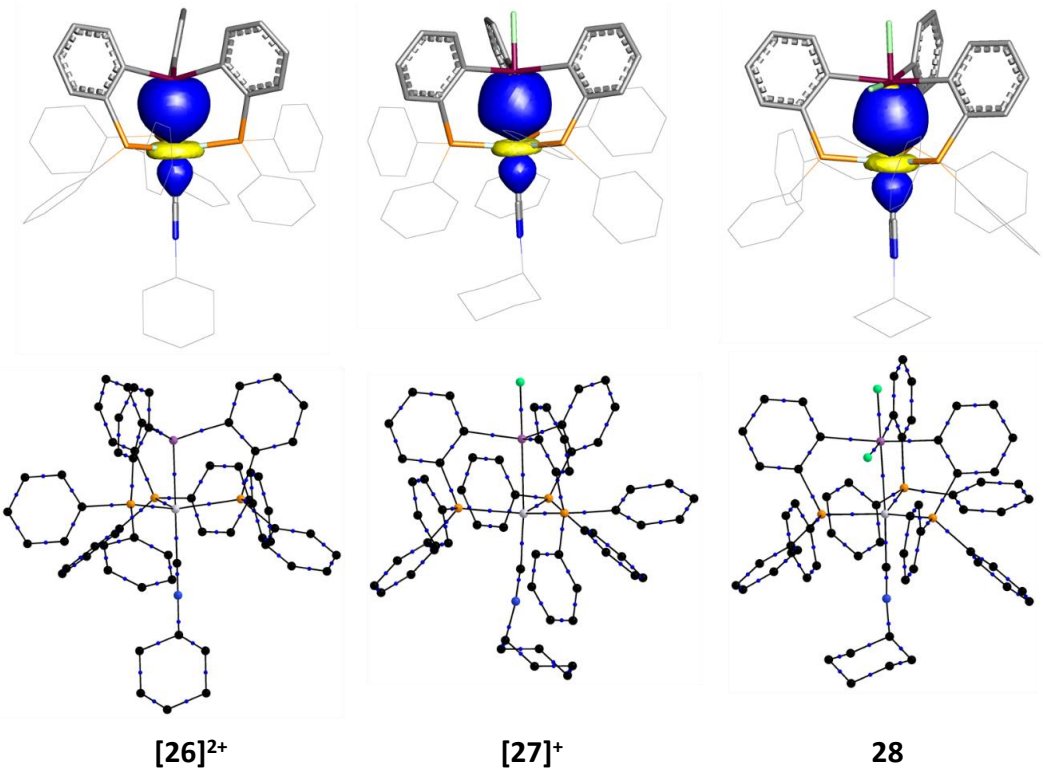

Figure 44. NLMO and QTAIM plots for [**26**]$^{2+}$, [**27**]$^{+}$, **28**. Above: NLMO plots (isodensity value = 0.05) of the Sb-Pt bonds in [**26**]$^{2+}$, [**27**]$^{+}$, **28**. Hydrogen atoms are omitted, and selected cyclohexyl and phenyl groups are drawn in wireframe for clarity. Below: DFT-optimized structures of [**26**]$^{2+}$, [**27**]$^{+}$, and **28**. Bond critical points located *via* QTAIM analysis are shown in as blue dots. Hydrogen atoms and bond critical points featuring ρ values less than 0.20 e Å^{-3} and their corresponding bond paths are omitted for clarity.

This simple computational result shows that all three compounds can be described on the basis of two main resonance structures (Figure 45). The preponderant contributing structure is that corresponding to a complex with a covalent Sb-Pt bond (resonance form a). However, the distinct polarization of the bonding pair toward platinum in all three structures suggests that the second contributing resonance structure is the $Pt^{0}Sb^{V}$ form b. The computational results also establish that a more classically accepted $Sb^{III}\rightarrow Pt^{II}$ resonance form is not a strong contributor. Inspection of the contribution of antimony and platinum to the NLMO makeup shows that the contribution of resonance form b increases from $[\mathbf{26}]^{2+}$ to $[\mathbf{27}]^{+}$ to **28**. With this increased contribution, the Sb-Pt bond adopt an increasing Sb←Pt character, with the difluorostiborane moiety of **28** formally behaving as a Z-ligand.[18-20, 24, 118-127]

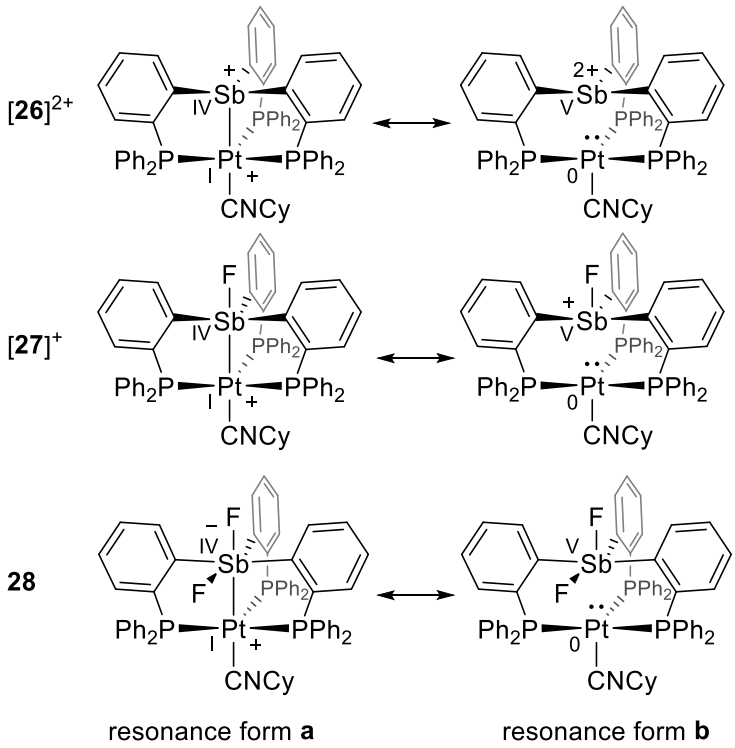

Figure 45. Contributing resonance structures for compounds [**26**]$^{2+}$, [**27**]$^{+}$, and **28**.

The natural charges found on platinum decreases notably upon coordination of the first fluoride anion and remains almost the same in [**27**]$^{+}$ and **28**. The natural charge on the antimony center increases, consistent with charge-density rules put forth by Gutmann. The accepting atoms of polyatomic acids, the antimony center in this case, experience a net decrease in electron density due to a "spillover" of density towards the peripheral substituents, one of them being the platinum center.[128, 129] Finally, the WBI values for the Sb-Pt interactions decreases across the series from 0.58 in [**26**]$^{2+}$ to 0.46 in [**27**]$^{+}$ to 0.42 in **28** as the contribution of resonance form b becomes more important.

In order to further investigate the changes in bonding in the Sb-Pt core upon coordination of successive equivalents of fluoride, we turned to a QTAIM[130] analysis of [**26**]$^{2+}$, [**27**]$^{+}$, and **28**. Relevant features of the electron density distribution function at selected bond critical points are presented in Table 12. In all cases, a BCP was located between the antimony and platinum centers (Figure 44). Examination of the values of ρ_{BCP} for the Sb-Pt bonds in the series finds a modest decrease from 0.65 e Å^{-3} in [**26**]$^{2+}$ to 0.47 e Å^{-3} in **28**, indicating a decrease in Sb-Pt bond strength upon coordination of fluoride to the antimony center. This conclusion is corroborated by the values of $\oint_{Sb\cap Pt}\rho(r)$, which decrease from 2.00 e Å^{-1} in [**26**]$^{2+}$, to 1.59 e Å^{-1} in [**27**]$^{+}$, and finally to 1.48 e Å^{-1} in **28**. The notable differences in the magnitude of the $\oint_{Sb\cap Pt}\rho(r)$ decrease upon successive coordination of fluoride anions to the antimony center suggests that the first fluoride coordination effects a greater weakening of the Sb-Pt bond relative to the coordination of the second equivalent of fluoride. Inspection of the ρ_{BCP} and $\oint_{Sb\cap C}\rho(r)$ values for the Sb-C bonds reveals that both metrics also decrease modestly upon successive fluoride coordination, consistent with the hypervalent configuration and increasing coordination number of the antimony center. The opposite trend, however, is observed for the Sb-F bonds, which display a slight increase in both ρ_{BCP} and $\oint_{Sb\cap F}\rho(r)$ values upon coordination of the second fluoride equivalent. The values of the delocalization index (δ(A,B)),[131] which corresponds to the number of electron pairs delocalized between atomic pairs, provide another useful tool for investigating the bonding present in the Sb-Pt cores of [**26**]$^{2+}$, [**27**]$^{+}$, and **28**. δ(Sb,Pt) falls from 0.93 in [**26**]$^{2+}$ to 0.63 in **28**, indicating that the bonding pair is less equally shared between the two atoms upon successive coordination

of fluoride.[132] This trend is consistent with both the polarization of the Sb-Pt interaction and the increasing delocalization of the Sb-Pt bonding pair throughout the molecule. Accordingly, the ratio of the Sb-BCP distance to the Sb-Pt distance decreases slightly from [**26**]$^{2+}$ to **28**, suggesting moderate polarization of the Sb-Pt bond towards the platinum center.

Table 12. Selected features of the electron density distribution function at bond critical points of [**26**]$^{2+}$, [**27**]$^{+}$, and **28**.

Bond (A-B)	d (Å)	$d_{A\text{-}BCP}$ (Å)	$d_{B\text{-}BCP}$ (Å)	ρ_{BCP} (e Å^{-3})	δ(A,B)	$\oint_{A\cap B}\rho(r)$ (e Å^{-1})
Compound [**26**]$^{2+}$						
Sb-Pt	2.494	1.225	1.269	0.65	2.00	0.92
avg. Sb-C	2.103	1.077	1.026	0.81	1.74	0.83
Pt-C	1.963	0.909	1.054	1.01	1.05	2.34
Compound [**27**]$^{+}$						
Sb-Pt	2.666	1.278	1.388	0.52	1.59	0.72
avg. Sb-C	2.147	1.087	1.060	0.76	1.59	0.75
Sb-F	2.037	1.049	0.988	0.62	1.34	0.47
Pt-C	1.988	1.071	0.917	0.96	1.02	2.35
Bond (A-B)	d (Å)	$d_{A\text{-}BCP}$ (Å)	$d_{B\text{-}BCP}$ (Å)	ρ_{BCP} (e Å^{-3})	δ(A,B)	$\oint_{A\cap B}\rho(r)$ (e Å^{-1})
Compound **28**						
Sb-Pt	2.733	1.297	1.436	0.47	1.48	0.63
avg. Sb-C	2.187	1.088	1.098	0.71	1.56	0.62
avg. Sb-F	2.012	1.088	1.098	0.71	1.56	0.62
Pt-C	1.986	1.073	0.913	0.96	1.05	2.34

3.5 Conclusions

In summary, we present a series of platinum stibine complexes that are derived by formal stepwise coordination of two fluoride anions at the antimony center rather than the platinum center. The ability of the platinum-bound antimony center to engage in coordination non-innocent behavior facilitates these transformations. Successive coordination of fluoride ligands at antimony results in a weakening of the Sb-Pt bond, as indicated by the lengthening of the Sb-Pt separation in the solid state. QTAIM analysis on the DFT-derived wavefunctions of the series corroborates the weakening of the Sb-Pt interaction. Both QTAIM and NBO analyses show that the Sb-Pt bond also becomes more polarized towards the platinum center upon successive fluoride coordination at the antimony center.

3.6 Experimental section

General Considerations. *Antimony compounds should be handled cautiously.* **25-**Cl was prepared according to the previously reported procedure.[80] Solvents were dried by passing through an alumina column. CyNC, $AgSbF_6$, and TlF were purchased from Strem and used as received. Ambient temperature NMR spectra were recorded using a Varian Unity Inova 400 FT NMR (399.59 MHz for ^{1}H, 100.45 MHz for ^{13}C, 375.89 MHz for ^{19}F, 161.74 MHz for ^{31}P, 85.43 MHz for ^{195}Pt) spectrometer. Chemical shifts (δ) are given in ppm and are referenced against residual solvent signals (^{1}H, ^{13}C) or external BF_3-Et_2O (^{19}F), H_3PO_4 (^{31}P), and K_2PtCl_4 (sat. D_2O soln., ^{195}Pt). IR spectra were recorded on a Mattson ATI Genesis FT-IR spectrometer using KBr pellets. Elemental analyses were performed at Atlantic Microlab (Norcross, GA).

Synthesis of [26][SbF_6]$_2$. CyNC (8 μL, 0.07 mmol) was added to a stirred solution of **25**-Cl (76 mg, 0.07 mmol) in 5 mL of CH_2Cl_2, causing an immediate change in the color of the solution from yellow to pale yellow. After stirring for 15 min., solid $AgSbF_6$ (45 mg, 0.14 mmol) was added, causing an immediate precipitation of AgCl. The reaction mixture was stirred in the absence of light for 12 h., at which time it was filtered over a plug of celite. All volatiles were removed from the filtrate to give a tacky, pale yellow solid, which was triturated with Et_2O (3 x 5mL) to afford a free-flowing yellow powder. The product was dried *in vacuo* to yield 100 mg (92%) of [**26**][SbF_6]$_2$. ^{1}H (339.59 MHz; $CDCl_3$): δ = 0.83-1.02 (br, 3H, Cy-C*H*), 1.25-1.46 (br, 5H, Cy-C*H*), 1.69-1.82 (br, 2H, Cy-C*H*), 4.38-4.51 (br, 1H, Cy-C*H*), 6.79-6.91 (br., 12H, *ortho* Ph-*H*), 7.14 (pseudo-t, 12H, *meta* Ph-*H*), 7.32 (t, 6H, *para* Ph-*H*, $^3J_{H\text{-}H}$ = 7.50 Hz), 7.36-7.41 (br s, 3H, *o*-P(Sb)C_6H_4), 7.64 (pseudo-t, 3H, *o*-P(Sb)C_6H_4), 8.01 (pseudo-t, 3H, *o*-P(Sb)C_6H_4), 9.02 (d, 3H, *o*-P(Sb)C_6H_4, $^3J_{H\text{-}H}$ = 7.50 Hz). ^{13}C{^{1}H} NMR (100.45 MHz, $CDCl_3$): δ = 22.77 (s, Cy-*C*H_2), 24.58 (s, Cy-*C*H_2), 32.06 (s, Cy-*C*H_2), 56.70 (s, Cy-*C*H), 129.65 (s), 130.59-131.38 (m), 131.59 (s), 132.12-132.83 (m) 133.35 (s), 134.63-135.43 (m), 135.55 (s), 136.37 (t, *J* = 9.03 Hz), 136.37 (br m), 139.42-136.37 (br m) The isonitrile carbon resonance was not observed. ^{19}F NMR (375.89 MHz, $CDCl_3$): Only broad, poorly resolved peaks from -110 to -140 ppm were observed for the SbF_6 anions. ^{31}P{^{1}H} NMR (161.74 MHz; $CDCl_3$): δ = 28.86 (s, $^1J_{Pt\text{-}P}$ = 2330 Hz). ^{195}Pt{^{1}H} NMR (83.31 MHz, $CDCl_3$): -5381 (br q, $^1J_{Pt\text{-}P}$ = 2330 Hz). Elemental analysis calculated (%) for $C_{61}H_{53}NF_{12}P_3PtSb_3$: C 43.58, H 3.18; N 0.83; found C 43.58; H 3.15, N 0.89.

Synthesis of [27][SbF$_6$]. A solution of [**26**][SbF$_6$]$_2$ (134 mg, 0.08 mmol) in 6 mL of CH_2Cl_2 was layered with a solution of KF (46 mg, 0.79 mmol) in 2mL H_2O. The biphasic reaction mixture was agitated for 30 minutes, after which the aqueous phase was carefully decanted. The organic phase was dried over Na_2SO_4, filtered, and dried *in vacuo*. The resulting tacky yellow solid was recrystallized from CH_2Cl_2/Et_2O to give [**27**][SbF$_6$] as a pale yellow powder (97 mg, 83%). ^{1}H (339.59 MHz; $CDCl_3$): δ = 0.83-1.08 (m, 2H, Cy-C*H*), 1.08-1.20 (m, 5H, Cy-C*H*), 1.26-1.47 (m, 3H, Cy-C*H*), 3.47-3.59 (br, 1H, Cy-C*H*), 6.92-7.04 (m, 12H, *ortho* Ph-*H*), 7.15 (pseudo-t, 12H, *meta* Ph-*H*), 7.21 (br d, 3H, *o*-P(Sb)C_6H_4, $^3J_{H\text{-}H}$ = 7.71 Hz), 7.26-7.32 (m, 9H, *para* Ph-*H* + *o*-P(Sb)C_6H_4), 7.46 (pseudo-t, 3H, *o*-P(Sb)C_6H_4), 8.67 (d, 3H, *o*-P(Sb)C_6H_4, $^3J_{H\text{-}H}$ = 8.23 Hz). ^{13}C{^{1}H} NMR (100.45 MHz, $CDCl_3$): δ = 22.45 (s, Cy-*C*H$_2$), 24.58 (s, Cy-*C*H$_2$), 31.59 (s, Cy-*C*H$_2$), 55.24 (s, Cy-*C*H), 128.70 (br q, *J* = 3.81 Hz), 130.77 (s), 131.19 (br s), 131.28 (s), 131.54 (s), 132.53 (br q, *J* = 3.81 Hz), 132.99-133.78 (br m), 135.44-136.10 (br m), 137.34 (br m), 148.41-150.41 (br m) The isonitrile carbon resonance was not observed. ^{19}F NMR (375.89 MHz, $CDCl_3$): δ = 128.59 (m), only broad, poorly resolved peaks from -110 to -140 ppm were observed for the SbF_6 anion ^{31}P{^{1}H} NMR (161.74 MHz; $CDCl_3$): δ = 39.67 (d, $^3J_{P\text{-}F}$ = 12.82 Hz, $^1J_{Pt\text{-}P}$ = 2964 Hz). ^{195}Pt{^{1}H} NMR (83.31 MHz, $CDCl_3$): δ = -5143 (q, $^1J_{Pt\text{-}P}$ = 2964 Hz). Elemental analysis calculated (%) for $C_{61}H_{53}NF_7P_3PtSb_2$: C 50.02, H 3.65; N 0.96; found C 49.73, H 3.66, N 0.98.

Synthesis of 28. CyNC (12 μL, 0.10 mmol) was added to a stirred solution of **25**-Cl (111 mg, 0.09 mmol) in 5 mL CH_2Cl_2, causing an immediate change in the color of the solution from yellow to pale yellow. After stirring for 15 min., solid TlF (46 mg, 0.21

mmol) was added, and the reaction mixture was stirred vigorously for 16 h. The resulting pale yellow suspension was filtered over a plug of celite, and all volatiles were removed from the filtrate to give a tacky, pale yellow residue. The residue was washed with 3 x 3 mL THF and subsequently dried *in vacuo* to afford 60 mg (51%) of **28** as a colorless powder. ^{1}H NMR (399.59 MHz, $CDCl_3$): δ = 1.05-1.24 (br, 5H, Cy-C*H*), 1.28-1.41 (br, 3H, Cy-C*H*), 1.42-1.54 (br, 2H, Cy-C*H*), 3.42-3.52 (br, 1H, Cy-C*H*), 6.73-6.82 (m, 8H, *ortho* Ph-*H*), 6.92 (pseudo-t, 8H, *meta* Ph-*H*), 6.96-7.01 (m ,4H, *ortho* Ph-*H*), 7.01-7.08 (m, 4H, *o*-P(Sb)C_6H_4), 7.09-7.20 (m, 12H, *meta* Ph-*H* + *para* Ph-*H* + *o*-P(Sb)C_6H_4), 7.32 (pseudo-t, 2H, *o*-P(Sb)C_6H_4), 7.52 (pseudo-t, 1H, *o*-P(Sb)C_6H_4, 8.62 (d, 2H, *o*-P(Sb)C_6H_4), $^{3}J_{H\text{-}H}$ = 7.69 Hz), 9.13 (d, 1H, *o*-P(Sb)C_6H_4, 6.77 Hz). ^{13}C{^{1}H} NMR (100.45 MHz; CD_2Cl_2): δ = 22.91 (s, Cy-*C*H_2), 24.89 (s, Cy-*C*H_2), 32.01 (s, Cy-*C*H_2), 55.00 (s, Cy-*C*H_2), 127.02 (br), 127.82 (br m), 128.23 (d, *J* = 9.14 Hz), 128.41-129.46 (br m), 129.64-130.74 (br m), 131.00 (br), 131.98 (br m), 132.52-133.40 (br m), 133.60 (br m), 133.86-134.60 (br m), 134.97-135.91 (br m), 137.82 (t, *J* = 23.70 Hz), 138.67 (dm, *J* = 32.85 Hz) The isonitrile carbon resonance was not observed. ^{19}F NMR (375.89 MHz, CD_2Cl_2): δ = -20.73 (br d, 1F, $^{2}J_{F\text{-}F}$ = 67.39 Hz, $^{2}J_{Pt\text{-}F}$ = approx. 66 Hz), -135.97 (dm, 1F, $^{2}J_{F\text{-}F}$ = 67.39 Hz). ^{31}P{^{1}H} NMR (161.74 MHz; CD_2Cl_2): δ = 27.44 (tm, 1P, $^{2}J_{P\text{-}P}$ = 132.61 Hz, $^{1}J_{Pt\text{-}P}$ = 3351Hz), 47.40 (dm, 2P, $^{2}J_{P\text{-}P}$ = 132.61, $^{1}J_{Pt\text{-}P}$ = 2888 Hz) ^{195}Pt{^{1}H} NMR (83.31 MHz, CD_2Cl_2): δ = -5136 (td, $^{1}J_{Pt\text{-}P}$ = 3351, $^{1}J_{Pt\text{-}P}$ = 2888 Hz). Elemental analysis calculated (%) for $C_{61}H_{53}NF_2P_3PtSb{\bullet}C_6H_6$: C 60.69, H 4.49; N 1.06; found C 60.44, H 4.63, N 1.08.

Computational Details. Density functional theory (DFT) calculations (full geometry optimizations) were carried out on **25**-Cl, **25**-F, [**26**]$^{2+}$, [**27**]$^{+}$, and **28** starting from their respective crystal structure geometries with the Gaussian09[133] program (MPW1PW91[95] functional, with 6-31G for H, C, 6-31+G(d') for N, F, 6-311++G** for P, aug-ccpVTZ for Sb,[96] Pt,[134] and Stuttgart relativistic small core ECPs for Sb,[97] Pt[134]). Frequency calculations were also carried out at the optimized geometries. While no imaginary frequencies were found for compounds **25**-Cl, [**27**]$^{+}$ and **28**, a single low energy imaginary frequency corresponding to phenyl ring motion persisted for **25**-F, and two low energy imaginary frequencies corresponding to the cyclohexyl group persisted for [**26**]$^{2+}$. Wavefunctions derived from the optimized structures were utilized for QTAIM analysis using the AIMAll[135] program. The optimized structures were also subjected to natural bond orbital (NBO)[98] analysis, and the resulting natural localized molecular orbitals (NLMOs) were plotted using the Jimp 2[99] program.

Crystallography. Single crystals of [**27**][SbF_6] suitable for X-ray diffraction were obtained by vapor diffusion of Et_2O into a solution of the compound in CH_2Cl_2. Single crystals of [**26**][SbF_6]$_2$ suitable for X-ray diffraction were obtained by slow diffusion of pentane into a $CHCl_3$ solution of the compound at room temperature. Single crystals of **28** suitable for X-ray diffraction were obtained by allowing a C_6H_6 solution of the compound to stand at room temperature overnight. Crystal data, details of data collection, and structure refinement parameters for compounds [**26**][SbF_6]$_2$, [**27**][SbF_6] and **28** are compiled in Table 13. The crystallographic measurements were performed at 110(2) K using a Bruker APEX-II CCD area detector diffractometer, with a graphite-

monochromated Mo-Kα radiation (λ = 0.71069 Å). In each case, a specimen of suitable size and quality was selected and mounted onto a nylon loop. The semi-empirical method SADABS[100] was applied for absorption correction. The structure was solved by direct methods and refined by the full-matrix least-square technique against F^2 with the anisotropic temperature parameters for all non-hydrogen atoms. All H atoms were geometrically placed and refined in riding model approximation. Data reduction and further calculations were performed using the Bruker SAINT+[101] and SHELXTL NT[102] program packages.

Table 13. Crystal data, data collections, and structure refinements for [**26**][SbF_6]$_2$, [**27**][SbF_6] and **28**.

	[**26**][SbF_6]$_2$	[**27**][SbF_6]	**28**
Formula	$C_{61}H_{53}F_{12}NP_3PtSb_3$ •2($CHCl_3$)	$C_{61}H_{53}F_7NP_3PtSb_2$	$C_{61}H_{53}F_2NP_3PtSb$ •(C_6H_6)
Formula Weight	1920.03	1464.54	1325.90
Crystal Size (mm)	0.33 x 0.21 x 0.17	0.24 x 0.11 0.05	0.20 x 0.17 x 0.05
Crystal System	Triclinic	Orthorhombic	Triclinic
Space Group	P-1	Pbca	P-1
a (Å)	11.2596(15)	17.2649(18)	11.0035(15)
b (Å)	15.673(2)	16.7361(18)	13.2048(18)
c (Å)	20.636(3)	36.860(4)	20.396(3)
α (°)	82.937(2)	90	100.137(2)
β (°)	83.932(2)	90	94.541(2)
γ (°)	70.025(1)	90	106.0490(10)
V (Å^3)	3388.7(8)	10650(2)	2777.8(7)
Z	2	8	2
ρ_{calc} (g/cm^3)	1.881	1.827	1.585
μ (mm^{-1})	3.621	3.785	3.138
F(000)	1846	5712	1320
T (K)	110(2)	110(2)	110(2)
Scan mode	ω, φ	ω, φ	ω, φ
hkl Range	-14 → 14	0 → 22	-14 → 14
	-20 → 20	0 → 21	-17 → 16
	0 → 26	-47 → 0	0 → 26
Reflns. collected	38449	31045	38449
Unique reflns. [Rint]	15563 [0.1047]	12232 [0.0293]	12757 [0.1026]
Reflns. used for refinement	15563	12232	12757
Refined parameters	808	676	676
GooF	1.010	1.063	1.024
R1[a], *w*R2[b] (all data)	0.0766, 0.1963	0.0449, 0.0599	0.0720, 0.1758
ρ_{fin} (max., min.) (eA^{-3})	3.9823, -3.0259	3.060, -1.108	2.208, -2.103

[a]R1 = $\sum||F_o| - |F_c||/\sum|F_o|$. [b] *w*R2 ($[w(F_o^2 - F_c^2)^2]/[\sum w(F_o^2)^2]$)$^{1/2}$; $w = 1/[\sigma^2(F_o^2) + (ap)^2 + bp]$; $p = (F_o^2 + 2F_c^2)/3$ with a = 0.1164 for [**26**][SbF_6]$_2$, 0.0131 for [**27**][SbF_6], and 0.1080 for **28**; and b = 0.0000 for [**26**][SbF_6]$_2$, 39.6233 for [**27**][SbF_6], and 0.0000 for **28**.

4. PREPARATION AND CHARACTERIZATION OF GOLD (I) COMPLEXES FEATURING AN AMBIPHILIC PHOSPHINE-CHLOROSTIBINE LIGAND

4.1 Introduction

Ambiphilic compounds are molecules that feature both Lewis acidic and Lewis basic functionalities, connected via an alkyl, aryl, or heteroatom linker (Figure 46).[21, 22, 120] The Lewis basic functionalities utilized typically feature N, P, and S donors, whereas the Lewis acidic functionalities are typically drawn from Groups 13 and 14,[136-139] with Group 15-[31, 32, 37, 40, 55] and 16-based[71, 140] acceptor groups being only recently reported. Interest in ambiphilic compounds, in particular those featuring phosphine-borane combinations, has grown in recent years, owing to their use as frustrated Lewis pairs (FLPs) for small molecule activation,[141-143] as well as their use in transition metal catalysis.[26]

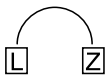

Figure 46. General structure of an ambiphilic compound, featuring a Lewis basic functionality (L) and a Lewis acidic functionality (Z) connected by a linker.

Ambiphilic compounds exhibit rich coordination chemistry, with a variety of coordination modes having been documented (Figure 47).[26] Coordination mode A occurs when the Lewis acid is pendant, and does not engage the metal center. Coordination mode B occurs when both the donor and acceptor functionalities of the ligand engage the metal center. Coordination mode C involves the interaction of a metal-bound ligand, usually a halide, to the acceptor moiety. Finally, coordination mode D occurs when a Lewis base

separate coordinates to the acceptor functionality, while the donor functionality coordinates to the metal center. This scenario includes cases in which a metal-halide bond is activated, resulting in transfer to the Lewis acidic functionality.

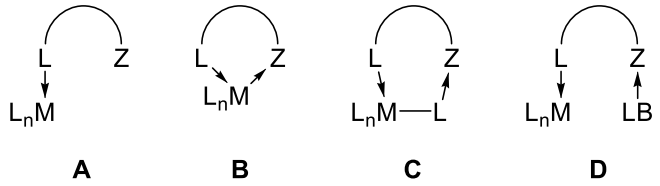

Figure 47. Observed coordination modes of ambiphilic ligands

Having previously shown that Sb(V) Z-ligands may engage late transition metal centers *via* coordination mode B, we sought to determine other coordination modes may be observed with antimony-containing ambiphilic ligands. Inspired by work from the Reid group in which coordinated halostibines of the form Me_nSbX_{3-n} were shown to act as Lewis acids towards neutral donors, as well as Lewis bases towards metal centers,[30, 42] we became interested in ambiphilic ligands featuring Sb(III) centers as their Lewis acid functionalities. In our initial efforts, we demonstrated that halostibines incorporated into a pincer-type ambiphilic ligand framework may act as pure σ-acceptors towards late transition metals.[37] With these results in mind, we decided to investigate the coordination chemistry of a bidentate ligand bearing dihaloarylstibine functionality in order to determine whether different coordination modes could be observed upon changing the number of donor buttresses.

4.2 Synthesis and characterization of a phosphine-dichloroarylstibine ligand

The phosphinylstibine ligand (*o*-(PPh_2)C_6H_4)$SbCl_2$ (**29** -Cl**)** was prepared by a redistribution reaction between ((*o*-(PPh_2)C_6H_4)$_3$Sb (**7**) and two equivalents of $SbCl_3$ (Figure 48). The $^{31}P\{^1H\}$ NMR spectrum of **29**-Cl consists of a singlet at -19.72 ppm. Due to reaction inhomogeneity, samples of **29**-Cl are often contaminated by small quantities of (*o*-(PPh_2)C_6H_4)$_2$SbCl (**6**-Cl) (up to 5% by $^{31}P\{^1H\}$ NMR, δ = -11.16 ppm). While these crude reaction mixtures were used without further purification, analytically pure samples of **29**-Cl could be obtained by fractional recrystallization from toluene/diethyl ether.

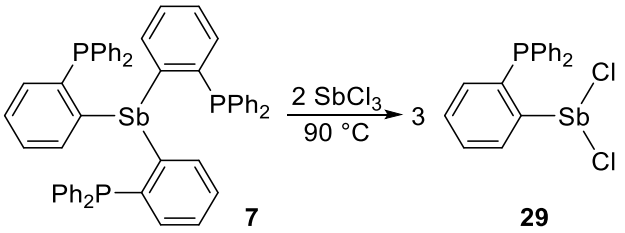

Figure 48. Synthesis of **29**-Cl by redistribution reaction of **7** with $SbCl_3$.

The solid state structure of **29**-Cl (Figure 49) exhibits a Sb-P separation of 3.03 Å, with the phosphine moiety oriented opposite an Sb-Cl bond. This orientation, along with the contracted Sb-C-C and P-C-C angles of 114.4(2) ° and 113.7(2) ° along the *ortho*-phenylene backbone suggest significant donation from the phosphine group into an Sb-Cl σ* orbital. Additionally, the stibine moiety of **29**-Cl engages a neighboring stibine in two Sb-Cl short contacts of 3.26 Å, further demonstrating the Lewis acidity of the dichloroarylstibine functionality. Similar short contacts are observed in the solid state

structures of the related $RSbCl_2$ species $PhSbCl_2$ (Sb-Cl' = 3.443(2) Å)[144] and *p*-tolyl$SbCl_2$ (Sb-Cl' = 3.433(2) Å)[145].

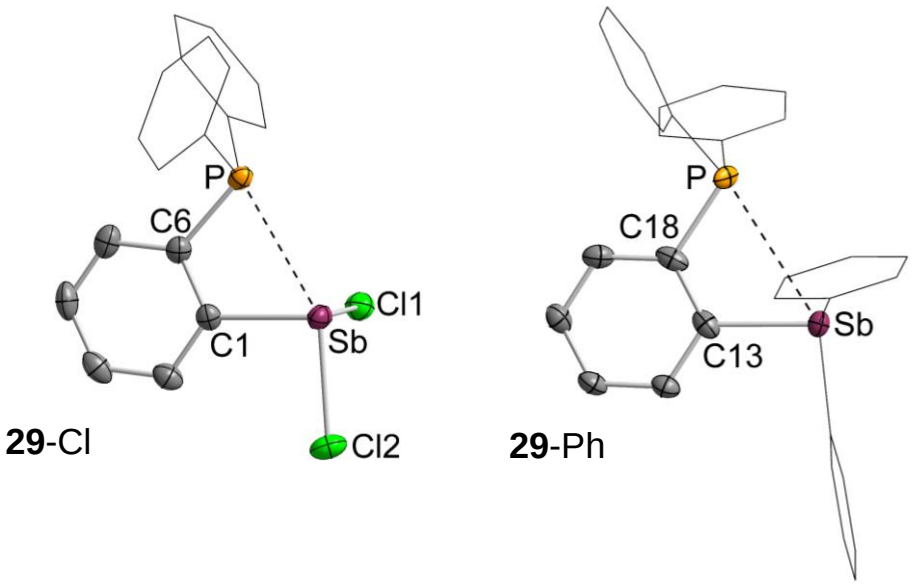

Figure 49. Solid state structures of **29**-Cl (left) and **29**-Ph (right). Ellipsoids are drawn at the 50% probability level. Hydrogen atoms are omitted, and selected phenyl groups are drawn in wireframe for clarity. Selected bond lengths (Å) and angles (°) for **29**-Cl: Sb-Cl1 2.3999(14), Sb-Cl2 2.4568(13), Sb-P 3.03, C6-C1-Sb 113.7(2), C1-C6-P 114.4(2). **29**-Ph: Sb-P 3.28, C18-C13-Sb 117.1(2), C13-C18-P 119.3(3).

In order to judge the effect of halogen substitution at antimony center on the ligand characteristics and coordination behavior, the corresponding triarylstibine derivative (*o*-$(PPh_2)C_6H_4)SbPh_2$[146] (**29**-Ph),was also structurally characterized (Figure 49). The Sb-P separation of 3.28 Å in **29**-Ph is considerably longer than that found in **29**-Cl (3.03 Å). The longer Sb-P separation, combined with the respective Sb-C-C and P-C-C angles of 117.1(2) and 119.3(3) along the *ortho*-phenylene backbone, suggest that the

intramolecular interactions between the phosphine and stibine moieties are predictably weaker than in the case of **29**-Cl.

In order to gain further insight into the relative strengths of the Sb-P interactions present in these two ligands, both compounds were subjected to optimization using DFT methods, followed by NBO analysis. The NBO analyses found combined l.p.(P)→σ*(Sb-C/Sb-Cl) second order perturbation energies of 7.0 and 20.7 kcal/mol for **29-**Ph and **29**-Cl, respectively.

4.3 Coordination chemistry

With the ligands **29**-Cl and **29**-Ph in hand, we next sought to investigate and compare their respective coordination behavior. To this end, **29**-Ph was allowed to react with (tht)AuCl (tht = tetrahydrothiophene) in a 1:1 ratio, affording compound (**30**) as a colorless solid (Figure 50). The $^{31}P\{^{1}H\}$ NMR spectrum of **30** consists of a singlet at 32.27 ppm.

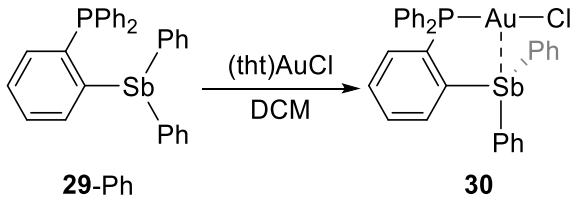

Figure 50. Synthesis of compound **30**.

The solid state structure of **30** contains two crystallographically independent molecules, differing in the orientation of the stibine, in the asymmetric unit. The ligand coordinates the gold center in an asymmetric fashion, with Au-P distances of 2.231(2) Å and 2.239(2)

Å and Au-Sb distances of 3.0527(8) Å and 3.0494(7) Å. While the Au-P distances are similar to that observed in Ph_3PAuCl (2.235(3) Å),[147] the Au-Sb distances are considerably longer than those observed in the three-coordinate $[Au(Sb\ Mes\ Ph_2)_3][ClO_4]$ (2.6250(4) Å)[87] and the four-coordinate $[Au(SbPh_3)_4][ClO_4]$ (2.658(2)-2.656(2) Å),[148] despite the Au-P-C-C torsion angles of -7.6(9)° and 13.0(9)° indicating that the gold center errs only slightly from the *o*-phenylene plane of the ligand. The antimony center adopts a disphenoid geometry, as indicated by the Au-Sb-C_{trans} angles of 171.4(2)° and 169.9(2)°, and C_{cis}-Sb-C_{cis} angles of 95.5(3)° and 96.4(3)°. Similar geometries have been observed at the antimony centers in the related tris- and bis-phosphinylstibine gold complexes.[37, 55, 149] The strong pyramidalization at the antimony centers, taken together with the relatively long Au-Sb separations suggest that the stibine moiety is only weakly engaged with the gold center as a Lewis base.[1] The gold center adopts a T-shaped geometry, with the P-Au-Cl angles of 168.84(8)° and 168.53(8)° indicating only a slight bend towards the stibine moiety.

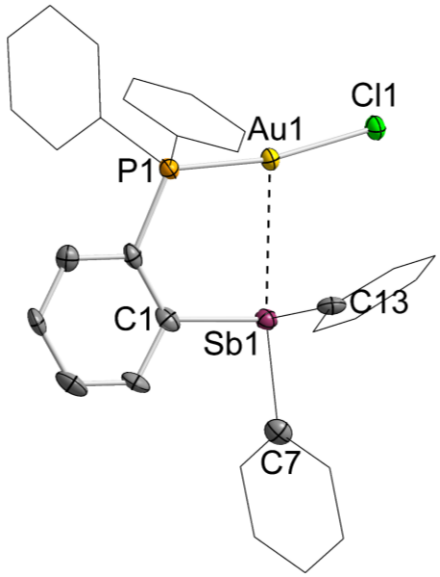

Figure 51 Structure of compound **30**, showing one of two crystallographically independent molecules within the unit cell. Thermal ellipsoids are drawn at the 50% probability level. Selected phenyl rings are drawn in wireframe, and hydrogens are omitted for clarity. Selected bond lengths (Å) and angles (°); the analogous metrics corresponding the second crystallographically independent molecule are given in brackets: Au1-Sb1 3.0527(8) [3.0494(7)], Au1-P1 2.231(2) [2.239(2)], P1-Au1-Cl1 168.84(8) [168.53(8)], C1-Sb1-C7 97.5(3) [99.3(3)], C1-Sb1-C13 95.5(3) [96.4(3)], C7-Sb1-C13 96.5(3) [95.6(3)], Au1-Sb1-C7 171.4(2) [169.9(2)].

Having characterized compound **30**, we next sought to prepare the corresponding gold complex of **29**-Cl. Reacting **29**-Cl with (tht)AuCl in a 1:1 ratio, however produced a reaction mixture whose $^{31}P\{^{1}H\}$ NMR spectrum in CH_2Cl_2 contained two distinct resonances (**31** and **32**, Figure 52). Intrigued by the presence of these two species, we next sought to individually isolate them.

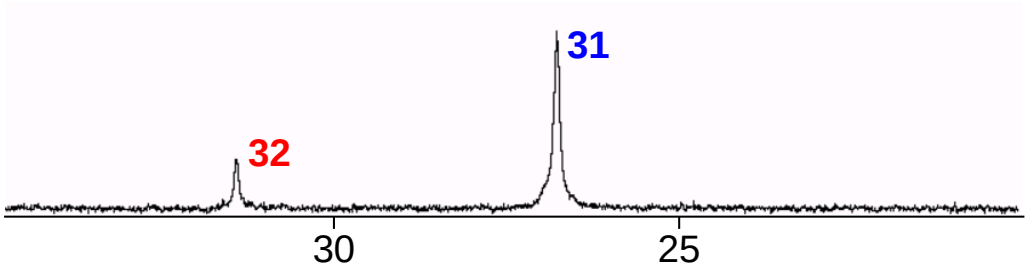

Figure 52. $^{31}P\{^{1}H\}$ NMR spectrum of the 1:1 reaction mixture of **29**-Cl and (tht)AuCl in CH_2Cl_2.

Repeating the reaction of **29**-Cl with (tht)AuCl at -78°C afforded **31** as the sole product (Figure 53). A single crystal X-ray diffraction study revealed **31** to be analogous to compound **30**, with one molecule of **29**-Cl coordinating to a AuCl fragment (Figure 54). Similar to the structure of **30**, the ligand coordinates the gold center in an asymmetric fashion, with an Au-P distance of 2.239(1) Å and an Au-Sb distance of 2.9817(5) Å. As in **30** the antimony center adopts a disphenoid geometry, with ∡Au-Sb-Cl_{trans} = 175.63(5)° and ∡C-Sb-Cl_{cis} = 94.9(2)°. The P-Au-Cl angle of 169.91(5)° deviates only slightly from linearity. Taken together, these geometric parameters suggest that, as in **30**, the stibine moiety is not strongly engaged with the gold center.

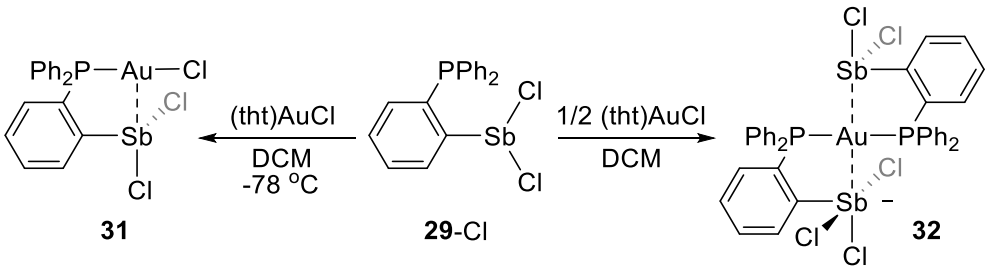

Figure 53. Synthesis of compounds **31** and **32**.

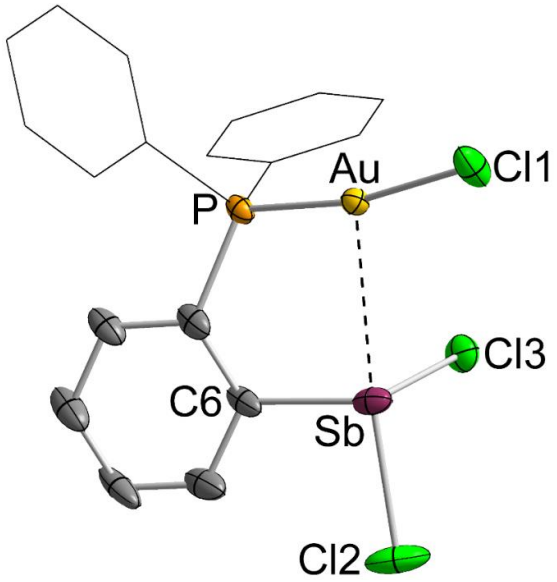

Figure 54. Crystal structure of **31**. Ellipsoids are drawn at the 50% probability level. Hydrogen atoms are omitted, and selected phenyl groups are drawn in wireframe for clarity. Selected bond lengths (Å) and angles (°) Au-Sb 2.9817(5), Au-P 2.239(1), P-Au-Cl1 169.91(5), C6-Sb-Cl2 93.5(2), C6-Sb-Cl3 94.9(2), Cl2-Sb-Cl3 94.86(5), Au-Sb-Cl2 175.63(5).

Although compounds **30** and **31** feature a high degree of structural similarity, inspection of their extended structures in the solid state highlights the differences in the ligand behavior of their antimony centers (Figure 55). In the case of 30, each crystallographically independent molecule forms a head-to-tail short contact dimer with a neighboring unit in

the solid state. The intermolecular Au-Sb distances of 3.46 Å and 3.43 Å are significantly longer than the intramolecular interactions, with the gold centers being oriented approximately *trans* to a neighboring Sb-C bond. In contrast to **30**, compound **31** forms a short contact dimer through two intermolecular Sb-Cl contacts of 3.11 Å, which is longer than the Sb-Cl distances observed in $[Me_4N][PhSbCl_3]$ (2.423(3)-2.657(3) Å).[150] The intermolecular Au-Au' distance of 3.67 Å is longer than the 2.50-3.50 Å distances typically associated with aurophilic interactions,[151] suggesting that the Sb-Cl interactions dictate the observed aggregation mode. Taken together, the two distinct modes of aggregation observed in **30** and **31** suggest that, despite their overall structural similarity, the antimony center in **30** acts more akin to a Lewis base whereas the antimony center in **31** acts as a Lewis acid.

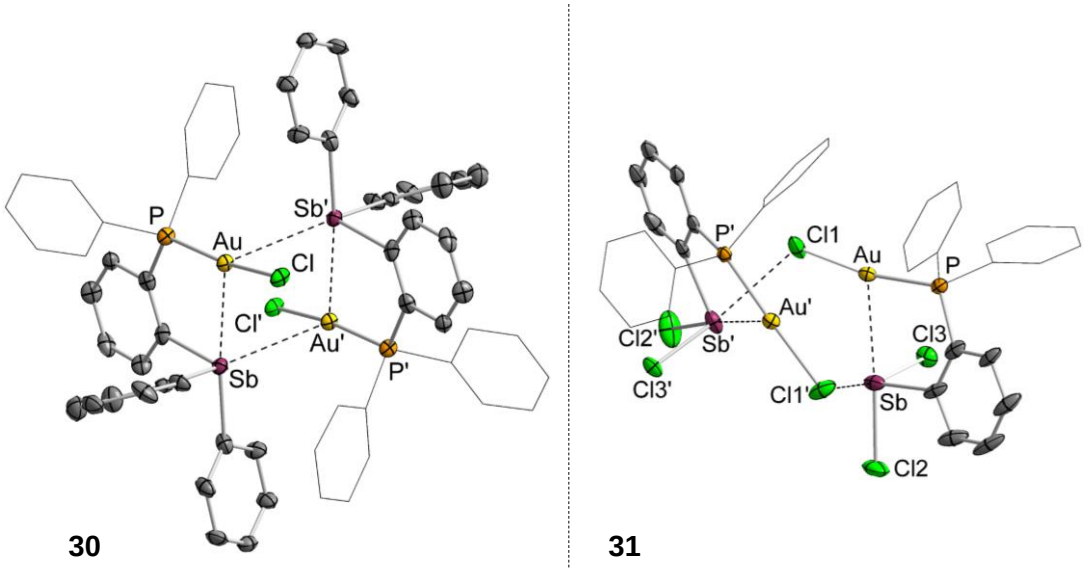

Figure 55. Extended solid state structures of **30** and **31**. Only one crystallographically independent unit is shown for **30**. Thermal ellipsoids are drawn at the 50% probability level. Selected phenyl rings are drawn in wireframe, and hydrogens are omitted for clarity.

Turning our attention to compound **32**, obtained along with **31** in the room temperature reaction of **29**-Cl with (tht)AuCl, a single crystal of the compound obtained from the reaction mixture was subjected to a single crystal X-ray diffraction study. To our surprise, the solid state structure of **32** revealed that two equivalents of ligand **29**-Cl had coordinated to the gold center, activating a Au-Cl bond to form a zwitterionic gold Sb (III) antimonate (Figure 56). By repeating the reaction of **29**-Cl with (tht)AuCl in a 2:1 ratio, **32** could be obtained as the sole product. The Au-Cl bond activation observed in the solid state structure of **32** stands in contrast to typical $ClAu(PR_3)_2$ species such as $ClAu(PPh_3)_2$, in which the chloride ligand remains bound to gold in the solid state.[152] Similar activations of Au-Cl bonds have been observed in gold complexes of ambiphilic phosphinoalane and phosphinogallane ligands.[153-155] Reconciliation of the solid state structure of **32** with the

singlet resonance observed in its $^{31}P\{^{1}H\}$ NMR spectrum suggests that the chloride abstracted from the gold center is rapidly exchanged between the two flanking antimony centers, or is dissociated in solution.

As in compounds **30** and **31**, the two phosphinostibine ligands coordinate to the gold center in an unbalanced fashion, with Au-P distances of 2.3215(10) Å and 2.3141(10) Å and Au-Sb distances of 3.0350(4) Å and 3.1198(3) Å for the stibine and antimonate moieties, respectively. The antimony center of the antimonate moiety approaches the gold center to attain a distorted square pyramidal geometry, as indicated by a calculated τ value of 0.17. The Au-Sb2-Cl4 angle of 171.22(5) ° indicates that the stibine moiety approaches the gold center to achieve a seesaw geometry. The geometries about the two antimony centers, taken together with the relatively long Au-Sb distances, suggests that, like in compounds **30** and **31**, the antimony ligands are at best only weakly engaged with the gold center as Lewis bases. The P1-Au-P2 angle of 168.76(5) ° slightly deviates from linearity, whereas the Sb1-Au-Sb2 angle of 135.722(15) ° is significantly bent.

Similar to compound **31**, **32** forms a chloride-bridged short contact dimer in the solid state, with one chloride from each antimonate moeity interacting with the gold center and the stibine moiety of a neighboring molecule. The shortest Au-Cl distance of 3.06 Å in this dimeric structure is considerably longer than that found in $(PPh_3)_2AuCl$ (2.526(10) Å),[152] suggesting that any Sb-Cl-Au bridging interactions are minimal. The intramolecular Sb-Cl contacts of 3.13 Å are similar to the intramolecular Sb-Cl distances observed in **31**.

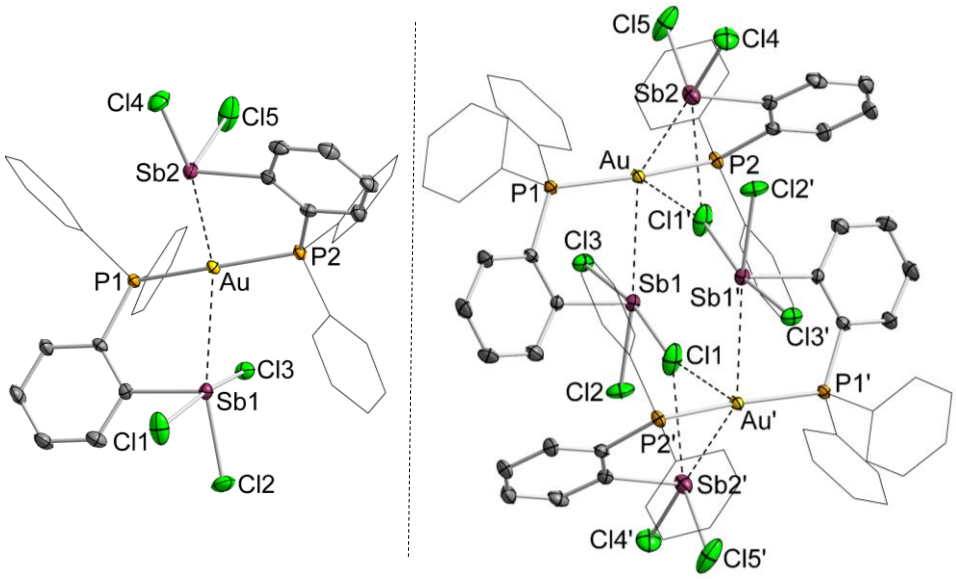

Figure 56. Solid state structure of compound **32**, shown as a monomeric unit (left) and the corresponding short contact dimer structure (right). Thermal ellipsoids are drawn at the 50% probability level. Selected phenyl rings are drawn in wireframe, and hydrogens are omitted for clarity. Selected bond lengths (**Å**) and angles (°): Au-Sb1 3.1198(3), Au-Sb2 3.0350(4), Au-P1 2.3215(10), Au-P2 2.3141(10), Sb1-Cl1 2.6471(11), Sb1-Cl2 2.3843(11), Sb1-Cl3 2.5437(10), Sb2-Cl4 2.3915(11), Sb2-Cl5 2.3886(13), P1-Au-P2 168.96(4), Sb1-Au-Sb2 135.164(9), Au-Sb1-Cl2 158.69(3), Au-Sb2-Cl4 170.88(3), Cl1-Sb1-Cl3 169.87(4).

Intrigued by the ability of the dichloroarylstibine unit of **29**-Cl to abstract a gold-bound chloride in conjunction with an ancillary donor ligand, we next sought to investigate the generality of this reactivity with phosphines by reacting **29**-Cl with (tht)AuCl in the presence of one equivalent of PPh_3, obtaining compound **33** as a yellow solid (Figure 57). Compound **33** is considerably more soluble in organic solvents than compound **32**, facilitating solution phase spectroscopy. The $^{31}P\{^{1}H\}$ NMR spectrum of compound **33** at 23 °C shows two broad resonances centered at 34.02 and 41.49 ppm, which resolve upon

cooling to -40 °C to a pair of strongly coupled doublets ($^2J_{P\text{-}P}$ = 299.00 Hz) at 35.47 and 42.43 ppm.

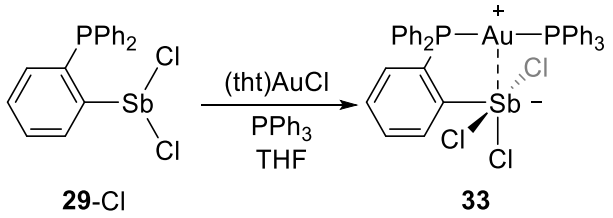

Figure 57. Synthesis of compound **33**.

The solid state structure of compound **33** was determined by a single crystal X-ray diffraction study. Similar to compound **32**, the structure of **33** revealed that the dichloroarylstibine moiety of **29**-Cl had activated a Au-Cl bond, forming a zwitterionic gold antimonate complex (Figure 58). The antimony center in **33** adopts a distorted square pyramidal geometry, as evidenced by a τ value equal to 0.22. The P1-Au-P2 angle of 167.66(5) ° deviates only slightly from linearity towards the antimony center. The Au-Sb distance of 2.9371(9) Å is slightly shorter than that found for the antimonate Au-Sb distance (3.1198(3) Å) in compound **32**, but again considerably longer than those found in the related three coordinate gold stibine complexes.

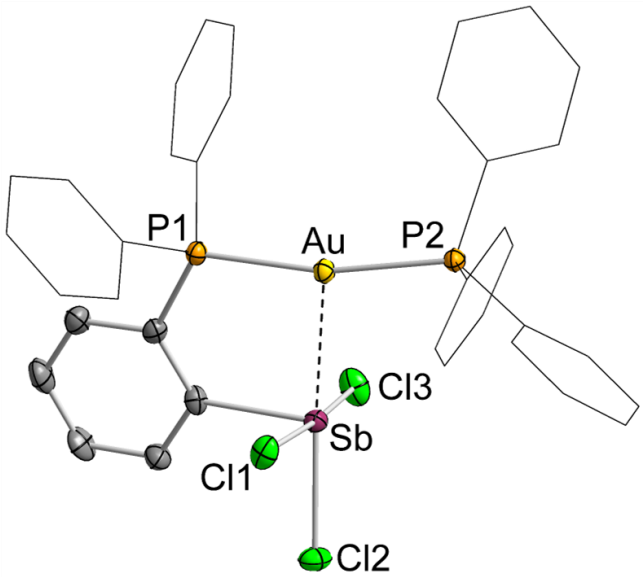

Figure 58. Structure of compound **33**. Thermal ellipsoids are drawn at the 50% probability level. Selected phenyl rings are drawn in wireframe, and hydrogens and solvent molecules are omitted for clarity. Selected bond lengths (**Å**) and angles (°): Au-Sb 2.9371(9), Au-P1 2.3154(16), Au-P2 2.3268(16), Sb-Cl1 2.6068(17), Sb-Cl2 2.3995(16), Sb-Cl3 2.5778(17), P1-Au-P2 167.66(5), Au-Sb-Cl2 161.97(4), Cl1-Sb-Cl3 175.28(5).

4.4 Computational studies on **30**, **31**, and **33**

In an effort to investigate the bonding situations between antimony and gold in **30**, **31**, and **33**, each compound was optimized by DFT methods and subsequently subjected to NBO analysis. Inspection of the NBO donor-acceptor interactions found in **30** and **31** finds both Au→Sb and Sb→Au interactions (Figure 59). Such 'confused' σ-donor/acceptor behavior has been previously observed in the related bisphosphinylstibine gold complexes **4** and **5**.[37] Inspection of the NBO deletion energies corresponding to the Au→Sb and Sb→Au interactions finds that the dichlorarylstibine unit in **31** acts as a weaker σ-donor and better σ-acceptor than the triarylstibine unit in **30**, in line with their expected electronic profiles (Table 14). The similar magnitudes of the Au→Sb and Sb→Au interactions in

each case suggest that the overall interaction between the antimony and gold centers is weak, in line with the geometric parameters which suggest limited engagement of the antimony atom as a ligand. NBO analysis of **33** finds that chloride coordination at the dichloroarystibine unit drastically alters the relative strengths of the Au→Sb and Sb→Au interactions, with the former being weakened and the latter being enhanced. This change can be attributed to the increased coordination number and negative charge on the trichloroarylantimonate unit.

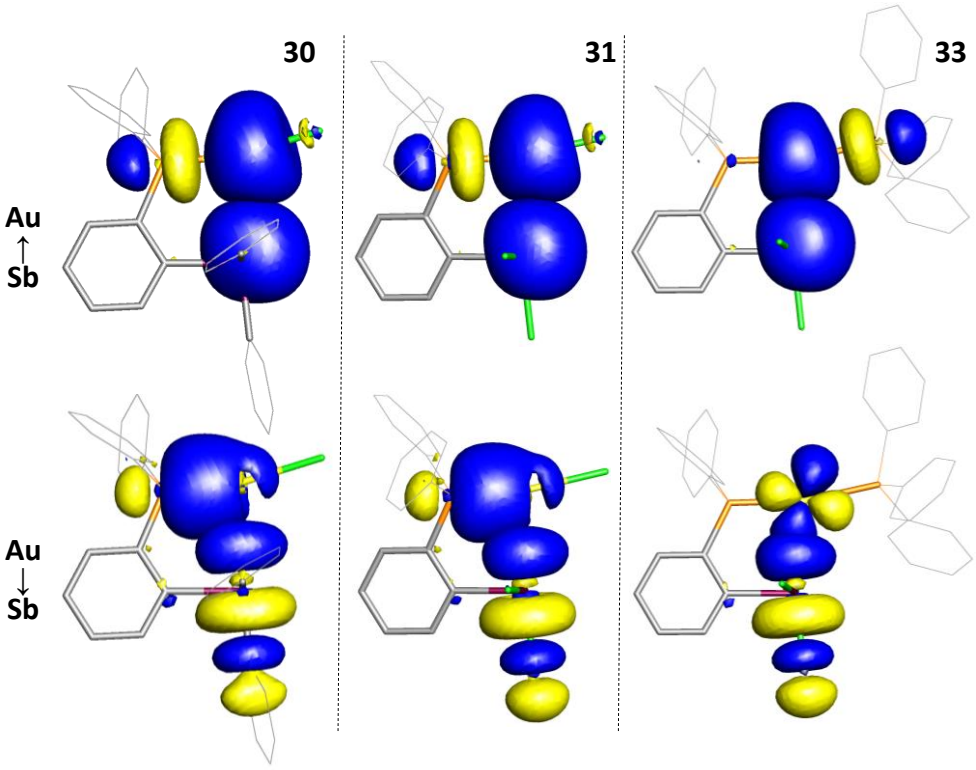

Figure 59. Principal Sb→Au (top) and Au→Sb (bottom) donor-acceptor interactions in **30** (left), **31** (center), and **33** (right) obtained from NBO analysis (isodensity value = 0.05). Hydrogen atoms are omitted, and selected groups are drawn in wireframe for clarity.

Table 14. NBO deletion energies for the Sb→Au and Au→Sb interactions in **30**, **31**, and **33**.

Compound	∑Sb→Au NBO deletion energies (kcal/mol)	∑Au→Sb NBO deletion energies (kcal/mol)
30	31.15	18.99
31	25.77	30.79
33	39.85	9.11

4.5 Two electron oxidation of a pendant antimony center

With compounds **30** and **31** in hand, we next investigated whether the pendant antimony centers present in these species could undergo clean, two electron oxidation. Such a possibility is well-precedented in related gold bis- and trisphosphinylstibine complexes **4**, **5**, and **10**¸which readily sustain oxidation by a variety of reagents, including *o*-chloranil (Figure 60).[37, 55, 80]

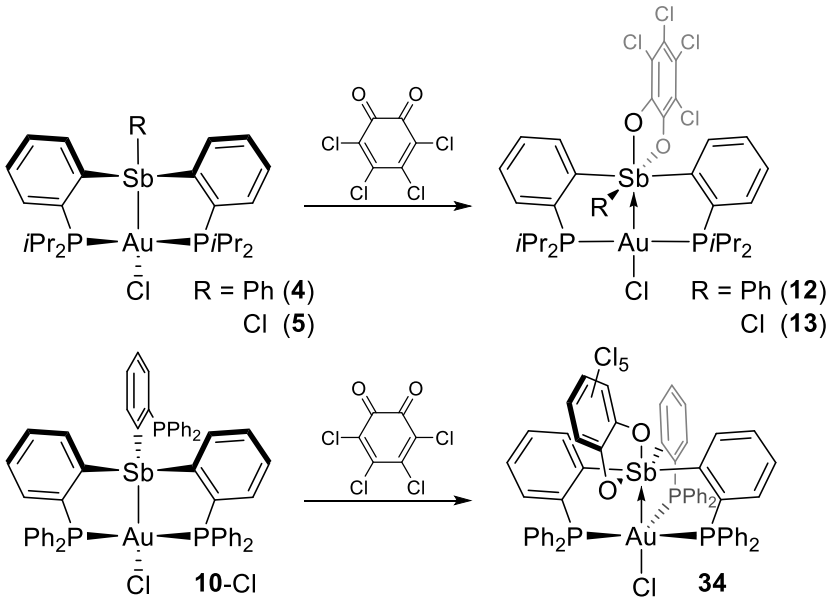

Figure 60. *o*-chloranil oxidations of Au-Sb complexes previously described by Wade[80] and Ke.[37]

While attempted oxidation of **31** by *o*-chloranil led to an intractable mixture of products, oxidation of **30** by *o*-chloranil cleanly afforded compound **35** as an orange solid. The $^{31}P\{^{1}H\}$ spectrum of compound **35** consists of a singlet at 41.49 ppm, which is appreciably downfield-shifted from that of **30** (32.27 ppm).

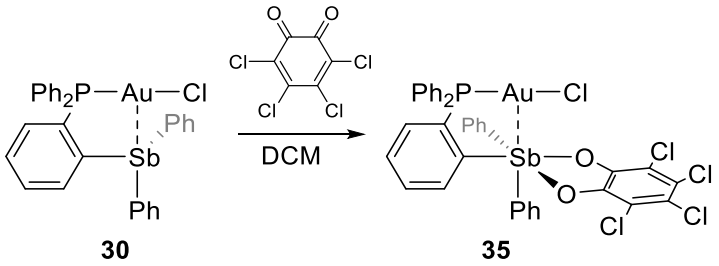

Figure 61. Oxidation of **30** by *o*-chloranil.

The crystal structure of **35** confirmed the oxidation of the antimony center by *o*-chloranil. Unlike **4** and **10**, whose Au-Sb bonds noticeably contract upon oxidation of the antimony center by *o*-chloranil (2.8374(4) Å in **10**-Cl to 2.6767(11) Å in **34**, 2.8669(4) Å in **4** to 2.6833(3) Å in **12**)[37, 80] the Au-Sb distance of 3.2181(3) Å is significantly longer than those found in **30** (3.0527(8), 3.0494(7) Å). Similar to compound **30** (∡P-Au-Cl = 168.84(8)°, 168.53(8)°) the P-Au-Cl angle of 171.93(3)° deviates only slightly from linearity. Whereas the respective τ_{Sb} values for **12** (0.02) and **34** (0.01) suggest that the gold centers in these species occupy an open site above the basal plane of a rigidly square pyramidal antimony center, the τ_{Sb} value of 0.19 in 35 suggests a significant distortion away from square pyramidal geometry. Taken together, these metrics suggest that the antimony center in **35** only weakly interacts with the proximal gold center. The difference in the coordination behavior of the stiborane unit in **35** relative to those found in **12** and **34** underscores the importance of using multiple donor buttresses to secure and enhance the M-Sb interactions in antimony-based ambiphilic ligands.

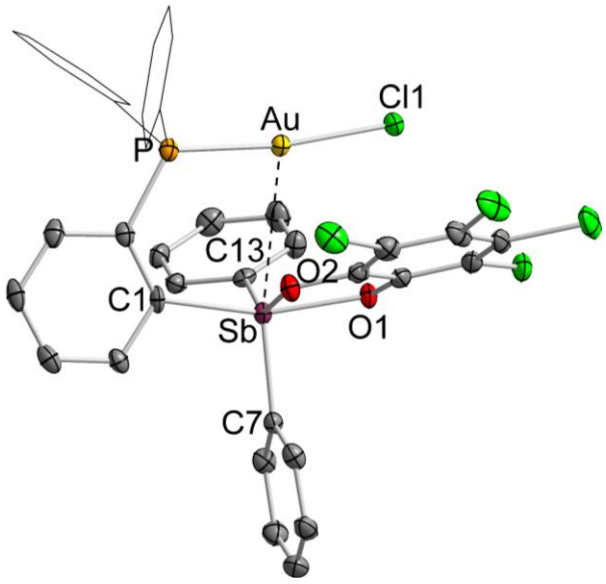

Figure 62. Structure of compound **35**. Thermal ellipsoids are drawn at the 50% probability level. Selected phenyl rings are drawn in wireframe, and hydrogens and solvent molecules are omitted for clarity. Selected bond lengths (Å) and angles (°): Au-Sb 3.2181(3), Au-P 2.2344(9), Sb-O1 2.052(2), Sb-O2 2.040(2), P-Au-Cl 171.93(3), Au-Sb-C7 168.32(9), O1-Sb-C1 158.67(11), O2-Sb-C13 147.32(11).

As a complement to the above structural study, the structure of **35** was subjected to DFT optimization and subsequent NBO analysis (Figure 63). NBO analysis found a series of donor-acceptor interactions involving a gold-based 5d orbital and vacant antimony-based orbitals. In contrast to the parent compound **30**, no Sb-Au interactions involving antimony-based orbitals were observed, in agreement with the oxidized nature of the antimony center in **35**. The deletion energy of the combined Au→Sb interactions sums to 7.71 kcal/mol, which is noticeably diminished compared with the magnitude of the deletion energies associated with the Au→Sb interactions in **30**, **31**, and **33**. The lesser strength of the Au→Sb interaction in **35** despite the oxidation of the antimony center can be attributed to the increased bulk of the stiborane moiety, as well as the greater Au-Sb separation.

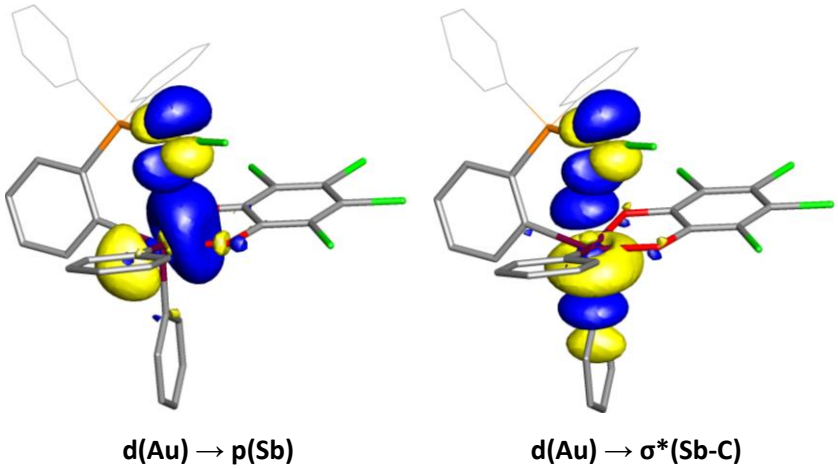

Figure 63. Principal Au→Sb donor-acceptor interactions in **35** obtained from NBO analysis (isodensity value = 0.05). Hydrogen atoms are omitted, and selected groups are drawn in wireframe for clarity.

4.6 Catalytic propargylamide cyclization

Electrophilic gold catalysis has attracted a great deal of interest in recent years, owing to the mild reaction conditions, good atom economy, and high functional group tolerance it affords.[156, 157]Typical gold catalysts are prepared by *in situ* activation of species of the general formula LAuX, where L is a neutral, two electron donor such as a phosphine or a carbene and X is a halide, alkoxide, or alkyl ligand. This activation is most often achieved by silver salt-mediated halide abstraction or protonolysis of a gold alkoxide or alkyl using an acid with a weakly coordinating conjugate base (Figure 64). In both of these cases, catalyst activation is rapid and irreversible. While the resultant active catalysts are highly active, they are often fragile, decomposing to catalytically inactive $[L_2Au]^+$ and metallic gold.[158] Additionally, use of silver salt-mediated anion metathesis method mandates the removal of AgX, which may itself be catalytically active,[159, 160] from the reaction mixture.

Taken together, these and other issues serve to limit the commercial utility of electrophilic gold catalysis.

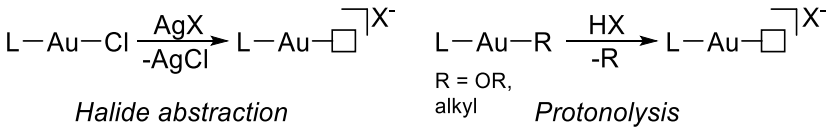

Figure 64. Typical activations of electrophilic gold (I) catalysts.

In an effort to address the stability of gold catalysts, a number of novel strategies have been developed. An area of particular focus towards this end has been the replacement of silver salts with alternative Lewis acids that act as chloride scavengers.[158, 161-164] In addition to avoiding the use of silver salts, the use of alternative Lewis acids may facilitate slow, reversible activation of the gold precatalyst, thus improving the robustness of the system. An example of such a system is provided by Gandon, who demonstrated that addition of a substoichiometric amount of $Cu(OTf)_2$ to Ph_3AuCl promotes the electrophilic cyclization of enynes (Figure 65).[158] Gandon has also extended this strategy to main group Lewis acids, including In (III), Si (IV), and Bi (III) salts.[163]

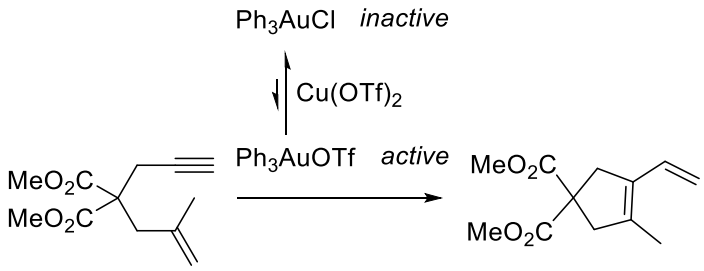

Figure 65. $Ph_3PAuCl/Cu(OTf)_2$-catalyzed enyne cyclization reported by Gandon.

A related strategy involves the design of ligands containing pendant Lewis acid functionalities, which are able to effect intramolecular halide abstraction from the gold center. [153-155] The viability of such a strategy is illustrated by a report from Bourissou and coworkers, in which a zwitterionic aluminate-phosphine gold complex arising from intramolecular chloride abstraction from (tht)AuCl was shown to catalyze the cyclization of propargylic amides (Figure 66).[155] In addition to facilitating halide abstraction, pendant Lewis acids have also been shown to improve the activity of electrophilic catalysts,[29, 38] even in cases when the structurally observed M→LA appears to be weak.[165] Finally, we note that the zwitterionic products of Lewis acid-mediated intramolecular halide abstraction bear comparison to a number of zwitterionic gold complexes featuring an anionic *N*-heterocyclic carbine (NHC) coordinated to a cationic gold center, a number of which have been shown to be active electrophilic catalysts.[166-168]

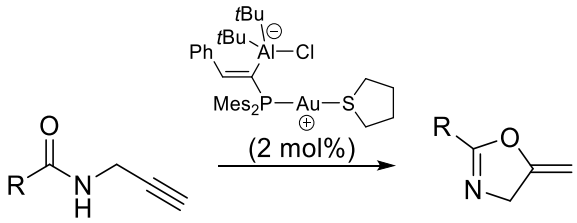

Figure 66. Catalytic cyclization of propargylic amides by a zwitterionic aluminate-phosphine gold complex reported by Bourissou.

Having established the Lewis acidity of the pendant dichloroarylstibine unit in **31**, we next sought to investigate whether this compound could serve as a competent electrophilic catalyst. The ability of **31** to engage a substrate concomitant with chloride transfer to the antimony center is supported by the facile formation of the zwitterionic species **32** and **33**, which can be viewed as resulting from displacement of a gold-bound chloride of **31** by **29**-Cl and PPh_3, respectively. Similar substrate-assisted chloride abstraction has been observed in alkali metal salts of NHC gold chlorides, which react with stoichiometric amounts of PPh_3 to give the corresponding zwitterionic NHC gold phosphine and an alkali chloride.[167] With this idea in mind, we envisioned that the dichloroarylstibine moiety in **31** could facilitate chloride displacement from the gold center by an incoming substrate molecule (Figure 67). The reversible nature of this intramolecular halide abstraction may also serve to improve the robustness of the catalyst.

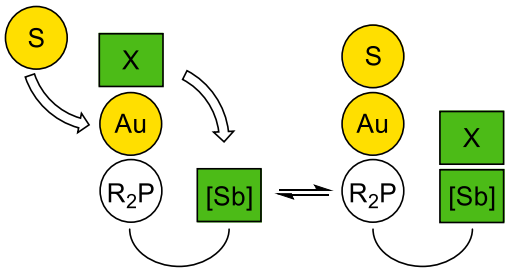

Figure 67. General scheme for the substrate-assisted abstraction of a gold-bound halide by a pendant antimony Lewis acid.

In a first approach to this idea, we investigated catalytic competency of **30**, **31**, and **33** for the cyclization of propargylic amides (Table 15). Propargylic amides were chosen as the substrate due to their modular syntheses, as well as their cyclized oxazole products being featured in a variety of pharmaceutical targets.[169-173] As a model reaction, **30**, **31**, and **33** were utilized as catalysts (2 mol. %) in the cyclization of *N*-(prop-2-yn-1-yl)adamantine-1-carboxamide. In each case, the cyclized product (A) and its isomer (B) are observed. To our surprise, compound **30** showed some activity, with 18% conversion over 33 hours. While triarylstibines have been shown to be mildly acidic,[43] to our knowledge no halide adducts of such species have been reported. Instead of facilitating chloride abstraction from the proximal gold center, the weakly Lewis acidic pendant stibine may serve instead to activate the gold center via inductive effects.[29, 38] An alternative explanation for the activity of **30** could be the presence or formation of small amounts of gold nanoparticles, which in some cases have been shown to be effective catalysts even at extremely low loadings.[174] Compound **31** proved to be considerably more competent than **30** in the cyclization of the substrate, converting 87% over 33 hours. This

enhanced activity is in line with the increased acidity of the dichloroarylstibine moiety relative to the triarylstibine moiety in **30**. Similar to **30** the bis(phosphine) compound **33** shows poor, but non-negligible activity, converting 13% in 29 hours. This activity is notable, in that it provides another example of a typically inactive bis(phosphine) gold center that can perform electrophilic catalysis. [29, 38] Finally, we note that all of the catalysts tested are inferior to a traditional gold catalyst, such as $Ph_3PAuNTf_2$ (NTf_2 = bis(trifluoromethanesulfonyl)imide), which catalyzes the same cyclization with a lower catalyst loading (1 mol%), shorter reaction time (18 h.), and higher yield (95%).[173]

Table 15. Activities of selected gold catalysts in the cyclization of *N*-(prop-2-yn-1-yl)adamantine-1-carboxamide.

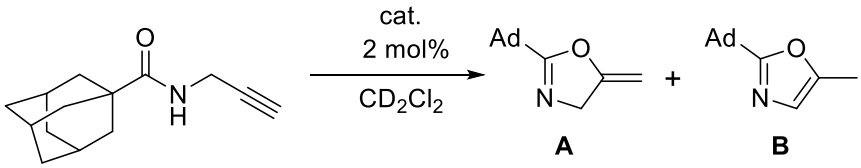

Catalyst	Time (h.)	Conversion (%)
30	33	18 (A) + 0 (B) = 18
31	33	42 (A) + 45 (B) = 87
33	29	4 (A) + 9 (B) = 13

In an effort to further probe the activity of **31**, a second series of cyclization reactions were performed (Table 16). First, we note that under the reaction conditions previously used, Ph_3PAuCl shows no catalytic activity, in line with its unactivated nature. However, when $PhSbCl_2$ (2 mol%) is added, mild catalytic activity is observed (14% conversion, 29

hours). The weak catalytic activity of this two-component system relative to **31** illustrates the importance of tethering the Lewis acidic functionality to the gold center for facilitating activity. In an effort to probe whether coordination of an external Lewis base to the antimony center alters the observed activity, we examined the effect of the addition of intermediate-hard Lewis bases which are known to form complexes with halostibines.[30] To this end, substoichiometric amounts of $[Bu_4N][Cl]$ and Ph_3PO were added to catalysis reaction mixtures containing **31**. In both cases, the external Lewis base retards the reaction, with addition of $[Bu_4N][Cl]$ almost completely halting catalytic reactivity.

Table 16. Activities of selected gold catalysts and additives in the cyclization of *N*-(prop-2-yn-1-yl)adamantine-1-carboxamide.

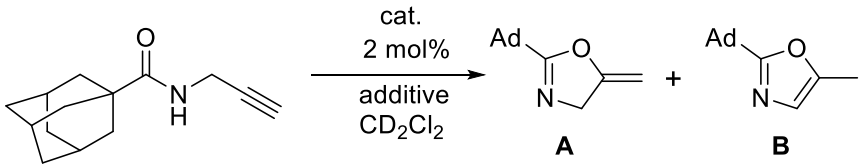

A **B**

Catalyst	Time (h.)	Conversion (%)
31	33	42 (A) + 45 (B) = 87
Ph_3PAuCl	29	0 (A) + 0 (B) = 0
Ph_3PAuCl + $PhSbCl_2$ (2 mol%)	29	5 (A) + 9 (B) = 14
31 + $[Bu_4N][Cl]$ (10 mol%)	33	2 (A) + 0 (B) = 2
31 + Ph_3PO (10 mol%)	33	50 (A) + 31 (B) = 81

Finally, we examined the effect of varying the propargylic amide substrate on the catalytic activity of **31** (Table 17). Compound **31** showed activity in each case, albeit less than that observed in $Ph_3PAuNTf_2$.

Table 17. Activity of compound **31** in the cyclization of various propargylic amides.

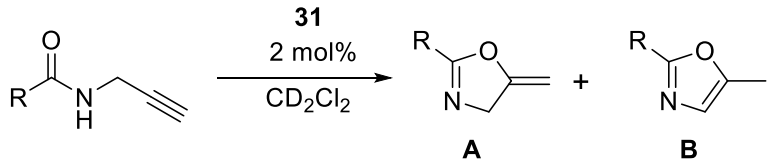

R =	Time (h.)	Conversion (%)
tert-Butyl	26	59 (A) + 29 (B) = 88
Adamantyl	33	42 (A) + 45 (B) = 87
Phenyl	48	43 (A) + 35 (B) = 78
4-Fluorophenyl[a]	49	15 (A) + 14 (B) = 29

a: Reaction mixture is heterogeneous, due to poor substrate solubility.

4.7 Conclusions

In conclusion, we report the synthesis and characterization of a novel ambiphilic antimony ligand containing Lewis acidic dichloroarylstibine group supported by a single phosphine buttress. The coordination chemistry of this ligand to gold is compared with that of the known phosphinylstibine ligand **29**-Ph. The resulting gold species **30** and **31** show "confused" σ-donor-acceptor ligand behavior, with structural metrics suggesting that the antimony ligand is weakly engaged in both cases. While oxidation of **31** was

intractable, the antimony center in **30** undergoes oxidation by *o*-chloranil to afford the gold-stiborane complex **35**.

Compound **31** binds a second equivalent of **29**-Cl or PPh_3 concomitant with the transfer of the gold-bound chloride to the pendant stibine to form the zwitterionic antimonates **32** and **33**, respectively. Compounds **30**, **31**, and **33** were shown to be active catalysts for the silver-salt free electrophilic cyclization of propargylic amides, providing proof of concept that pendant, Lewis acidic stibines can active otherwise inactive Ph_3PAuCl species for catalysis.

4.8 Experimental section

General Considerations. *Antimony compounds should be handled cautiously.* (tht)AuCl,[177] (*o*-$(Ph_2P)C_6H_4)_3Sb$[93], and (*o*-$(Ph_2P)C_6H_4)SbPh_2$[146] were prepared according to previously reported procedures. Solvents were dried by passing through an alumina column. *o*-chloranil and PPh_3 were purchased from Aldrich and used as received. Ambient and low temperature NMR spectra were recorded using a Varian Unity Inova 400 FT NMR (399.59 MHz for ^1H, 100.45 MHz for ^{13}C, 161.74 MHz for ^{31}P) spectrometer. Chemical shifts (δ) are given in ppm and are referenced against residual solvent signals (^1H, ^{13}C) or external H_3PO_4 (^{31}P). Elemental analyses were performed at Atlantic Microlab (Norcross, GA).

Spectral Data for 29-Ph. ^1H NMR (399.53 MHz, $CDCl_3$): δ = 7.14-7.21 (m, 5H, *o*-$P(Sb)C_6H_4$ + PPh + SbPh), 7.21-7.33 (m, 15H, *o*-$P(Sb)C_6H_4$ + PPh + SbPh), 7.35-7.42 (m, 4H, *o*-$P(Sb)C_6H_4$ + PPh + SbPh). ^{13}C NMR (100.46 MHz, $CDCl_3$): δ = 128.68 (d, J = 13.76 Hz), 128.76 (d, J = 15.97 Hz), 129.04 (s), 129.39 (br. s), 130.13 (br. s), 133.89 (d,

J = 17.58 Hz), 134.52 (s), 136.49 (d, *J* = 13.66 Hz), 136.89 (s), 137.07 (d, *J* = 11.15 Hz), 139.74 (d, *J* = 14.46 Hz), 144.96 (d, *J* = 3.01 Hz), 149.12 (d, *J* = 51.83 Hz). $^{31}P\{^{1}H\}$ NMR (161.72 MHz, $CDCl_3$): δ = -6.37 (s).

Synthesis of 29-Cl. **7** (524 mg, 0.57 mmol) and $SbCl_3$ (264 mg, 1.15 mmol) were combined in a Schlenk tube charged with a stirbar. Toluene (ca. 1 mL) was added, and the reaction mixture was heated at 90 °C for 16 h. After cooling, the resulting off-white solid was extracted with CH_2Cl_2 (approx. 30 mL), and filtered over a plug of Celite. All volatiles were removed from the filtrate in vacuo to afford **29**-Ph (649 mg, 82% yield) as a white powder. ^{1}H NMR (399.53 MHz, $CDCl_3$): δ = 7.34-7.45 (m, 10H, PPh), 7.47 (m, 1H, *o*-P(Sb)C_6H_4), 7.56 (m, 1H, *o*-P(Sb)C_6H_4), 7.72 (m, 1H, *o*-P(Sb)C_6H_4), 8.48 (d, 1H, *o*-P(Sb)C_6H_4, *J* = 7.69 Hz). ^{13}C NMR (100.46 MHz, $CDCl_3$): δ = 129.26 (d, *J* = 8.33 Hz), 130.32 (br. d, *J* = 2.21 Hz), 132.23 (br. d, *J* = 3.01 Hz), 132.61 (br. d, *J* = 4.52 Hz), 132.79 (br. d, 1.50 Hz), 133.43 (br. s), 133.51 (br. s), 133.66 (br. s), 135.11 (br. s), 142.48 (d, *J* = 18.28 Hz), 161.29 (d, *J* = 55.65 Hz). $^{31}P\{^{1}H\}$ NMR (161.72 MHz, $CDCl_3$): δ = -19.72 (s).

Synthesis of 30. A solution of **29**-Ph in 2 mL of CH_2Cl_2 was added dropwise to a stirred solution of (tht)AuCl in approx. 0.5 mL CH_2Cl_2 The resultant colorless solution was stirred for 12 h. After concentrating the reaction solution to approx. 0.5 mL, the product was precipitated with excess pentane, collected by filtration, and dried *in vacuo* to give **30** as a pale yellow powder (115 mg, 82% yield). ^{1}H NMR (399.53 MHz, $CDCl_3$): δ = 7.03 (m, 1H, *o*-P(Sb)C_6H_4), 7.18-7.27 (m, 6H, *o*-P(Sb)C_6H_4 + PPh + SbPh), 7.28-7.37 (m, 10H, *o*-P(Sb)C_6H_4 + PPh + SbPh), 7.39-7.48 (m, 6H, *o*-P(Sb)C_6H_4 + PPh + SbPh), 7.55 (m, 1H *o*-P(Sb)C_6H_4). ^{13}C NMR (100.46 MHz, $CDCl_3$): δ = 129.25 (s), 129.27 (d, *J* = 50.33 Hz),

129.30 (br. d, J = 2.61 Hz), 129.32 (d, J = 14.46 Hz), 131.94 (br. d, J = 2.91 Hz), 132.14 (br. d, J = 2.21 Hz), 134.07 (d, J = 9.14 Hz), 134.74 (d, J = 14.56 Hz), 136.73 (s), 138.89 (d, J = 13.66 Hz), 139.51 (d, J = 4.52 Hz), 146.08 (d, J = 24.41 Hz). ^{31}P {1H} NMR(161.72 MHz, $CDCl_3$): δ = 32.27 (s).

Synthesis of 31. A solution of **29**-Cl (498 mg, 1.09 mmol) in 5 mL CH_2Cl_2 was added dropwise to a stirred solution of (tht)AuCl (351.7, 1.09 mmol) in 5 mL CH_2Cl_2 cooled to -78°C. After stirring for -78°C for 1 h., the reaction mixture was allowed to warm to room temperature. The resultant suspension was filtered over a plug of celite to remove a fine black precipitate, and all volatiles were removed from the filtrate. The residue was recrystallized from 1:1 CH_2Cl_2/pentane, and the white precipitate was filtered and dried *in vacuo* to give 406.6 mg (54.0%) of **31**. ^{1}H NMR (399.53 MHz, $CDCl_3$): δ = 7.24 (dd, 1H, *o*-P(Sb)C_6H_4, J = 11.21 Hz, 7.83 Hz), 7.46-7.54 (m, 9H, *o*-P(Sb)C_6H_4 + PPh), 7.54-7.61 (m, 2H, PPh), 7.76 (pt, 1H, *o*-P(Sb)C_6H_4), 8.71 (dd, 1H, *o*-P(Sb)C_6H_4, J = 7.56 Hz, 3.42 Hz). ^{13}C NMR (100.46 MHz, $CDCl_3$): δ = 127.3 (d, J = 65.70 Hz), 129.95 (d, J = 12.18 Hz), 131.23 (d, J = 9.17 Hz), 132.99 (s), 133.78 (s), 134.48, J = 13.81 Hz), 135.31 (d, J = 6.78 Hz), 157.04 (d, J = 23.61 Hz). ^{31}P {1H} NMR(161.72 MHz, $CDCl_3$): δ = 24.71 (s).

Synthesis of 32. A solution of (tht)AuCl (168.6 mg, 0.37 mmol) in 3 mL CH_2Cl_2 was added dropwise to a stirred solution of **29**-Cl, immediately forming a bright yellow solution. After stirring for 4 h., the resulting yellow suspension was concentrated, and excess (10 mL) Et_2O was added to precipitate the product. The supernatant was decanted, and the precipitated yellow solid was dried *in vacuo* to obtain 104.7 mg (49%) of **32** as a

yellow solid. ^{1}H NMR (399.53 MHz, $CDCl_3$): δ = 7.39 (d, 2H, *o*-P(Sb)C_6H_4, J = 7.95 Hz), 7.49 (pt, 2H, *o*-P(Sb)C_6H_4), 7.52-7.63 (m, 14H, PPh), 7.63-7.69 (m, 6H, PPh), 7.74 (pt, 2H, *o*-P(Sb)C_6H_4), 8.71 (d, 2H, *o*-P(Sb)C_6H_4, J = 8.42 Hz). ^{31}P {1H} NMR(161.72 MHz, $CDCl_3$): δ = 35.14 (br. s). Due to the poor solubility of **32**, a satisfactory ^{13}C{^{1}H} NMR spectrum could not be obtained.

Synthesis of 33. Triphenylphosphine (77 mg, 0.29 mmol) was added as a solid to a stirred solution of (tht)AuCl (94 mg, 0.29 mmol) in 3 mL THF, and the resultant solution was stirred for 10 minutes. A solution of **29**-Cl in 1 mL THF was added dropwise to the stirred (tht)AuCl/PPh_3 solution. The resultant bright yellow solution was allowed to stand overnight, depositing a large amount of yellow crystals. The supernatant was decanted, and the solid was washed with 2 mL cold THF and dried *in vacuo* to afford **33** (198 mg, 70% yield) as yellow crystalline solid. ^{1}H NMR (399.53 MHz, $CDCl_3$, 23 °C): δ = 7.27-7.67 (m, 28H, PPh_3 + PPh + *o*-P(Sb)C_6H_4), 8.73 (d, 1H, *o*-P(Sb)C_6H_4, $^{3}J_{H\text{-}H}$ = 7.69 Hz). ^{1}H NMR (399.53 MHz, $CDCl_3$, -40 °C): δ = 7.36-7.44 (m, 2H, PPh), 7.44-7.50 (m, 4H, PPh_3), 7.50-7.68 (m, 21H, PPh + PPh_3 + *o*-P(Sb)C_6H_4), 7.68-7.74 (m, 1H, *o*-P(Sb)C_6H_4), 8.81 (dd, 1H, *o*-P(Sb)C_6H_4, $^{3}J_{H\text{-}H}$ = 8.05 Hz, $^{4}J_{H\text{-}H}$ = 3.11 Hz). ^{13}C{^{1}H} NMR (100.46 MHz, $CDCl_3$, 23 °C): δ = 128.39 (br. s, PPh), 128.59 (br. s, PPh_3), 130.80 (br. s, PPh), 131.30 (br. s, PPh_3), 132.43 (br. s, *o*-P(Sb)C_6H_4), 132.65 (br. s), 132.87 (br. s, PPh), 133.28 (br. s, PPh_3), 133.69 (br. s, *o*-P(Sb)C_6H_4). ^{31}P{^{1}H} NMR (161.72 MHz, $CDCl_3$, 23 °C): δ = 34.02 (br. s, 1P), 41.49 (br. s, 1P). ^{31}P{^{1}H} NMR (161.72 MHz, $CDCl_3$, -40 °C): δ = 35.47 (d, 1P, $^{2}J_{P\text{-}P}$ = 299.00 Hz), 42.43 (d, 1P, $^{2}J_{P\text{-}P}$ = 299.00 Hz).

Synthesis of 35. A solution of *o*-chloranil (231.4 mg, 0.30 mmol) in 4 mL CH_2Cl_2 was added dropwise to a stirred solution of **30** in 2 mL CH_2Cl_2. The resulting orange-red solution was stirred for 15 minutes, then concentrated to 2 mL. Excess (10 mL) pentane was added, precipitating an orange solid, which was filtered and dried *in vacuo* to give 261.3 mg (85.6%) of **35**. ^{1}H NMR (399.53 MHz, $CDCl_3$): δ = 7.24-7.26 (m, 1H, *o*-P(Sb)C_6H_4), 7.28-7.36 (m, 3H, SbPh + PPh), 7.36-7.43 (m, 4H, SbPh + PPh), 7.36-7.55 (m, 10H, *o*-P(Sb)C_6H_4) + SbPh + PPh), 7.55-7.62 (m, 2H, *o*-P(Sb)C_6H_4), 7.62-7.69 (m, 4H, PPh). ^{31}P{^{1}H} NMR (161.72 MHz, $CDCl_3$): δ = 41.49 (s).

Catalytic Cyclization of Propargyl Amides. Propargylic amide substrates were synthesized according to reported procedures.[171-173]. Conversion percentages were estimated using durene as an internal standard. A typical procedure is as follows: The selected substrate (0.33 mmol) is dissolved in 0.70 mL of a 3.92 x 10^{-2} M solution of durene in CD_2Cl_2. The resulting solution was added to an NMR tube charged with the selected gold catalyst (2 mol%). During the course of the catalysis reactions, the reaction mixtures were kept in the dark.

Computational Details. Density functional theory (DFT) calculations (full geometry optimizations) were carried out on **29**-Ph, **29**-Cl, **30**, **31**, **33**, and **35** starting from their respective crystal structure geometries with the Gaussian09[133] program (PBE0[178] functional, with 6-31G for H, C, 6-311+G(d) for O, P, Cl, and ccpVTZ for Sb,[96] Au,[134] and Stuttgart relativistic small core ECPs for Sb,[97] Au[134]). Frequency calculations carried out at the optimized geometries found no imaginary frequencies. The optimized structures

were also subjected to natural bond orbital (NBO)[98] analysis, and the resulting NBOs were plotted using the Jimp 2[99] program.

Crystallography. Single crystals of **29**-Ph and **32** suitable for X-ray diffraction were grown by slow diffusion of pentane into a $CHCl_3$ solution of the compound at room temperature. Single crystals of **29**-Cl suitable for X-ray diffraction were grown by slow diffusion of pentane into a toluene solution of the compound at room temperature. Single crystals of **30** were obtained by slow diffusion of Et_2O into a solution of the compound in CH_2Cl_2. Single crystals of **31** by layering a solution of the compound in CH_2Cl_2 with pentane. Single crystals of **33** suitable for X-ray diffraction were obtained by allowing a concentrated $CHCl_3$ solution of the compound to stand for ca. 2 days. Single crystals of **35** suitable for X-ray diffraction were grown by slow diffusion of Et_2O into a toluene solution of the compound at room temperature. Crystal data, details of data collection, and structure refinement parameters for compounds **29**-Ph, and **29**-Cl are compiled in Table 18. Crystal data, details of data collection, and structure refinement parameters for compounds **30** and **31** are compiled in Table 19. Crystal data, details of data collection, and structure refinement parameters for compounds **32**, **33**, and **35** are compiled in Table 20. The crystallographic measurements were performed at 110(2) K using a Bruker APEX-II CCD area detector diffractometer, with a graphite-monochromated Mo-Kα radiation (λ = 0.71069 Å). In each case, a specimen of suitable size and quality was selected and mounted onto a nylon loop. The semi-empirical method SADABS[100] was applied for absorption correction. The structure was solved by direct methods and refined by the full-matrix least-square technique against F^2 with the anisotropic temperature

parameters for all non-hydrogen atoms. All H atoms were geometrically placed and refined in riding model approximation. Data reduction and further calculations were performed using the Bruker SAINT+[101] and SHELXTL NT[102] program packages.

Table 18. Crystal data, data collections, and structure refinements for **29**-Ph and **29**-Cl.

	29-Ph	**29**-Cl
Formula	$C_{30}H_{24}PSb$	$C_{18}H_{14}Cl_2PSb$
Formula Weight	537.25	453.94
Crystal Size (mm)	0.17 x 0.11 x 0.10	0.24 x 0.21 x 0.14
Crystal System	Triclinic	Monoclinic
Space Group	P-1	P2(1)/n
a (Å)	8.1982(18)	9.924(6)
b (Å)	12.539(3)	13.713(9)
c (Å)	12.781(3)	14.846(7)
α (°)	109.757(2)	90
β (°)	100.887(2)	118.36(3)
γ (°)	97.066(2)	90
V (Å^3)	1189.2(5)	1777.9(18)
Z	2	4
ρ_{calc} (g/cm^3)	1.500	1.643
μ (mm^{-1})	1.243	1.933
F(000)	540	832
T (K)	110(2)	110(2)
Scan mode	ω, φ	ω, φ
hkl Range	-10 → 10	-13 → 13
	-16 → 15	-18 → 18
	-0 → 16	-19 → 20
Reflections collected	13810	21195
Unique reflections [Rint]	5364 [0.0340]	4610 [0.0603]
Reflns. used for refinement	5364	4610
Refined parameters	302	199
GooF	1.007	1.012
R1[a], *w*R2[b] (all data)	0.0420, 0.0720	0.0502, 0.0767
ρ_{fin} (max., min.) (eA^{-3})	1.035, -0.837	0.623, -0.616

[a]R1 = $\sum||F_o| - |F_c||/\sum|F_o|$. [b] *w*R2 ($[w(F_o^2 - F_c^2)^2]/[\sum w(F_o^2)^2]$)$^{1/2}$; $w = 1/[\sigma^2(F_o^2) + (ap)^2 + bp]$; $p = (F_o^2 + 2F_c^2)/3$ with a = 0.0095 for **29**-Ph, and 0.0306 for **29**-Cl; and b = 2.9705 for **29**-Ph, and 0.0000 for **29**-Cl.

Table 19. Crystal data, data collections, and structure refinements for **30** and **31**.

	30	**31**
Formula	$C_{30}H_{24}AuClPSb$	$C_{18}H_{14}AuCl_3PSb$•0.5($CHCl_3$)
Formula Weight	769.63	746.01
Crystal Size (mm)	0.13 x 0.12 x 0.12	0.12 x 0.10 x 0.08
Crystal System	Triclinic	Monoclinic
Space Group	P-1	C 1 2/c 1
a (Å)	12.895(2)	24.818(3)
b (Å)	13.118(2)	16.172(2)
c (Å)	17.711(3)	11.0183(13)
α (°)	90.941(2)	90
β (°)	99.553(2)	102.076(5)
γ (°)	118.917(2)	90
V (Å^3)	2569.9(8)	4324.3(9)
Z	4	8
ρ_{calc} (g/cm^3)	1.989	2.292
μ (mm^{-1})	6.937	8.659
F(000)	1464	2776
T (K)	110(2)	110(2)
Scan mode	ω, φ	ω, φ
hkl Range	-15 → 15	-25 → 32
	-16 → 16	-20 → 21
	-21 → 21	-14 → 14
Reflns. collected	26823	38100
Unique reflns. [Rint]	10050 [0.0516]	4987 [0.0535]
Reflns. used for refinement	10050	4987
Refined parameters	613	253
GooF	1.026	1.042
R1[a], *w*R2[b] (all data)	0.0591, 0.1163	0.0523, 0.0573
ρ_{fin} (max., min.) (eA^{-3})	4.204, -1.574	1.447, -1.561

[a]$R1 = \sum||F_o| - |F_c||/\sum|F_o|$. [b] $wR2 ([w(F_o^2 - F_c^2)^2]/[\sum w(F_o^2)^2])^{1/2}$; $w = 1/[\sigma^2(F_o^2) + (ap)^2 + bp]$; $p = (F_o^2 + 2F_c^2)/3$ with $a = 0.0591$ for **30**, and 0.0100 for **31**; and $b = 7.5896$ for **30**, and 39.2425 for **31**.

Table 20. Crystal data, data collections, and structure refinements for **32**, **33**, and **35**.

	32	**33**	**35**
Formula	$C_{36}H_{28}AuCl_5P_2Sb_2$	$C_{36}H_{29}AuCl_3P_2Sb$ •3($CHCl_3$)	$C_{36}H_{24}AuCl_5O_2PSb$ •(C_7H_8)
Formula Weight	1140.24	1306.75	1107.67
Crystal Size (mm)	0.36 x 0.08 x 0.04	0.28 x 0.23 x 0.12	0.20 x 0.13 x 0.06
Crystal System	Triclinic	Orthorhombic	Monoclinic
Space Group	P-1	P2(1)2(1)2(1)	P21/n
a (Å)	11.9081(8)	14.159(5)	12.4164(10)
b (Å)	12.1399(8)	16.514(5)	21.4726(17)
c (Å)	15.2606(11)	20.176(6)	13.8391(11)
α (°)	86.9680(10)	90	90
β (°)	73.2090(10)	90	98.2900(10)
γ (°)	62.4240(10)	90	90
V (Å^3)	1863.6(2)	4718(3)	3651.1(5)
Z	2	4	2
ρ_{calc} (g/cm^3)	2.032	1.840	1.931
μ (mm^{-1})	5.836	4.455	5.199
F(000)	1080	2520	2044
T (K)	110(2)	110(2)	110(2)
Scan mode	ω, φ	ω, φ	ω, φ
hkl Range	-14 → 15	-19 → 19	-16 → 16
	-15 → 15	-22 → 22	-28 → 28
	0 → 19	-27 → 27	-18 → 18
Reflns. collected	22123	58351	44880
Unique reflns. [Rint]	8457 [0.0453]	12410 [0.0554]	9097 [0.0551]
Reflns. used for refinement	8457	12410	9097
Refined parameters	415	497	451
GooF	1.071	1.016	1.014
R1[a], *w*R2[b] (all data)	0.0356, 0.0641	0.0371, 0.0610	0.0382, 0.0610
ρ_{fin} (max., min.) (eA^{-3})	1.119, -0.974	1.150, -1.206	0.751, -0.927

[a]R1 = $\sum||F_o| - |F_c||/\sum|F_o|$. [b] *w*R2 ($[w(F_o^2 - F_c^2)^2]/[\sum w(F_o^2)^2]^{1/2}$; $w = 1/[\sigma^2(F_o^2) + (ap)^2 + bp]$; $p = (F_o^2 + 2F_c^2)/3$ with a = 0.0210 for **32**, 0.0074 for **33**, and 0.0247 for **35**; and b = 0.4147 for **32**, 0.0000 for **33**, and 0.5761 for **35**.

5. REDOX AND ANION EXCHANGE CHEMISTRY OF A NICKEL STIBINE COMPLEX[3]

5.1 Introduction

In 1995, Green[17] introduced the Covalent Bond Classification as a new method for the description of ligands and the way by which they bind to metal centers (M). This method, which is predicated on the nature of the bond connecting M to the ligating atom of the ligand, identifies three distinct situations. In the first situation, a Lewis basic or L-type ligand acts as a two-electron donor to form a L→M dative interaction. In the second situation, which is the charge reverse analog of the first one, a Lewis acidic or Z-type ligand interacts with the metal via a M→L interaction.[18-20, 24, 118-127] A third, intermediate situation arises when a one electron donor or X-type ligand combines with an electron from the metal center to form a covalent bond. Prototypical examples of such ligands include PR_3 or CO for L-type ligands, H or CH_3 for X-type ligands, and BR_3 for Z-type ligands. As part of our ongoing interest in the coordination chemistry of redox active ligands, we have now questioned whether the L-, X-, and Z-ligand function could be sustained by a single ligating element. In this communication, we describe a Ni/Sb platform in which the antimony ligand can be switched from L to X to Z via successive formal one electron redox processes.

---

[3] Reprinted in part with permission from, "Redox and Anion Exchange Chemistry of a Stibine–Nickel Complex: Writing the L, X, Z Ligand Alphabet with a Single Element"; Jones, J. S.; Wade, C. R.; Gabbaï, F. P. *Angew. Chem. Int. Ed.* **2014**, *53*, 8876, Copyright 2014 by Wiley-VCH Verlag GmbH & Co.

5.2 Synthesis of a zerovalent nickel complex

Reaction of (*o*-(Ph_2P)C_6H_4)$_3$Sb (**7**)[93] with Ni(PPh_3)$_4$ in THF afforded LNi(PPh_3) (**36**) as an orange powder (Scheme 1). Solutions of compound **36** slowly decompose at ambient temperature, but are stable indefinitely at -20 °C. The ^{31}P NMR spectrum of **36** in C_6D_6 consists of a doublet at 52.54 ppm, a triplet at 39.73 ppm ($^2J_{P\text{-}P}$ = 46.89Hz), and a singlet at -8.62 ppm in a 2:1:1 ratio, suggesting a κ-P-P-Sb coordination mode of **7** to a [(Ph_3P)Ni] fragment.

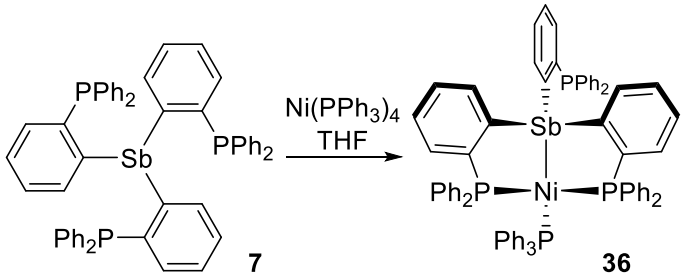

Figure 68. Synthesis of **36**.

This spectroscopic assignment was corroborated by a single crystal diffraction study (Figure 69). In the solid state structure of **36**, the nickel center adopts a distorted tetrahedral geometry with large P-Ni-P angles whose sum is equal to 348.75(15) °. As a result of the constraints enforced by the ligand backbone, the four coordinate antimony center also displays an unusual geometry characterized by a large Ni-Sb-C angle of 159.77(11)°. The Ni-Sb distance of 2.4574(10) Å in **36** is comparable to the average Ni-Sb distance of

2.449(2) Å in $Ni_2(CO)_4(\mu_2\text{-}Ph_2SbOSbPh_2)_2$, one of the few structurally characterized arylstibine complexes of zerovalent nickel.[179]

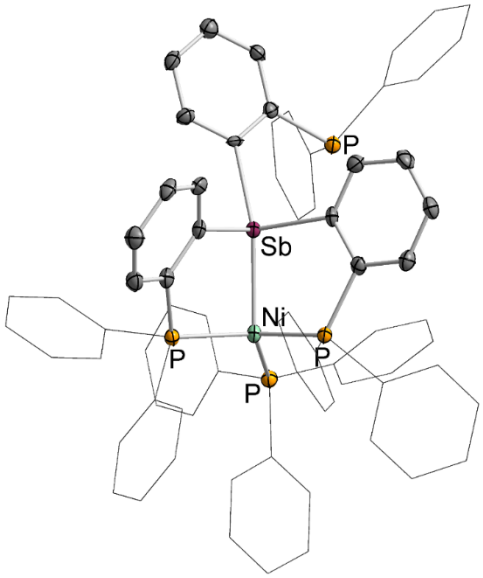

Figure 69. Structure of compound **36**. Thermal ellipsoids are drawn at the 50% probability level. Selected phenyl rings are drawn in wireframe, and hydrogens and solvent molecules are omitted for clarity. Selected bond lengths (**Å**) and angles (°): Sb-Ni 2.4574(10), Ni-Sb-C1 159.76(11), P2-Ni-P3 114.38(5), P2-Ni-P4 113.88(5), P3-Ni-P4 120.49(5).

5.3 Redox and anion exchange chemistry of a nickel stibine complex

With compound **1** in hand, we sought to determine whether the Sb-Ni heterobimetallic core could sustain oxidation without decomposition. Gratifyingly, **36** undergoes a clean, two-electron oxidation by $PhICl_2$ in toluene to afford the dark purple **23**-Cl characterized by a single ^{31}P NMR resonance at 35.42 ppm in $CDCl_3$ (Scheme 1).

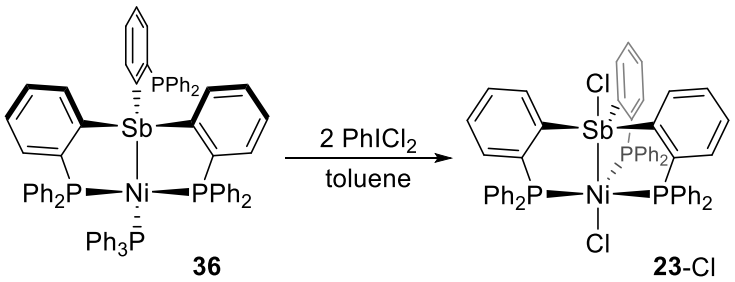

Figure 70. Oxidation of **36** to form **23**-Cl.

Compound **23**-Cl was previously prepared by reaction of **7** with $NiCl_2$•$6H_2O$ and characterized in a dissertation by Casey R. Wade. The structural parameters of **23**-Cl are taken directly from this document and used in the context of comparison with other compounds described in this chapter. The Sb-Ni lantern complex **23**-Cl features a Sb-Ni distance (2.4852(5) Å) almost identical to that in **36** (Sb-Ni 2.4574(10) Å). In contrast to **36** however, the nickel atom adopts a trigonal bipyramidal geometry with the antimony atom and a chloride ligand at the axial positions. The most distinguishing feature of **23**-Cl is the presence of a chloride ligand bound to the antimony center, in a position *trans* from the nickel atom.

While **36** can be regarded as a classical stibine complex, the presence of an antimony-bound chloride ligand in **23**-Cl makes its classification somewhat more ambiguous. Indeed, with chloride as an extra ligand, the antimony moiety in **23**-Cl is tetrasubstituted and thus akin to a stiboranyl unit bound to the nickel atom.[180] On the basis of this analysis, it can be proposed that oxidation of **36** into **23**-Cl triggers an L- to X-type conversion of the antimony ligand.

With the observation of the L- and X-ligand functions on the same platform, the conversion of the antimony center into a Lewis acidic, Z-type stiborane ligand became a stimulating fundamental possibility.[181, 182] In our first approach to this idea, **23**-Cl was allowed to react with catechol in the presence of a base to yield red-orange **37** (Figure 71). The ^{31}P NMR spectrum of **37** in d_8-toluene consists of a doublet at 60.31 ppm and a triplet at -52.87 ppm ($^2J_{P\text{-}P}$ = 139.20 Hz), the strong upfield shift of the latter resonance being diagnostic of an *ortho*-metallated phosphine in a four-membered chelate ring.[183]

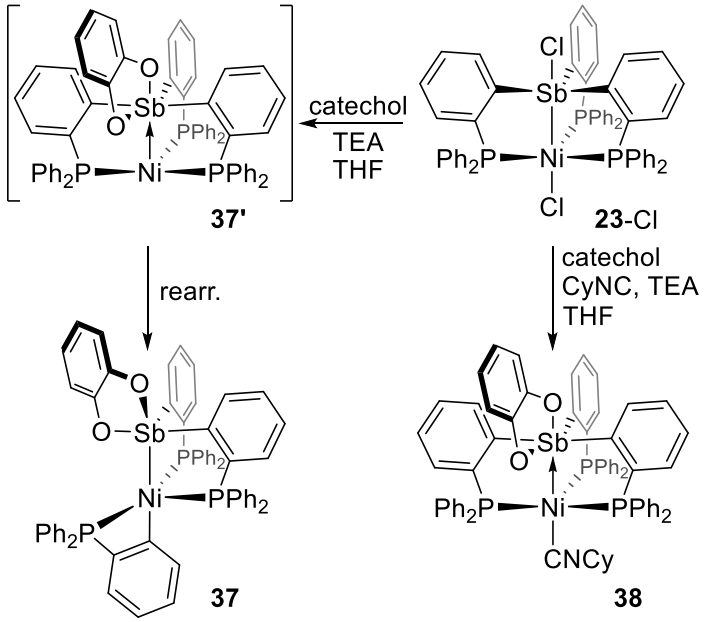

Figure 71. Synthesis of **37** and **38** from **23**-Cl.

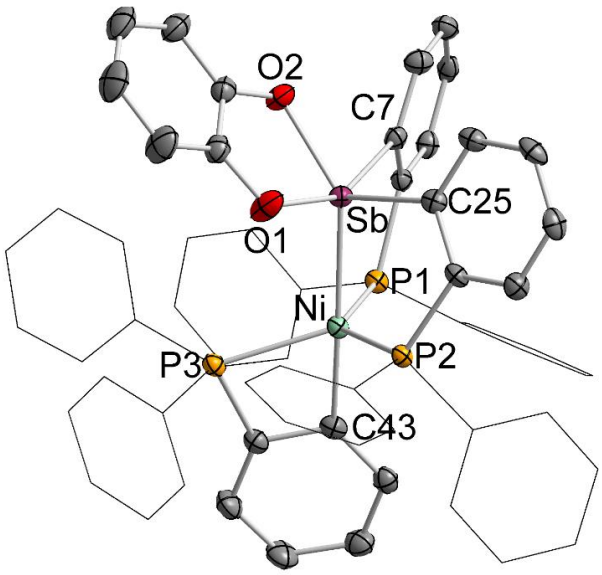

Figure 72. Structure of compound **37**. Thermal ellipsoids are drawn at the 50% probability level. Selected phenyl rings are drawn in wireframe, and hydrogens and solvent molecules are omitted for clarity. Selected bond lengths (**Å**) and angles (°): Sb(1)-Ni(1) 2.4564(6), Sb(1)-O(1) 2.0495(19), Sb(1)-O(2) 2.127(2), Ni(1)-C(43) 1.966(3), P(1)-Ni(1)-P(3) 110.99(3), P(2)-Ni(1)-P(3) 117.30(3).

The solid state structure of **37** confirmed migration of an *ortho*-diphenylphosphinophenylene group from antimony to nickel, leading us to speculate the intermediacy of nickel(0) complex (**37'**) that would evolve into **37** via insertion of the nickel center into a Sb-C bond. Although the Sb-Ni distance of 2.4564(6) Å varies little from the Sb-Ni distance of 2.4852(5) Å found in **23**-Cl, the loss of a phosphine buttress in **37** causes the antimony center to assume a distorted ($\tau = 0.23$) square pyramidal geometry. With the goal of activating small molecules *via* the speculated intermediate **37**', we next repeated the reaction under an atmosphere of H_2. This synthetic modification did not alter the course of this reaction, with **37** being the only product observed. This result suggests

that the insertion of the nickel center into an Sb-C bond is too rapid to be intercepted by a substrate.[27, 184]

With the goal of damping the reactivity of the low valent nickel center in **37'** and its tendency toward insertion reactions, we next considered whether the use of a π-acidic ligand would help stabilize the electron-rich nickel atom. To this end, the same reaction was repeated in the presence of cyclohexyl isocyanide. Gratifyingly, this reaction afforded the stiborane nickel complex **38** in good yield (Figure 71). While orange-red solutions of 38 slowly decompose in air, solid samples appear to be indefinitely stable. The ^{31}P NMR spectrum of **38** in $CDCl_3$ shows a doublet at 68.91 ppm and a triplet at 39.68 ppm ($^2J_{P\text{-}P}$ = 83.89 Hz), indicating the inequivalence of the phosphine arms of the ligand. The crystal structure of **38** confirmed coordination of the catecholate ligand to the antimony center leading to the formation of a square pyramidal triarylcatecholatostiborane moiety whose open square base faces the neighbouring nickel atom (Figure 2).[185] Correspondingly, the isocyanide tris(phosphine) nickel moiety forms a trigonal pyramid ($\Sigma\angle$(P-Ni-P) = 357.8(1)°) with the antimony positioned directly above the NiP_3 trigonal base. Although the Sb-Ni distance in **38** (2.6253(4) Å) is 0.17 Å longer than that measured in **36** (2.4574(10) Å), the observed arrangement of the two moieties supports the presence of a direct Ni→Sb interaction.

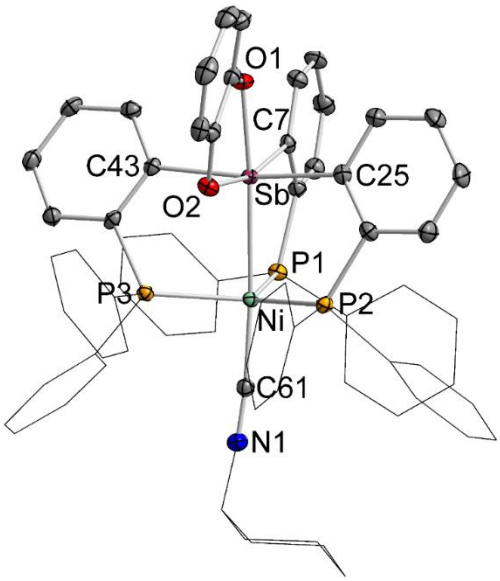

Figure 73. Structure of compound **38**. Thermal ellipsoids are drawn at the 50% probability level. Selected phenyl rings are drawn in wireframe, and hydrogens and solvent molecules are omitted for clarity. Selected bond lengths (Å) and angles (°): Sb-Ni 2.6253(4), Sb-O1 2.0920(12), Sb-O2 2.1169(12), Ni-C61 1.8586(19), N1-C61 1.161(2), O1-Sb-Ni 173.06(3), O2-Sb-C7 166.99(6), C25-Sb-C43 170.65(6), P1-Ni-P2 120.43(2), P1-Ni-P3 113.919(19), P2-Ni-P3 123.49(2), C61-N1-C62 174.73(19).

In support of this view, the $\nu_{(CN)}$ of **38** (2142 cm^{-1}), which is considerably higher than that found in (CyNC)Ni(PPh_3)$_3$ (2020 cm^{-1}),[111] shows that the transfer of electron density from nickel to antimony reduces the metallobasicity of the nickel atom and thus the strength of the Ni→isocyanide π-backbonding interaction. A similar effect has been observed by Figueroa upon coordination of a Lewis acidic thallium cation to isocyanide nickel(0) complexes.[186] A precedent also exists in carbonyl rhodium and iridium boratrane complexes,[187, 188] which feature significantly higher CO stretching frequencies than their Lewis acid-free analogues. Finally, we note that the observed CyNC C-N stretching frequency for **38**, is significantly lower than that found in the valence isoelectronic

compound **28** (ν_{CyNC} = 2181 cm^{-1}),[149] consistent with the stronger backbonding ability of nickel relative to platinum.[189] From these structural and spectroscopic features, we conclude that the stiborane moiety in **38** acts as a Z-type ligand.[35, 181, 182, 190] The presence of a Ni→Lewis acid interaction in **38** is reminiscent of the situation encountered in nickel borane or alane complexes such as **A**,[191] **B**[27] and **C**[25] which have been obtained from $(COD)_2Ni$ for **A** and **C** or by reduction of a nickel halide precursor for **B** (Figure 74). Although complex **38** is chemically related to these derivatives, it is unique in that the Z-type ligand function is the result of an anion induced internal redox reaction.

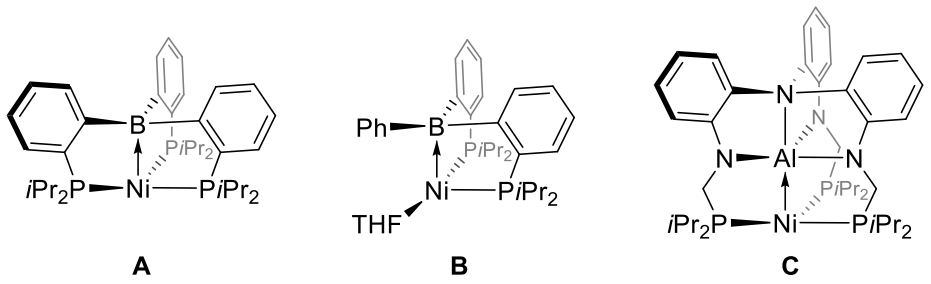

Figure 74. Examples of known zerovalent nickel complexes featuring a Z-type ligand.

5.4 NBO analyses of **36**, **23**-Cl, and **38**.

This view is supported by the Natural Bond Orbital (NBO) analysis of the Sb-Ni bonding present in these complexes (Figure 75). Implementation of this method at the DFT optimized geometries shows that while the Sb-Ni bond in **36** may be described as a lp(Sb)→Ni donor-acceptor interaction (E^2 = 53.07 kcal/mol), the Sb-Ni bond in **23**-Cl is treated as a covalent bond with a distinct polarization toward the nickel atom (Sb 36.3% /

Ni 57.7%). Weaker Ni→σ*(Sb-C) interactions were also observed in the case of 36, which along with the disphenoid geometry at antimony suggests that the stibine moiety acts as a 'confused' σ-donor/acceptor towards the nickel center. Overall, these results show that the Sb-Ni bonding in **36** is best described as a classical Sb→Ni dative bond, in which the stibine moiety of **7** acts as an L-type ligand. In the case of **23**-Cl, the presence of a polar covalent bond shows that the antimony center acts as a strongly σ-donating, X-type stiboranyl fragment.

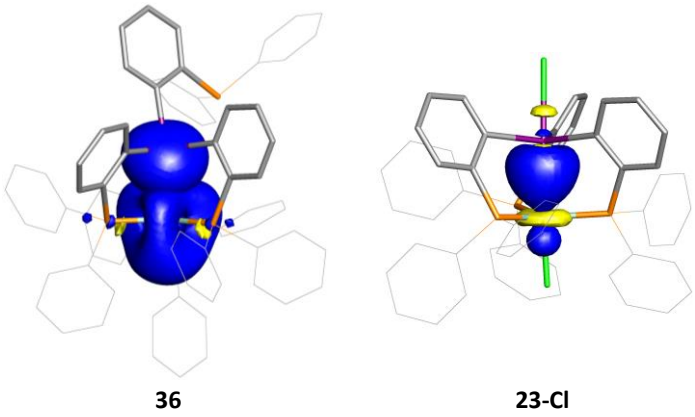

Figure 75. NBO plots of the major Sb-Ni bonding interactions in compounds **36** and **23**-Cl (isodensity value = 0.05). Hydrogen atoms are omitted, and selected phenyl groups are truncated for clarity.

The nature of the Ni→Sb interaction present in **38** has also been probed using the NBO method (Figure 76). The NBO analysis separates **38** into four distinct units: (*o*-$(Ph_2P)C_6H_4)_3Sb$, Ni, *o*-$O_2C_6H_4$, and CyNC. The antimony-based accepting orbital for the major Ni→Sb interaction is therefore parsed as a vacant p orbital. Inspection of the NBO

output finds a series of Ni→p(Sb) and Ni→σ*(Sb-C) donor-acceptor interactions involving the Ni d_{z^2} orbital . The sum of the second order stabilization energies of these interaction (ΣE^2) is equal to 20.85 kcal/mol, a value significantly smaller than that of the lp(Sb)→Ni in **36** (E^2 = 53.07 kcal/mol). These results show that the umpolung of the Ni-Sb bond induced by conversion of **36** into **38** is accompanied by a relative weakening of the dative interaction present at the core of this complex. This bond umpolung bears an interesting parallel with the donor/acceptor role inversion described by Wagler for a family of SnPd complexes.[192] Finally, it is important to note that in contrast to compound **38**, NBO analysis of the valence isoelectronic compound **28** finds a NLMO corresponding to the Sb-Pt bond which is strongly polarized towards the platinum center (Sb 29.9% / Pt 60.2%). While the two species undoubtedly lie close to each other on the spectrum of Sb-M bond polarization, the enhanced covalency of the Sb-Pt bond in **28** relative to the Sb-Ni bond in **38** can be attributed to the larger 5d orbitals of Pt, which may allow for superior overlap with antimony relative to **38**.

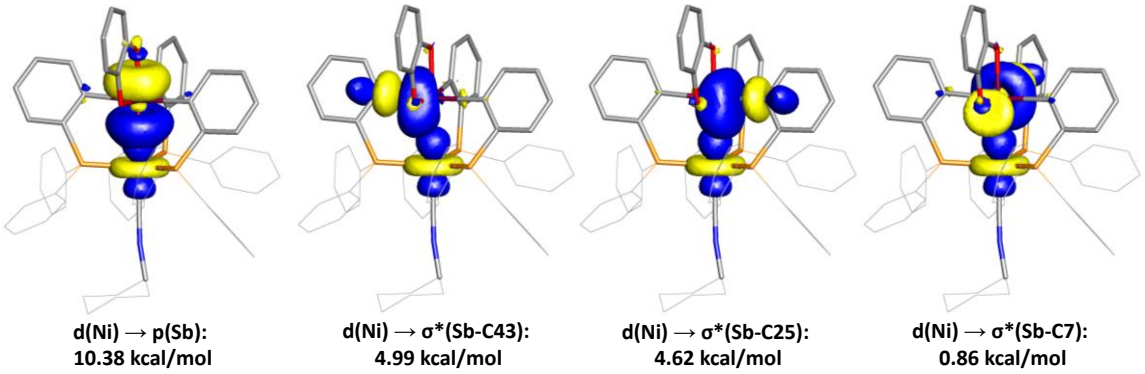

Figure 76. NBO plots (isodensity value = 0.05) of the major Ni→Sb donor-acceptor interactions and their corresponding calculated second-order perturbation energies in **38**. Hydrogen atoms are omitted, and some phenyl and the cyclohexyl rings are drawn in wireframe for clarity.

5.5 Conclusions

In summary, we provide an example of a complex in which the ligating atom can assume all three Covalent Bond Classification ligand functions. Conversion among these three ligand functions is achieved by a combination of redox and anion exchange reactions. Structural metrics and NBO analysis support the changing nature of the Sb-Ni interaction, with the best description of the Sb-Ni interaction changing from an Sb→Ni dative bond in **36**, to a Sb-Ni covalent bond in **23**-Cl, and finally to a Ni→Sb dative bond in **38**.

The ability of the modulate the ligand properties of the coordinated antimony center after complexation may prove to be a promising strategy for tuning transition metal centers to promote unusual reactivity. In particular, we note that anion binding at the antimony center of **23**-Cl in the absence of a induces the insertion of the nickel center into an Sb-C bond. This "unmasking" of a reactive metal center *via* a coordination non-innocent

antimony ligand may prove to be a useful strategy for the indirect modulation of a catalyst *in situ*.

5.6 Experimental section

General Considerations. *Antimony compounds should be handled cautiously.* (*o*-$(Ph_2P)C_6H_4)_3Sb$[93] (**7**) and $Ni(PPh_3)_4$,[193] and $PhICl_2$[194] were prepared according to reported procedures. Catechol was purchased from Aldrich and recrystallized prior to use. All preparations were carried out under an atmosphere of dry N_2 unless otherwise specified. Solvents were dried by passing through an alumina column (pentane and CH_2Cl_2) or refluxing under N_2 over Na/K (Et_2O and THF). Ambient temperature NMR spectra were recorded on a Varian Unity Inova 400 FT NMR (399.59 MHz for ^1H, 161.74 MHz for ^{31}P, 100.45 MHz for ^{13}C) spectrometer. Chemical shifts (δ) are given in ppm and are referenced against residual solvent signals (^1H, ^{13}C) or external H_3PO_4 (^{31}P). IR spectra were recorded on a Mattson ATI Genesis FT-IR spectrometer using KBr pellets. Elemental analyses were performed at Atlantic Microlab (Norcross, GA).

Synthesis of 36. A solution of $Ni(PPh_3)_4$ (174 mg, 157 μmol) in ~3 mL THF was added dropwise to a stirred suspension of L (142 mg, 157 μmol) in ~5 mL THF, immediately forming a dark red solution. The solution was stirred for 12 h. to give an orange suspension. The reaction mixture was filtered and washed with THF(2 x 2 mL) and dried *in vacuo* to yield 123 mg (64%) of **36** as a bright orange powder. ^1H NMR (399.53 MHz; C_6D_6): δ = 6.61-7.12 (m, 36H, *o*-P(Sb)C_6H_4 + Ph-C*H* + PPh_3 *meta*- and *ortho*-Ph-C*H*), 7.17-7.26 (m, 8H, *o*-P(Sb)C_6H_4 + Ph-C*H)*, 7.27-7.58 (m, 10H, *o*-P(Sb)C_6H_4 + PPh_3 *ortho*-Ph-C*H*), 7.73 (d, 2H, *o*-P(Sb)C_6H_4 $^3J_{H\text{-}H}$ = 7.57 Hz), 8.14 (d, 1H, *o*-P(Sb)C_6H_4, $^3J_{H\text{-}H}$ =

6.10 Hz). $^{31}P\{^{1}H\}$ NMR (161.73 MHz; C_6D_6): δ= -8.62 (s, 1P, free arm), 39.73 (t, 1P, PPh_3, $^{2}J_{P\text{-}P}$ = 46.89Hz), 52.54 (d, 2P, $^{2}J_{P\text{-}P}$ = 46.89Hz). A satisfactory ^{13}C NMR spectrum could not be obtained, due to poor solubility in common organic solvents and decomposition in solution at ambient temperature. Elemental analysis calculated (%) for $C_{72}H_{57}NiP_4Sb$: C 70.50, H 4.68; found C 69.23, H 4.95.

Synthesis of 23-Cl**.** A solution of $PhICl_2$ (29 mg, 105 μmol) in 5mL toluene was added dropwise to a stirred suspension of **36** (64 mg, 52 μmol) at 0° C. The red suspension quickly gave way to a deep blue solution, which was stirred for ~30 minutes. All volatiles were removed, and the resultant blue-purple solid was triturated with Et_2O, collected on a sintered glass frit, and dried *in vacuo* to yield 52 mg (93%) of **23**-Cl. ^{1}H and ^{31}P NMR spectra for **23**-Cl matched those reported previously.[80] Elemental analysis calculated (%) for $C_{54}H_{42}NiP3Sb$: C 62.65, H 4.09; found C 62.38, H 4.21.

Synthesis of 37: A solution of TEA (20 μL, 0.15 mmol) and catechol (8 mg, 0.08 mmol) in 1 mL THF was added dropwise to a stirred, purple suspension of **23**-Cl (68 mg, 0.07 mmol) in 5 mL THF. Over the course of two hours, a deep orange-red suspension formed. The resulting mixture was filtered over a plug of celite. The filtrate was concentrated to ca. 1mL, and ca. 10 mL of pentane were added to precipitate the product. The precipitate was filtered and dried *in vacuo* to afford 29 mg (41%) of **37** as an orange-red powder. ^{1}H NMR(399.53 MHz; C_6D_6): δ= 5.74 (pseudo-t, 1H, catechol C*H*), 6.18 (t, 4H, Ph-C*H*, $^{3}J_{H\text{-}H}$ = 7.33 Hz), 6.31 (t, 2H, Ph-C*H*, $^{3}J_{H\text{-}H}$ = 7.32 Hz), 6.40 (pseudo-t, 4H, Ph-C*H*), 6.43-6.54 (m, 6H, Ph-C*H* + catechol C*H*), 6.55-6.64 (m, 5H, Ph-C*H* + *o*-P(Ni)C_6H_4), 6.64-6.78 (m ,11H, Ph-C*H* + catechol C*H*), 6.80-6.94 (m, 4H, Ph-C*H*), 6.95-

7.05 (m, 3H, *o*-P (Ni)C_6H_4 + *o*-P (Sb)C_6H_4), 7.19 (pseudo-t, 4H, *o*-P (Sb)C_6H_4), 8.37 (d, 2H, *o*-P (Sb)C_6H_4, $^3J_{H\text{-}H}$ = 7.32 Hz). $^{13}C\{^1H\}$ NMR (100.45 MHz; $CDCl_3$): δ = 112.36 (s, catechol *C*H), 113.50 (s, catechol *C*H), 117.72 (s, catechol *C*H), 119.09 (s, catechol *C*H), 126.61 (s), 126.88 (s), 128.32 (m), 128.48 (s), 128.79 (br. m), 129.19 (br. m), 130.18 (s), 131.08 (s), 131.35 (s), 132.21 (m), 133.31 (m), 133.51 (m), 133.88 (s), 134.40 (s), 134.63 (m), 135.51 (m), 136.58 (m), 138.41 (m). Some resonances are obscured by the C_6D_6 *C*D peak. $^{31}P\{^1H\}$ NMR (161.73MHz; C_7D_8): δ = -52.87 (t, 1P, *ortho*-metalated arm, $^2J_{P\text{-}P}$ = 139.20 Hz), 60.31 (d, 2P, $^2J_{P\text{-}P}$ = 139.20 Hz). Elemental analysis calculated (%) for $C_{60}H_{46}NiO_2P_3Sb$: C 67.20, H 4.32; found C 66.90, H 4.35.

Synthesis of 38. CyNC (20 μL, 160 μmol) was added via syringe to a stirred, purple suspension of **23**-Cl (163 mg, 160 μmol) in 5 mL THF to give a yellow-brown suspension, which was stirred for 15 min. A solution of TEA (48 μL, 346 μmol) and catechol (18 mg, 170 μmol) in 1 mL THF was added dropwise to the CyNC/**23**-Cl suspension, resulting in the rapid formation of a cloudy orange-red solution. After stirring for 2 h, the reaction mixture was filtered over a plug of Celite and concentrated to ca. 1 mL. The product was precipitated by addition of ca. 10 mL pentane, filtered, and dried *in vacuo* to yield **38** as an orange powder (168 mg, 90%). ^1H NMR (399.59 MHz; $CDCl_3$): δ = 1.02 (br, 4H, Cy-CH_2), 1.31 (br, 6H, Cy-CH_2), 3.09 (br, 1H, Cy-C*H*), 5.28 (d, 1H, catechol C*H*, $^3J_{H\text{-}H}$ = 7.69 Hz), 6.10 (pseudo-t, 1H, catechol C*H*), 6.26 (pseudo-t, 1H, catechol C*H*), 6.60-6.68 (m, 6H, *o*-P(Sb)C_6H_4 + Ph-C*H*), 6.70-6,84 (m, 18H, *o*-P(Sb)C_6H_4 + Ph-C*H*), 6.84-6.93 (m, 5H, *o*-P(Sb)C_6H_4 + Ph-C*H* + catechol C*H*), 6.96-7.10 (m, 10H, *o*-P(Sb)C_6H_4 + Ph-C*H*), 7.48 (pseudo-t, 1H, *o*-P(Sb)C_6H_4), 8.16 (d, 2H, *o*-P(Sb)C_6H_4, $^3J_{H\text{-}H}$ = 7.32 Hz), 9.18 (d,

1H, *o*-P(Sb)C_6H_4, $^3J_{H\text{-}H}$ = 7.32 Hz). $^{13}C\{^1H\}$ NMR (100.45 MHz; $CDCl_3$): δ = 23.32 (s, Cy-*C*H_2), 24.99 (s, Cy-*C*H_2), 32.09 (s, Cy-*C*H_2), 55.02 (s, Cy-*C*H), 112.92 (s, catechol *C*H), 113.72 (s, catechol *C*H), 114.76 (s, catechol *C*H), 115.93 (s, catechol *C*H), 126.83 (s), 127.42 (t, *J* = 4.52 Hz), 127.54 (t, *J* = 4.62 Hz), 127.99 (s), 128.13 (d, *J* = 5.32 Hz), 128.50 (s), 128.59 (s), 128.69 (s), 129.58 (s), 130.08 (s), 131.14 (t, *J* = 12.96 Hz), 132.19 (d, *J* = 9.95 Hz), 133.20 (t, *J* = 13.68 Hz), 133.63 (t, 5.32 Hz), 134.16 (d, *J* = 23.61 Hz), 134.53 (t, *J* = 6.12 Hz), 135.51 (s), 136.24 (m), 137.59 (t, *J* = 21.30 Hz), 138.19 (t, *J* = 6.13 Hz), 138.47 (t, *J* = 6.13 Hz). $^{31}P\{^1H\}$ NMR(161.73MHz, $CDCl_3$): δ = 39.68 (t, 1P, $^2J_{P\text{-}P}$ = 83.89 Hz), 68.91 (d, 2P, $^2J_{P\text{-}P}$ = 83.89 Hz) Elemental analysis calculated (%) for $C_{67}H_{57}NNiO_2P_3Sb\bullet 2C_6H_6$: C 70.93, H 5.20; N 1.05; found C 70.96, H 5.30, N 1.10.

Theoretical Calculations. Density functional theory (DFT) calculations (full geometry optimization) were carried out on compounds **1**, **2**, and **4**, starting from the crystal structure geometries with Gaussian09[133] program (mPW1PW91[95] functional, with the basis sets 6-31G(d)[195] for H, C, N, O, P, Cl; cc-pVTZ[196] for Ni; cc-pVTZ[197] with Stuttgart[198] relativistic small core ECP for Sb). Despite extensive efforts, a global minimum could not be obtained in the optimization of compound **2**; the two remaining virtual frequencies correspond to very low energy movements of the phenyl groups. The optimized structures, which are in excellent agreement with the solid-state structures, were subjected to a NBO analysis.[199] The resulting Natural Bond Orbitals(NBOs) and Natural Localized Molecular Orbitals (NLMOs) were visualized and plotted in Jimp 2 program.[99]

Crystallography. Single crystals of **36** suitable for X-ray diffraction were obtained by slow diffusion of Et_2O into a toluene solution of the compound at -20°C. Single crystals

of **37** suitable for X-ray diffraction were obtained by slow diffusion of Et_2O into a benzene solution of the compound at room temperature. Single crystals of **38** suitable for X-ray diffraction were obtained by slow diffusion of pentane into a benzene solution of the compound at room temperature. Crystal data, details of data collection, and structure refinement parameters for compounds **36**, **37**, and **38** are compiled in Table 21. The crystallographic measurements were performed at 110(2) K using a Bruker APEX-II CCD area detector diffractometer, with a graphite-monochromated Mo-Kα radiation (λ = 0.71069 Å). In each case, a specimen of suitable size and quality was selected and mounted onto a nylon loop. The semi-empirical method SADABS[100] was applied for absorption correction. The structure was solved by direct methods and refined by the full-matrix least-square technique against F^2 with the anisotropic temperature parameters for all non-hydrogen atoms. All H atoms were geometrically placed and refined in riding model approximation. Data reduction and further calculations were performed using the Bruker SAINT+[101] and SHELXTL NT[102] program packages.

Table 21. Crystal data, data collections, and structure refinements for **36**, **37**, and **38**.

	36	**37**	**38**
Formula	$C_{72}H_{57}NiP_4Sb$	$C_{62}H_{55}NiO_2P_3Sb$	$C_{64}H54NNiO_2P_3Sb$
	$\bullet 1.5(C_4H_{10}O)$	$\bullet (C_6H_6)$	$\bullet 4(C_6H_6)$
Formula Weight	1337.70	1183.54	1454.88
Crystal Size (mm)	0.13 x 0.11 x 0.03	0.34 x 0.25 x 0.17	0.31 x 0.21 x 0.13
Crystal System	Triclinic	Triclinic	Monoclinic
Space Group	P-1	P-1	P2(1)/n
a (Å)	12.674(4)	10.903(2)	21.226(3)
b (Å)	14.112(4)	14.127(3)	14.225(2)
c (Å)	19.207(6)	19.629(4)	25.500(4)
α (°)	96.850(4)	104.671(2)	90
β (°)	95.575(4)	96.648(3)	114.248(2)
γ (°)	109.285(3)	107.980(2)	90
V ($Å^3$)	3185.0(17)	2719.4(10)	7020.3(17)
Z	2	2	4
ρ_{calc} (g/cm^3)	1.395	1.445	1.377
μ (mm^{-1})	0.868	0.979	0.773
F(000)	1382	1218	3012
T (K)	110(2)	110(2)	110(2)
Scan mode	ω, φ	ω, φ	ω, φ
hkl Range	-16 → 16	-14 → 14	-27 → 27
	-18 → 18	-18 → 17	-18 → 18
	0 → 25	0 → 25	-33 → 33
Reflections collected	37325	32320	81959
Unique reflections [Rint]	14713 [0.1112]	12533 [0.0743]	16262 [0.0509]
Reflns. used for refinement	12232	12533	16262
Refined parameters	794	631	865
GooF	1.017	1.015	1.018
R1[a], *w*R2[b] (all data)	0.0977, 0.1503	0.0483, 0.1194	0.0364, 0.0692
ρ_{fin} (max., min.) (eA^{-3})	1.451, -1.847	0.931, -0.602	0.578, -0.319

[a]$R1 = \sum||F_o| - |F_c||/\sum|F_o|$. [b] $wR2\ ([w(F_o^2 - F_c^2)^2]/[\sum w(F_o^2)^2])^{1/2}$; $w = 1/[\sigma^2(F_o^2) + (ap)^2 + bp]$; $p = (F_o^2 + 2F_c^2)/3$ with $a = 0.0650$ for **36**, 0.0627 for **37**, and 0.0233 for **38**; and $b = 0.0000$ for **36**, 0.0000 for **37**, and 4.6978 for **38**.

6. COORDINATION NON-INNOCENCE OF A PLATINUM STIBORANYL COMPLEX[4]

6.1 Introduction

The term of ligand non-innocence is used when a ligand participates in a redox process that would otherwise be expected to occur at the metal center.[200-203] Such ligands are of both fundamental and applied interest, due to their ability to profoundly impact the reactivity of their coordinated metal centers.[204, 205] Prototypical examples of systems exhibiting this behavior include metal dithiolene complexes, which undergo successive ligand based reductions.[206-208] Recent results in the coordination chemistry of heavy main group ligands suggest that a ligand can also become non-innocent by participating in anion rather than electron exchange reactions.[30, 42, 49, 149, 209] Such behavior, which we coin coordination non-innocence, has hitherto been demonstrated principally with antimony ligands in the trivalent state. Notable exceptions, however are the gold-stibonium complex and the mercury-stibonium complex, which can coordinate both anionic and neutral Lewis bases at their antimony centers.[31-33] In this chapter we now show that the concept of coordination non-innocence can be applied to stiboranyl ($R_4Sb•$) ligands and exploited for the design of a new anion-responsive platform.[210-213] As documented in this report, this new platform operates through a fluoride-induced, reversible switching of a stiboranyl X-ligand (one electron donor) into a stiborane Z-ligand (σ-accepting ligand).[17]

---

[4] Reprinted in part with permission from, "Anion-Controlled Switching of an X Ligand into a Z Ligand: Coordination Non-innocence of a Stiboranyl Ligand"; Ke, I.-S.; Jones, J. S.; Gabbaï, F. P. *Angew. Chem. Int. Ed.* **2014**, *53*, 2633, Copyright 2014 by Wiley-VCH Verlag GmbH & Co.

6.2 Oxidation and subsequent bond metathesis of a divalent platinum stibine complex

Compounds **39** and **41** were previously described and characterized by Dr. Iou-Sheng Ke in a dissertation.[214] All structural and spectroscopic data for these compounds cited herein are used in the context of comparison with original compounds described in this chapter. Compound **39** was reported to undergo oxidation by *o*-chloranil and undergo subsequent platinum-mediated Sb-C insertion to give compound **41** (Figure 77).

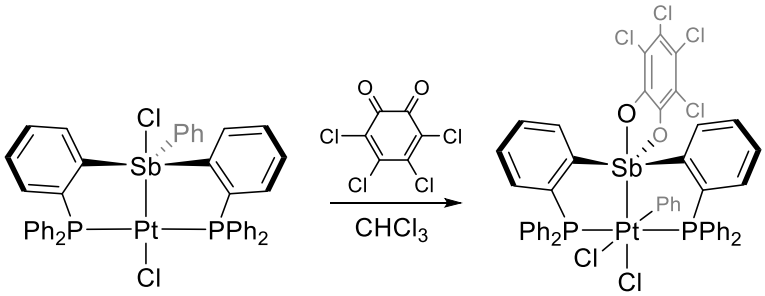

Figure 77. Synthesis of **41** from **39** described by Ke.[214]

Qualitative monitoring of the above reaction found that it proceeds through two phases. Upon initial addition of the *o*-chloranil solution to a solution of **39**, a deep red solution is formed. This is followed by precipitation of **41** as a yellow solid. Intrigued by the place of the initial phase of the reaction in the eventual formation of the Sb-C bond insertion product, we sought to spectroscopically monitor the progress of the reaction. To this end, a CH_2Cl_2 solution of *o*-chloranil was added to a suspension of **39** in CH_2Cl_2. The reaction

mixture was stirred until a homogeneous, deep red solution was formed, which was then stored at -20°C. The $^{31}P\{^{1}H\}$ NMR spectrum of this reaction mixture features a single peak at 32.44 ppm, flanked by ^{195}Pt satellites ($J_{Pt\text{-}P}$ = 3276 Hz). The observed $J_{Pt\text{-}P}$ value is substantially larger than that observed for compound **41** ($^{1}J_{Pt\text{-}P}$ = 2192 Hz), which suggested that the platinum center in the intermediate had not yet undergone oxidation.

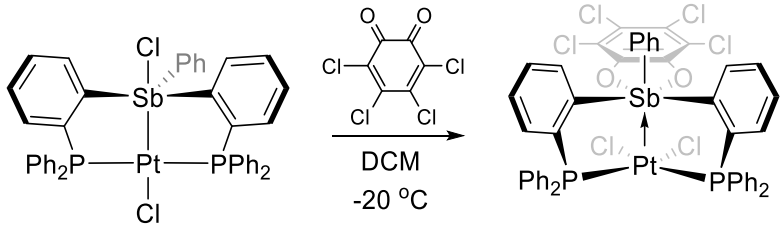

39 **40**

Figure 78 Reaction of **39** with *o*-chloranil at low temperature.

Layering the red solution with pentane at -40 °C afforded single crystals of the initial reaction product (**40**), which were subjected to an X-ray diffraction study (Figure 79). The solid state structure of **40** revealed that the antimony center had been oxidized by *o*-chloranil, forming a neutral tetrachlorocatecholate stiborane unit. The antimony center adopts a square pyramidal geometry, as indicated by a calculated τ value of 0.08. The open face of the stiborane unit is positioned over the tethered, divalent platinum center, with the Sb-Pt separation of 2.9868(7) Å being considerably longer than those found in both **39** (2.5380(8) Å) and **40** (2.5906(5) Å), and exceeding the sum of antimony and platinum covalent radii (2.75 Å).[215] The platinum center retains a square planar geometry, with the

chloride ligand previously coordinated at antimony returning to the platinum center. Taken together, these structural and spectroscopic observations suggest that the square pyramidal stiborane unit[216, 217] in **40** acts as Z-type ligand towards the proximal divalent platinum center.

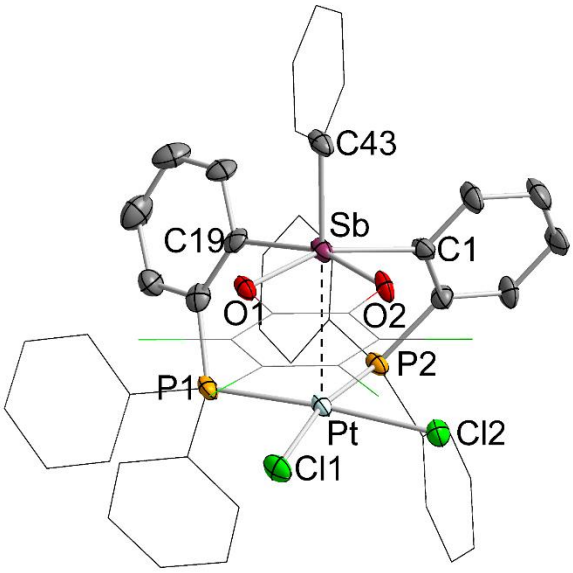

Figure 79 Crystal structure of compound **40**. Thermal ellipsoids are drawn at the 50% probability level. Selected phenyl groups and the *o*-chloranil group are drawn in wireframe. Hydrogen atoms and solvent residues are omitted for clarity. Selected bond lengths (Å) and angles (°): Sb-Pt 2.9868(7), Sb-O1 2.074(4), Sb-O2 2.058(4), Sb-C43 2.128(6), P1-Pt-Cl2 175.91(6), P2-Pt-Cl1 168.92(6), C43-Sb-Pt 173.63(18), O1-Sb-C1 156.9(2), O2-Sb-C19 162.6(2).

When returned to room temperature, solutions of **40** quickly convert to **41.** While the mechanism of this conversion remains unknown, it likely involves a series of isomerizations and/or pseudorotations at both the antimonyn and platinum centers based on the observed structure of **40**.

6.3 Fluoride binding studies

While from a coordination chemistry standpoint compound **41** is described as a stiboranyl ($R_4Sb•$) complex of platinum, it may also be viewed as a metallostiborane. In light of electron-deficient stiboranes having been shown in recent years to possess sufficient Lewis acidity to extract fluoride anions from aqueous media,[48, 218] we sought to investigate the reactivity of **41** towards fluoride anions. Dr. Iou-Sheng Ke made inroads towards this goal, performing a fluoride titration of **41** in $CHCl_3$ using TBAF (Figure 80).[214] Based on $^{31}P\{^1H\}$ NMR spectra, Ke concluded that the first equivalent of fluoride binds at antimony in a fluoride-for-chloride exchange to form compound **42**-F. While **42**-F was unable to be isolated, Ke assigned a Sb(μ^2-Cl)Pt structure to this intermediate product on the basis of DFT calculations. Ke then postulated on the basis of $^{31}P\{^1H\}$ and $^{19}F\{^1H\}$ NMR that addition of a second equivalent of fluoride replaces the bridging chloride anion in a second chloride-for-fluoride exchange to form compound **43**-F. A crystal structure of **43**-F was purported to confirm this assignment.

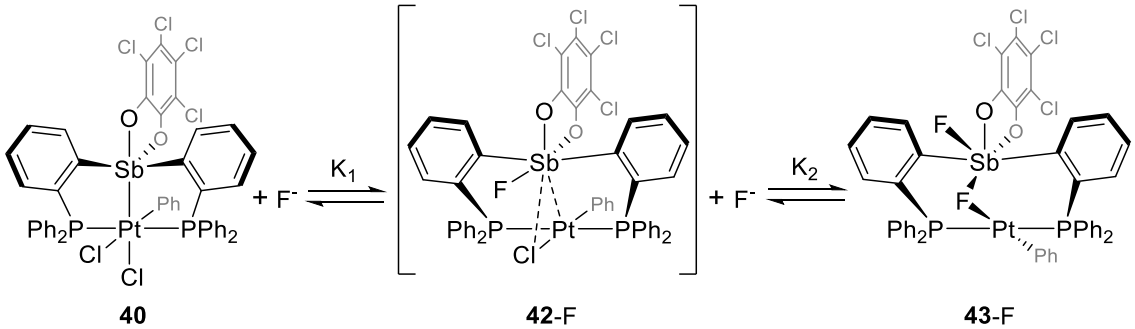

Figure 80. Sequential fluoride binding to **41** proposed by Ke.[214]

With the above results in mind, the investigation was renewed with the intention to determine whether **41** could bind fluoride under aqueous/organic biphasic conditions. Layering a $CHCl_3$ solution of **41** with a solution of KF (10-20 eq.) in unbuffered water (Millipore purified, pH 5) and agitating the resulting biphasic mixture for approximately 20 minutes cleanly afforded a compound characterized by a $^{31}P\{^1H\}$ NMR spectrum in $CDCl_3$ consisting of a singlet at 26.29 ppm flanked by ^{195}Pt satellites ($^1J_{Pt\text{-}P}$ =3276 Hz) (Figure 81). While the observed $^{31}P\{^1H\}$ NMR spectrum matched that reported for **43**-F, only one resonance at -97.6 ppm was observed in the $^{19}F\{^1H\}$ spectrum in contrast to the two resonances reported by Ke. In an effort to reconcile the previous assignment with the newly obtained spectral data, a new refinement of the previously reported crystal structure for **43**-F, along with a new data collection of a solvate isomer was performed. On the basis of two short contacts (1.88 Å) between the atom bridging the antimony and platinum atoms and the antimony-bound fluoride, the bridging group was reassigned as a hydroxide anion (Figure 82). This structural feature of **43**-OH is furthermore consistent with the presence of only one resonance in the recorded ^{19}F NMR spectrum.

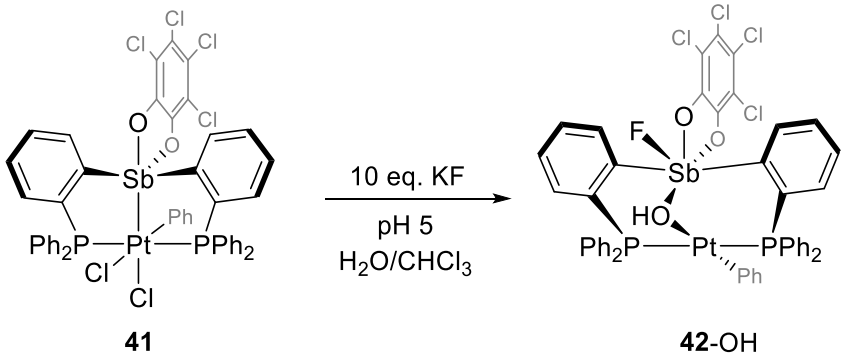

Figure 81 Treatment of compound **41** with KF in unbuffered water under biphasic conditions.

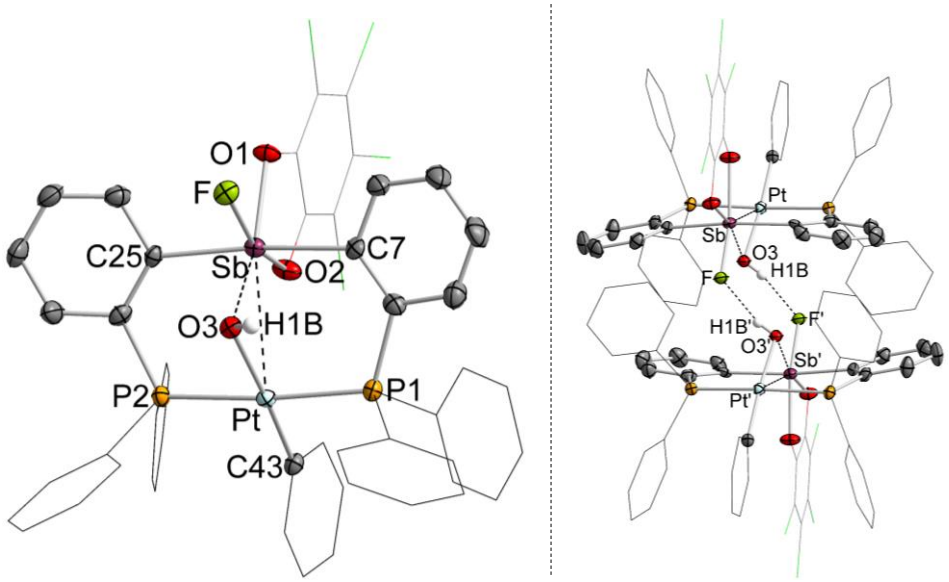

Figure 82. Crystal structure of **43**-OH (left) and its extended structure (right) , showing hydrogen bonding between the hydroxide and fluoride groups. Thermal ellipsoids are drawn at the 50% probability level. Selected phenyl groups are drawn in wireframe. Hydrogen atoms and solvents are omitted for clarity. Selected bond lengths (Å) and angles (°): Sb-Pt 3.0428(7), Sb-O1 2.046(3), Sb-O2 2.095(3), Sb-O3 2.087(3), Sb-F1 1.979(3), Pt-O3 2.125(3), P1-Pt-P2 174.25(4), O3-Pt-C43 176.20(17), O1-Sb-O3 162.78(14), O2-Sb-F1 158.51(13), C7-Sb-C25 172.46(18).

The geometric parameters for **43**-OH are very similar to those previously reported for **43**-F. As a consequence of this substitution, the Sb-Pt separation greatly lengthens from 2.5906(5) Å in **41** to 3.0428(7) Å in **43**-OH. The Sb-Pt distance is similar to that found in **40** (2.9868(7) Å) suggesting that the covalent Sb-Pt bond has been effectively cleaved by anion coordination at the antimony center. The antimony center adopts an octahedral geometry, whereas the platinum center attains a square planar geometry typical for the divalent state. The hydroxide ligand bridges the antimony and platinum centers in an almost symmetric fashion, with the Sb-OH distance of 2.087(3) Å and the Pt-OH distance

of 2.125(3) Å being only slightly longer than those found in monomeric [(18-crown-6)K][(C_6F_5O)$SbCl_4$(OH)][219] (1.924(3) Å) and [(*R*,*R*)-Me-Duphos)Pt(Ph)(OH)][220] (2.052(6) - 2.058(7) Å).

Having demonstrated that **41** undergoes partial hydrolysis in addition to chloride-for-fluoride exchange to form **43**-OH, we next reinvestigated the intermediates in this process. To this end, a $CDCl_3$ solution of **41** was layered with an aqueous solution of KF, and the reaction progress at various mixing times was monitored *via* $^{31}P\{^1H\}$ NMR (Figure 83). Upon initial agitation of the aqueous and organic phases (5 s.), an orange color rapidly developed in the organic phase. Inspection of the $^{31}P\{^1H\}$ NMR spectrum at this point revealed the presence of two distinct intermediates, characterized by their respective $^{31}P\{^1H\}$ shifts of 39.04 and 35.50 ppm flanked by ^{195}Pt satellites with $^1J_{Pt\text{-}P}$ values of 2702 and 2855 Hz, respectively. As the mixing of the two layers progresses, these two intermediates gradually disappear, cleanly forming compound **43**-OH.

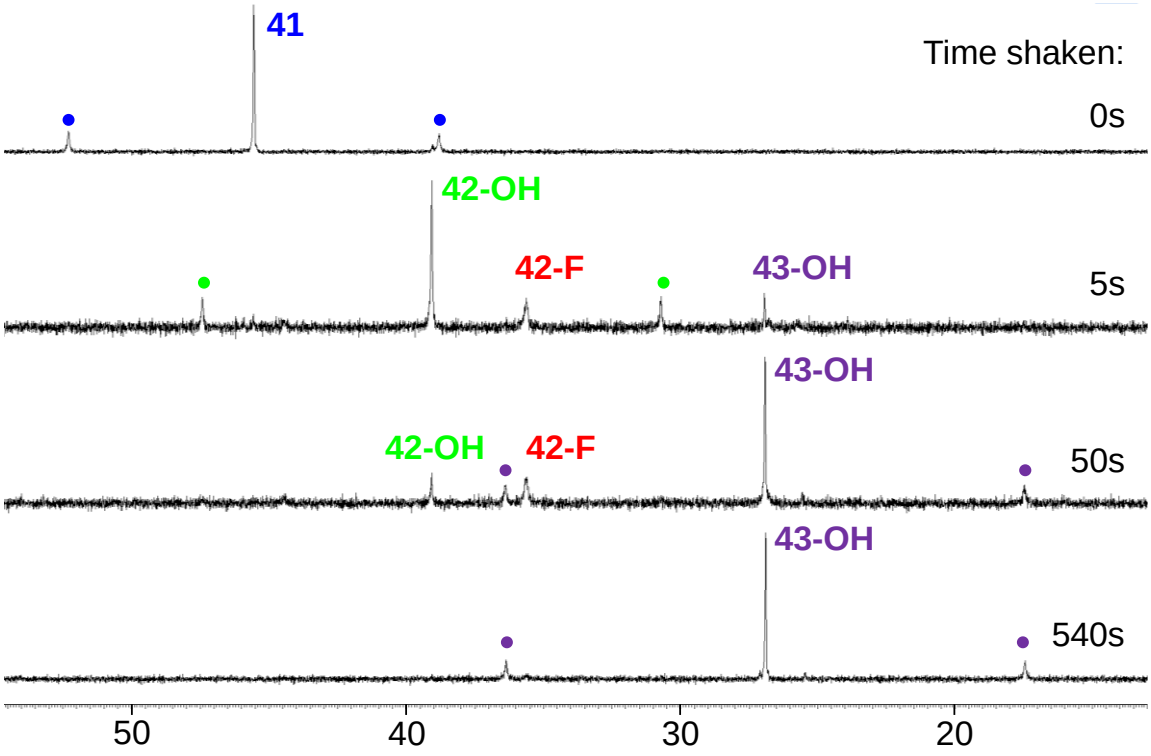

Figure 83 $^{31}P\{^{1}H\}$ NMR spectra of the biphasic reaction of **41** in $CDCl_3$ with aqueous (Millipore purified, pH 5) KF at progressive mixing times.

Layering a $CDCl_3$ solution of **41** with only unbuffered water and mixing the two phases resulted in a mixture of unreacted **41** and **42**-OH, establishing **42**-OH as a hydrolysis product. Indeed, when a $CDCl_3$ solution of **41** is layered with pH 9 borate buffered water, rapid and full conversion to **42**-OH is achieved (Figure 84). With **42**-OH identified as one of the intermediates involved in the transition from **41** to **43**-OH, we next sought to isolate the second observed intermediate.

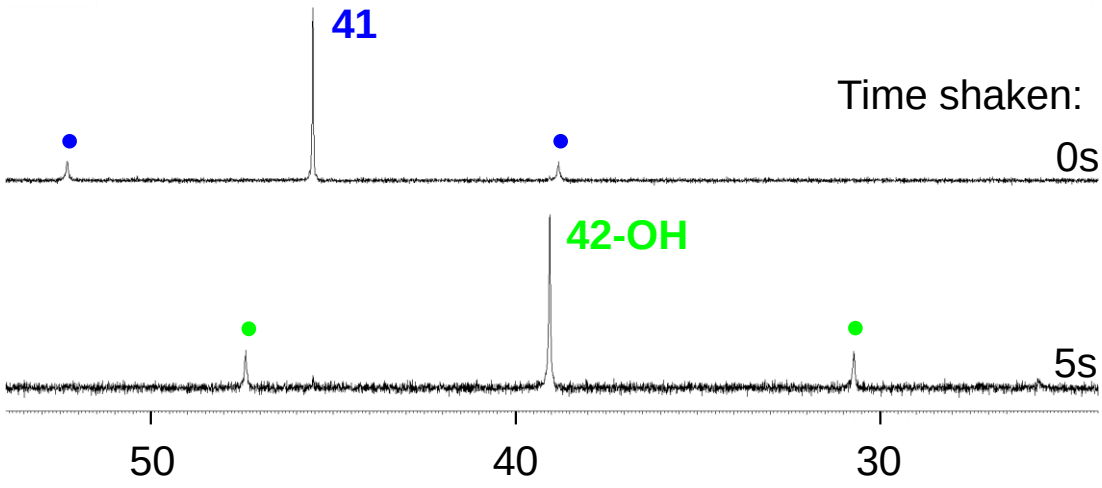

Figure 84 $^{31}P\{^{1}H\}$ NMR spectra of the biphasic reaction of **41** in $CDCl_3$ with water (borate buffer, pH 9) at progressive mixing times.

In order to prevent hydrolysis, **41** was allowed to react under biphasic conditions with excess KF in an aqueous 0.1 M HCl solution (Figure 85). Mixing of the two phases cleanly and rapidly afforded an orange solution. Concomitant with the observed color change, a new resonance appeared at -77.1 ppm in the ^{19}F NMR spectrum of the reaction mixture. The $^{31}P\{^{1}H\}$ NMR spectrum consisting of a singlet at 35.50 ppm flanked by ^{195}Pt satellites with ($^{1}J_{Pt\text{-}P}$ = 2855 Hz), consistent with the second intermediate observed in the formation of **43**-OH. Taken together these spectral data support the identity of the second intermediate as **42**-F, in agreement with the intermediate previously observed by Ke.[214] The lack of $^{3}J_{P\text{-}F}$ coupling observed in both **42**-F and **43**-OH is precedented by similar Sb-Pt and Sb-Pt complexes,[38, 209] and may be rationalized by the Karplus equation, in which the ^{3}J coupling between two nuclei is most diminished when their dihedral angle approaches 90°.[221, 222] The $^{195}Pt\{^{1}H\}$ resonance of **42**-F at -3714 ppm is shifted noticeably

more downfield than that reported for *trans*-[(*p*-$MeOC_6H_4$)PtCl(PPh_3)$_2$] (δ(^{195}Pt) = -4365 ppm],[223, 224] consistent with transfer of electron density from platinum to antimony. This downfield shift is also consistent with the transfer of electron density from platinum to antimony, a phenomenon analogous to that proposed for a series of complexes of the general formula NCN(X)Pt→SO_2 (NCN = 2,6-[(Me_2N)CH_2]$_2$$C_6H_4$ and X =halide).[225] Finally, we note that the conversion of **41** into **42**-F can be reversed by addition of a fluoride scavenger such as $AlCl_3$ to the aqueous layer.

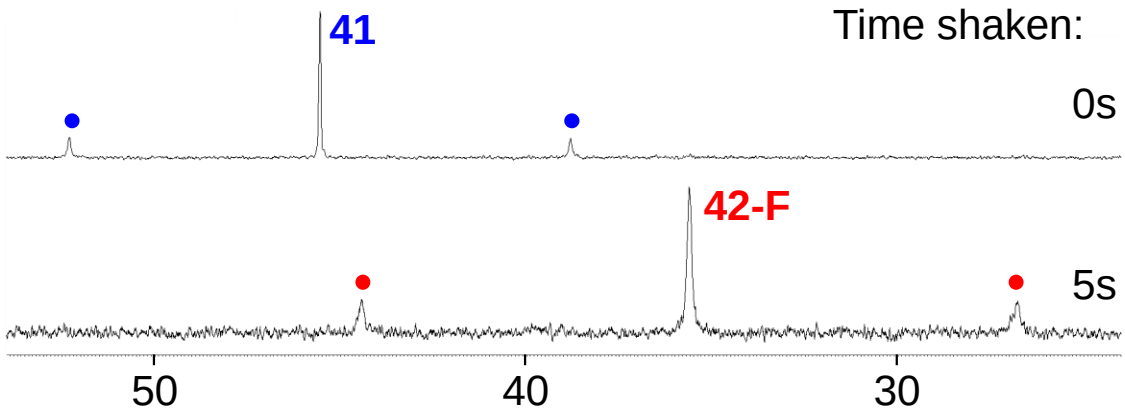

Figure 85 ^{31}P{^{1}H} NMR spectra of the biphasic reaction of **41** in $CDCl_3$ with KF (10 eq.) in 0.1 M HCl at progressive mixing times.

Final confirmation of the structure of **42**-F was obtained from a single crystal X-ray diffraction study (Figure 86). Although only one platinum-bound chloride ligand is exchanged for an antimony-bound fluoride, this substitution results in a large increase in the Sb-Pt separation from 2.5906(5) Å in **41** to 3.0868(11) Å in **42**-F. As in compound **43**-F, the platinum center adopts a square planar geometry characteristic of the divalent state,

whereas the antimony center adopts a distorted square pyramidal geometry ($\tau = 0.12$). In contrast to **43**-OH, which features a somewhat symmetric hydroxide bridge, the chloride ligand of **42**-F can be considered primarily platinum-bound, as indicated by the short (2.432(3) Å) Pt-Cl distance relative to the Sb-Cl separation (2.831(3) Å). Indeed, while the observed Pt-Cl distance is quite similar to that found for *trans*-$(Ph_3P)_2Pt(Ph)Cl$ (2.408(5) Å),[226] the observed Sb-Cl distance is considerably longer than those found in $[Ph_2SbCl_2((OPPh_2)_2N)]$ (2.452(1) – 2.420(1) Å).[227] Thus while **43**-OH may be described as a zwitterionic antimonate, **42**-F is best described as a platinum stiborane complex, in which an acidic face of the stiborane is positioned above a divalent platinum center.

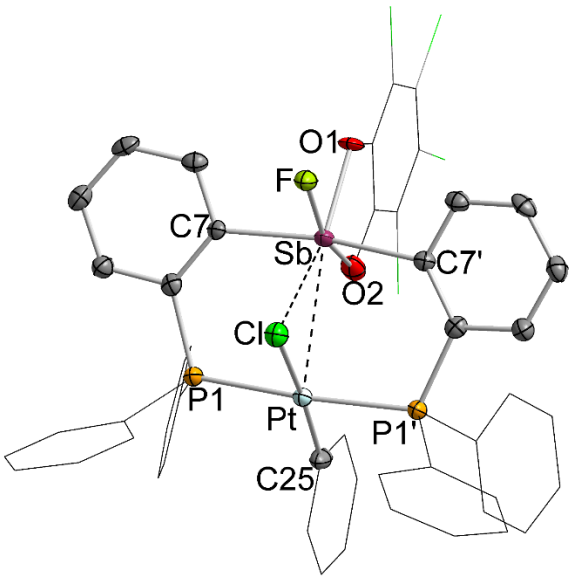

Figure 86 Crystal structure of **42**-F. Thermal ellipsoids are drawn at the 50% probability level. Selected phenyl groups are drawn in wireframe. Hydrogen atoms are omitted for clarity. Selected bond lengths (Å) and angles (°): Sb-Pt 3.0868(11), Sb-F 1.957(7), Sb-Cl 2.831(3), Pt-Cl 2.432(3), Sb-O1 2.031(8), Sb-O2 2.093(10), P1-Pt-P1' 172.21(11), Cl-Pt-C25 173.7(4), Pt-Sb-O1 154.8(3), Cl-Sb-O1 156.9(3), F-Sb-O2 160.9(3), C7-Sb-C7' 168.2(4), Sb-Cl-Pt 71.35(9), O1-Sb-O2 80.4(4), F-Sb-Cl 76.5(2).

Although the final hydrolysis/anion exchange product of the reaction of **41** with aqueous KF is colorless, the intermediate species **42**-OH and **42**-F are both strongly colored. Intrigued by the possibility of using this anion responsive platform in the context of colorimetric sensing, we next took initial steps towards investigating the use of **41** as a fluoride sensor. Unfortunately, even using an acidified aqueous phase (pH = 1), the binding of hydroxide is competitive with the binding of fluoride at concentrations below 100 ppm.

6.4 Computational studies

In order to investigate the changing nature of the Sb-Pt bonds in the series of compounds presented, compounds **41**, **42**-F, and **43**-OH were subjected to optimization by DFT methods starting from their observed crystal structure geometries. Inspection of the calculated frontier orbitals find that in each case, the LUMO bears significant antimony character (Figure 87). The contribution of the antimony center to the LUMO increases across the series. This trend, while somewhat counterintuitive, can be rationalized by a "spillover" of electron density from the antimony center to its substituents.[128] In each case, the HOMO is mostly localized to the *o*-chloranil π system.

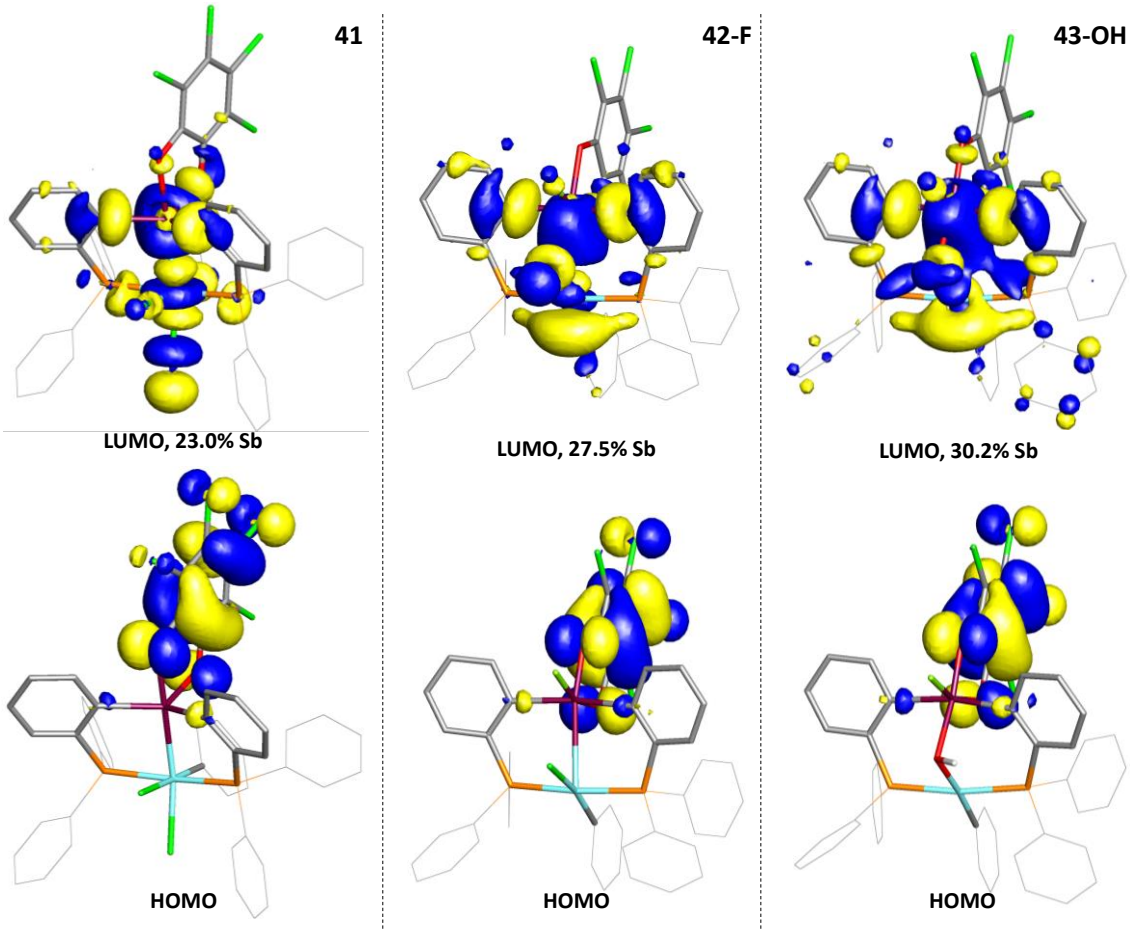

Figure 87. HOMO and LUMO orbitals (isodensity value = 0.05) of compounds **41**, **42**-F, and **43**-OH. Selected hydrogen atoms are omitted and selected phenyl groups are drawn in wireframe for clarity.

All three compounds were next submitted to NBO analysis at their DFT-optimized geometries. In the case of **40**, finds a NLMO corresponding to the Sb-Pt bond (Sb 32.5% / Pt 37.9%), consistent with the formulation of the antimony ligand as a covalently bound stiboranyl (Figure 88). In compound **42**, however NBO analysis finds a series of d(Pt)→σ*(Sb) and (p(Cl)→σ*(Sb)) donor-acceptor interactions, whose combined delocalization energy equals 59.9 kcal/mol and 26.2 kcal/mol, respectively. The change

in nature of the Sb-Pt interaction, along with the relatively modest delocalization energy associated with the d(Pt)→σ*(Sb) interactions suggests that fluoride coordination to the antimony center severs the covalent Sb-Pt bond found in **41** and transforms the antimony ligand into a Z-type stiborane.

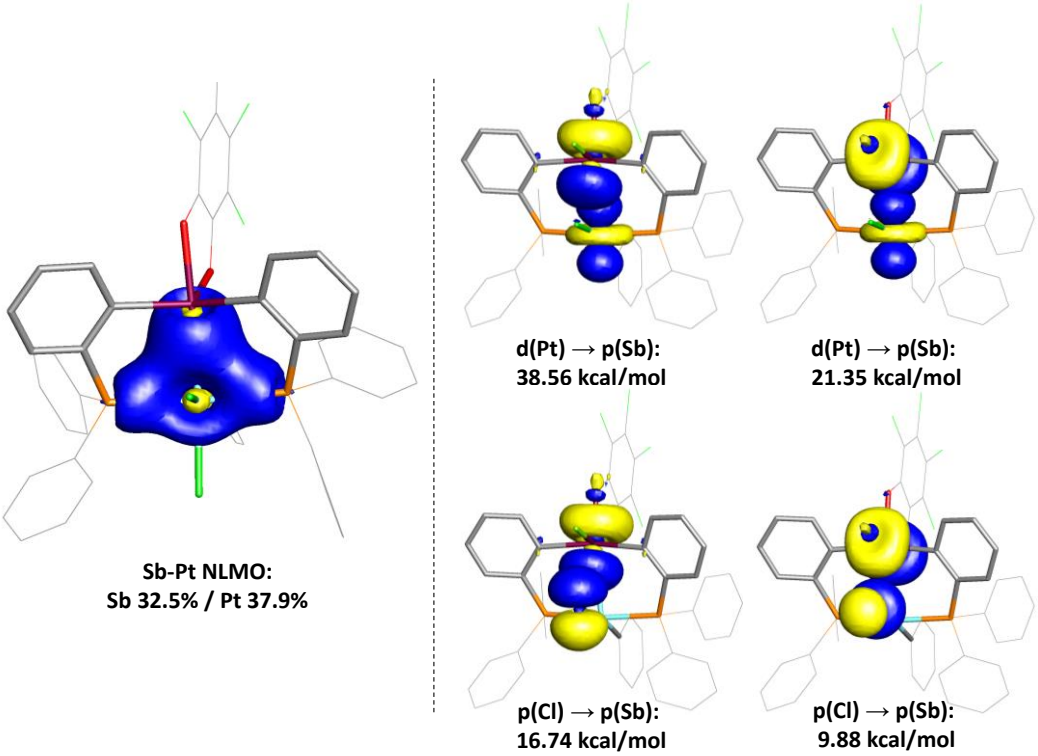

Figure 88. NBO plots for the Sb-Pt interactions in **41** and **42**-F. (left) NLMO plot of the Sb-Pt bond in **41** (isodensity value = 0.05). (right) Major d(Pt)→p(Sb) and p(Cl)→p(Sb) donor-acceptor interactions in **42**-F obtained from NBO analysis (isodensity value = 0.05). Hydrogen atoms are omitted, and selected groups are drawn in wireframe for clarity.

Finally, NBO analysis of compound **43**-OH finds that similar to **42**-F, the antimony center in the stiborane moiety engages the platinum center and the bridging hydroxide ligand in

a series of donor-acceptor interactions (Figure 89). The sum of the combined delocalization energies for the d(Pt)→σ*(Sb) and (p(O)→σ*(Sb)) is equal to 23.2 and 73.9 kcal/mol, respectively. Compared with **42**-F, the strength of the Pt→Sb interaction is diminished while the strength of the interaction with the bridging ligand is enhanced, in line with structural metrics suggesting that the hydroxide anion in **43**-OH bridges in a more symmetric fashion than the chloride anion in **42**-F.

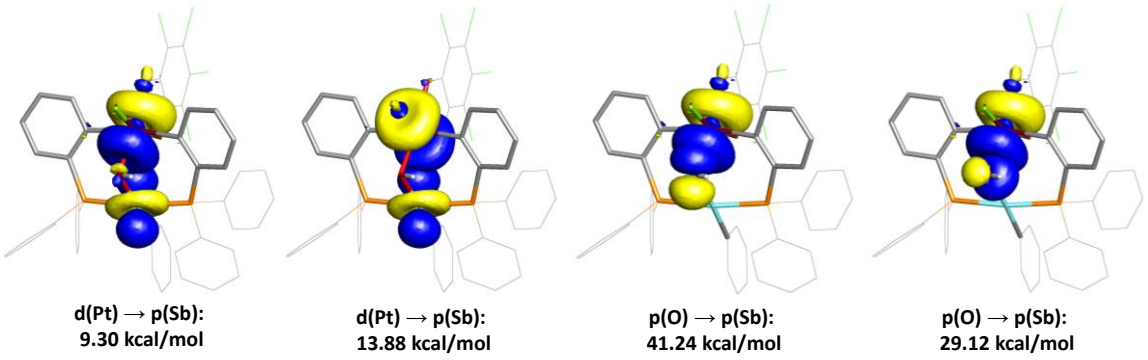

Figure 89. Major d(Pt)→p(Sb) and p(O)→p(Sb) donor-acceptor interactions in **43**-OH obtained from NBO analysis (isodensity value = 0.05). Selected hydrogen atoms are omitted, and selected groups are drawn in wireframe for clarity.

In an effort to investigate the origin of the colorimetric response of **41** to fluoride, both **41** and **42**-F were subjected to TD-DFT calculations. UV/Vis monitoring of the reaction in CH_2Cl_2 found that the formation of **42**-F is associated with the appearance of low-energy bands which extend into the visible range of the spectrum (Figure 90). TD-DFT calculations found that these bands are associated with a series of low-energy transitions. The three low-energy transitions of highest intensity (labeled as **A**-**C**) share the common

feature of having the LUMO as the sole accepting orbital. As the LUMOs of both **41** and **42**-F features significant antimony character, we postulate that the binding of fluoride and concomitant cleavage of the covalent Sb-Pt bond significantly perturbs the electronic transitions in **42**-F.

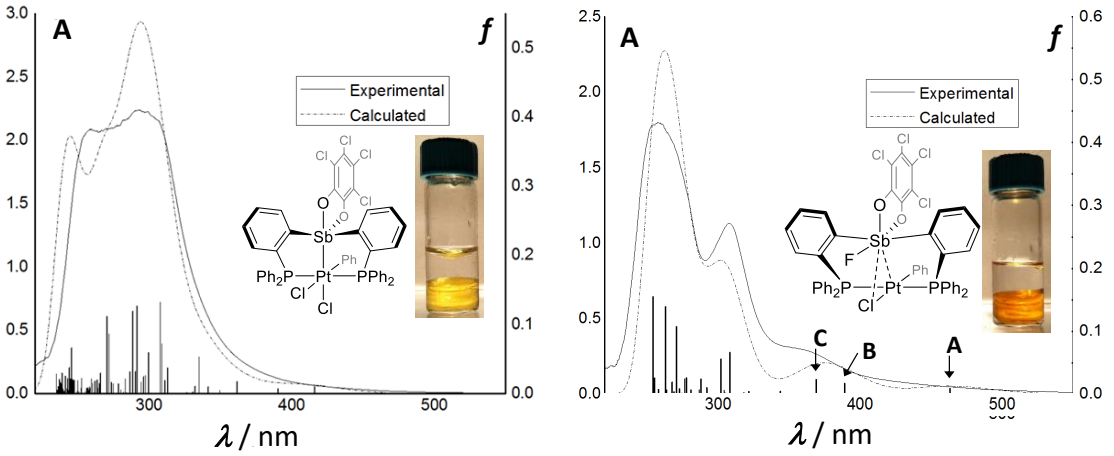

Figure 90. Experimental and calculated (TD-DFT) UV–visible spectra of **41** (left) and **42**-F (right) with the computed excitations shown as thin lines with heights proportional to the calculated oscillator strengths. Inset photos show the biphasic reaction mixtures before (**41**) and after (**42**-F) agitating the two phases.

6.5 Conclusions

In conclusion, we report a new fluoride anion-responsive platform whose properties originate from the coordination non-innocence of an antimony ligand. The series of compounds presented highlight the ability of antimony to act as a dynamic redox partner in conjunction with late transition metal centers. We report the isolation of an intermediate (**40**) in the two-electron oxidation of **39** by *o*-chloranil and subsequent platinum-mediated antimony-carbon bond insertion to give **41**.

The covalent Pt-Sb bond in compound **41** can be cleaved to form the Sb (μ_2-OH) Pt species **43**-OH, which was previously misidentified as a fluoride-bridged species. Two new Sb (μ_2-Cl) Pt (**42**-F and **42**-OH) intermediates in this transformation were found and isolated. NBO analysis suggests that anion coordination at antimony results triggers a reversible switch of a stiboranyl X-ligand (one electron donor) into a stiborane Z-ligand (σ-accepting ligand). The strongly colored **42**-F was used to provide a turn-on response for fluoride binding in a proof of concept experiment.

6.6 Experimental details

General Considerations. *Antimony compounds should be handled cautiously.* Compounds **39**[110, 214], **41**[110, 214], and **43**-OH[214] were prepared according to reported procedures. Solvents were dried by passing through an alumina column (n-pentane and CH_2Cl_2) or by reflux under N_2 over Na/K (Et_2O and THF). All other solvents were used as received. *o*-chloranil was purchased from Aldrich and used as received. All air and moisture sensitive manipulations were carried out under an atmosphere of dry N_2 employing either a glove box or standard Schlenk techniques. Ambient temperature NMR spectra were recorded on a Varian Inova 500 FT NMR (499.43 MHz for ^{1}H, 125.58 MHz for ^{13}C) spectrometer or a Varian Unity Inova 400 FT NMR (399.59 MHz for ^{1}H, 100.45 MHz for ^{13}C, 375.99 MHz for ^{19}F, 161.74 MHz for ^{31}P, 85.69 MHz for ^{195}Pt) spectrometer. Chemical shifts (δ) are given in ppm and are referenced against residual solvent signals (^{1}H, ^{13}C) or external BF_3•Et_2O(^{19}F) and H_3PO_4(^{31}P) K_2PtCl_4 in D_2O (^{195}Pt). UV/Vis spectra were recorded on an Ocean Optics USB4000 spectrometer with an Ocean Optics ISS light source. Elemental analyses were performed at Atlantic Microlab (Norcross, GA).

Synthesis of 40. 39 (21.7 mg. 0.022 mmol) and *o*-chloranil (5.7 mg, 0.023 mmol) were combined and 0.7 mL CH_2Cl_2 was added, producing a deep red reaction mixture. After mixing for 20 min the reaction is complete as monitored by ^{31}P NMR. The resultant solution was stored at -20 °C. $^{31}P\{^1H\}$ NMR (161.74 MHz; CH_2Cl_2): δ 32.44 (s, $^1J_{P\text{-}195Pt}$ = 3276 Hz).

Synthesis of 42-F. A solution of KF (4 mg, 0.06 mmol) in 0.5 mL MeOH was added to a stirred, yellow suspension of **41** (77 mg, 0.06 mmol) in 2 mL CH_2Cl_2. After stirring for 1 h., all volatiles were removed from the resulting orange suspension to give an orange solid, which was extracted with 6 mL cold CH_2Cl_2. The resulting orange solution was filtered over a plug of celite, after which all volatiles were removed to give 55 mg of an orange-red powder (73%). ^1H NMR (399.59 MHz; $CDCl_3$): δ 6.11 (s, 1H, SbPh-CH), 6.35-6.49 (m, 2H, SbPh-CH), 6.49-6.59 (m ,3H, SbPh-CH), 6.87 (t, 4H, PPh-CH, $^3J_{H–H}$ = 7.30 Hz), 7.11 (t, 2H, *o*–P(Sb)C_6H_4, $^3J_{H–H}$ = 6.80 Hz), 7.15-7.43 (m, 8H, PPh-CH), 7.46-7.62 (m, 8H, PPh-CH), 7.97-8.10 (m, 4H *o*–P(Sb)C_6H_4), 8.44 (d, 2H, *o*–P(Sb)C_6H_4, $^3J_{H–H}$ = 7.77 Hz). ^{13}C NMR (100.45 MHz, $CDCl_3$): δ 122.94 (s), 126.40 (s), 126.79 (s), 127.54 (s), 127.76 (t, $J_{C\text{-}P}$ = 5.02 Hz), 128.01 (s), 128.82 (s), 129.00 (t, $J_{C\text{-}P}$ = 5.53 Hz), 129.34 (s), 129.89 (s), 132.28 (s), 132.63 (s), 132.86 (t, $J_{C\text{-}P}$ = 4.62 Hz), 133.15 (dt, $J_{C\text{-}P}$ = 7.11, 2.49 Hz), 135.39 (t, $J_{C\text{-}P}$ = 6.03 Hz), 136.04 (s). Resonances corresponding to the *o*-tetrachlorocatecholate moiety were not observed. $^{19}F\{^1H\}$ NMR (375.99 MHz, $CDCl_3$): δ -77.12 (br. s). $^{31}P\{^1H\}$ NMR (161.74 MHz; $CDCl_3$): δ 35.50 (s, $^1J_{P–195Pt}$ = 2855 Hz). Elemental analysis calculated (%) for $C_{48}H_{33}Cl_5FO_2P_2PtSb$: C, 47.38 H, 2.73; found C, 46.86 H 2.89.

Synthesis of 42-OH. A 3 mL solution of 41 (33.9 mg, 0.34 mmol) in $CHCl_3$ was layered with 0.5 mL of an alkaline aqueous solution (pH 9.0, borate buffer), and shaken for 10 s. to give a deep red-orange solution. The aqueous layer was carefully decanted, and the all volatiles were removed from the organic phase. The solid residue was extracted into 6 mL CH_2Cl_2, dried over Na_2SO_4, filtered over a plug of celite, and dried *in vacuo* to give 19.8 mg (47%) of **42**-OH as an orange solid. ^{1}H NMR (399.59 MHz; $CDCl_3$): δ 6.50-6.60 (m, 6H, SbPh-CH + PPh-CH), 6.71 (t, 1H, SbPh-CH, $^3J_{H–H}$ = 7.32 Hz), 6.95 (t, 4H, PPh-CH, $^3J_{H–H}$ = 7.69 Hz). 7.17-7.23 (m, 4H, PPh-CH), 7.30 (t, 2H, SbPh-CH, $^3J_{H–H}$ = 7.51 Hz), 7.42-7.59 (m, 10H, PPh-CH + *o*–P(Sb)C_6H_4), 7.75-7.85 (m, 4H, *o*–P(Sb)C_6H_4), 7.95 (d, 2H, $^3J_{H–H}$ = 7.87 Hz). ^{13}C NMR (100.45 MHz, $CDCl_3$): δ 116.36 (s, $O_2C_6Cl_4$), 117.71 (s, $O_2C_6Cl_4$), 118.96 (s, $O_2C_6Cl_4$), 120.89 (s, $O_2C_6Cl_4$), 126.45 (q, *J* = 28.93 Hz), 127.59 (s), 127.85 (t, *J* = 5.42 Hz), 128.28 (t, *J* = 5.32 Hz), 128.65 (s), 129.53 (m), 129.85 (s), 130.21 (s), 131.48 (t, *J* = 6.83 Hz), 131.66 (s), 132.32 (s), 133.50 (m), 135.02 (m), 135.88 (m), 145.95 (s, $O_2C_6Cl_4$), 149.44 (s, $O_2C_6Cl_4$). ^{31}P{^{1}H} NMR (161.74 MHz; $CDCl_3$): δ 39.04 (s, $^1J_{P–195Pt}$ = 2702 Hz).

Theoretical Calculations. Density functional theory (DFT) calculations (full geometry optimization) were carried out on compounds **41**, **42**-F, and **43**-OH, starting from the crystal structure geometries with Gaussian09[133] program (BP86[228, 229] functional, with the basis sets 6-31G for H, C, O, F; 6-311+G(d) for P, Cl; cc-pVTZ[197] with Stuttgart[198] relativistic small core ECP for Sb; and cc-pVTZ[230] with Stuttgart[230] relativistic small core ECP for Pt). Frequency calculations were also carried out on the optimized geometry, showing no imaginary frequencies. The optimized structures, which are in excellent

agreement with the solid-state structures, were subjected to a NBO analysis.[199] The resulting Natural Bond Orbitals(NBOs) and Natural Localized Molecular Orbitals (NLMOs) were visualized and plotted in Jimp 2 program.[99] TD-DFT calculations were performed using the mPW1PW91[95] functional and the basis sets listed above. The SMD[231] implicit solvation model was employed, using CH_2Cl_2 as the solvent.

Crystallography. Single crystals of **40**, **42**-F, and **43**-OH suitable for X-ray diffraction were obtained by layering a solution of the compound in CH_2Cl_2 with pentane. Crystal data, details of data collection, and structure refinement parameters for compounds **40**, **42**-F, and **43**-OH are compiled in Table 22. The crystallographic measurements were performed at 110(2) K or 150(2) K using a Bruker APEX-II CCD area detector diffractometer, with a graphite-monochromated Mo-Kα radiation (λ = 0.71069 Å). In each case, a specimen of suitable size and quality was selected and mounted onto a nylon loop. The semi-empirical method SADABS[100] was applied for absorption correction. The structure was solved by direct methods and refined by the full-matrix least-square technique against F^2 with the anisotropic temperature parameters for all non-hydrogen atoms. All H atoms were geometrically placed and refined in riding model approximation. Data reduction and further calculations were performed using the Bruker SAINT+[101] and SHELXTL NT[102] program packages.

Table 22. Crystal data, data collections, and structure refinements for **40, 42**-F, and **43**-OH.

	40	**42**-F	**43**-OH
Formula	$C_{48}H_{33}Cl_6O_2P_2PtSb$	$C_{48}H_{33}Cl_5FO_2P_2PtSb$	$C_{48}H_{34}Cl_4FO_3P_2PtSb$ • ($CHCl_3$)
Formula Weight	1233.28	1216.83	1198.33
Crystal Size (mm)	0.21 x 0.14 x 0.08	0.21 x 0.10 x 0.06	0.11 x 0.08 x 0.04
Crystal System	Monoclinic	Orthorhombic	Triclinic
Space Group	P2(1)/n	Pnma	P-1
a (Å)	11.838(3)	11.034(3)	12.511(3)
b (Å)	37.089(10)	14.993(4)	14.673(3)
c (Å)	14.663(4)	26.373(7)	14.848(3)
α (°)	90	90	100.924(3)
β (°)	109.471(3)	90	97.080(2)
γ (°)	90	90	113.207(2)
V ($Å^3$)	6070(3)	4363(2)	2399.9(9)
Z	4	4	2
ρ_{calc} (g/cm^3)	1.814	1.875	1.658
μ (mm^{-1})	3.545	4.249	3.806
F(000)	3232	2324	1164
T (K)	110(2)	110(2)	150(2)
Scan mode	ω, φ	ω, φ	ω, φ
hkl Range	-15 → 14	-14 → 0	-17 → 16
	-48 → 47	-20 → 0	-20 → 19
	-17 → 18	0 → 36	0 → 20
Reflections collected	51830	54411	30652
Unique reflections [Rint]	13237 [0.0649]	6583 [0.0307]	12439 [0.0658]
Reflns. used for refinement	13237	6169	12439
Refined parameters	517	300	581
GooF	1.021	1.073	1.022
R1[a], *w*R2[b] (all data)	0.0778, 0.1268	0.0750, 0.1583	0.0576, 0.1043
ρ_{fin} (max., min.) (eA^{-3})	2.249, -1.483	6.343, -2.099	1.392, -1.627

[a]$R1 = \sum||F_o| - |F_c||/\sum|F_o|$. [b] $wR2\ ([w(F_o^2 - F_c^2)^2]/[\sum w(F_o^2)^2])^{1/2}$; $w = 1/[\sigma^2(F_o^2) + (ap)^2 + bp]$; $p = (F_o^2 + 2F_c^2)/3$ with $a = 0.0650$ for **40**, 0.0336 for **42**-F, and 0.0411 for **43**-OH ; and $b = 0.0000$ for **40**, 145.5443 for **42**-F, and 5.0212 for **43**-OH

7. FORMAL PHOTOREDUCTIVE ELIMINATION OF A C-X BOND FROM A SB-PT HETEROBIMETALLIC PLATFORM

7.1 Introduction

As a key step in the envisaged catalytic photochemical production of hydrogen from hydrohalic acids, the study of the photoreductive elimination of halogen equivalents has attracted increasing interest in the past decade.[61] One of the most successful strategies in designing complexes able to sustain halogen photoreductive elimination is that of utilizing homo- or heterobimetallic platforms in which two metal centers are held in close proximity and participate in synergistic support of redox activity. As part of our interest in redox-active main group compounds, we have shown that both antimony[70] and tellurium[69] ligands are responsive to redox changes at adjoining transition metal centers and can act to facilitate photoreductive elimination of halogen equivalents. In particular, the Sb-Pt compound **14** was shown to sustain chlorination and subsequent photoreductive elimination of a chlorine equivalent.

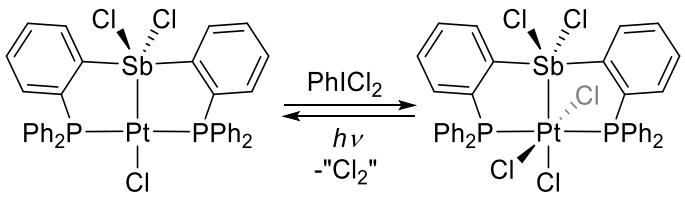

14 **15**

Figure 91. Oxidation and photoreductive regeneration of **14** as reported by Yang.[70]

In addition to acting as photoredox platforms for energy applications, the coordination non-innocent properties of antimony have the potential to be used in conjunction with a redox active transition metal to trigger anion release. Such "photocages" for anions are of special interest to the biology community, as they allow for excellent spatial and temporal control over anion release; an appealing feature for the study of anion-driven cellular processes.[232, 233] In a prior investigation published in a dissertation by Dr. Iou-Sheng Ke, this concept was approached by using the Sb-Pt complex **39**.[214] Similar to compound **14**, **39** undergoes chlorination by $PhICl_2$ to give **44** , which was structurally and spectroscopically characterized. As the chloride anion is more weakly bound in **39** relative to **44**, it was proposed that the photoreductive elimination of a chlorine equivalent from **44** would be able to trigger the release of a chloride anion from the antimony center, especially in aqueous media.

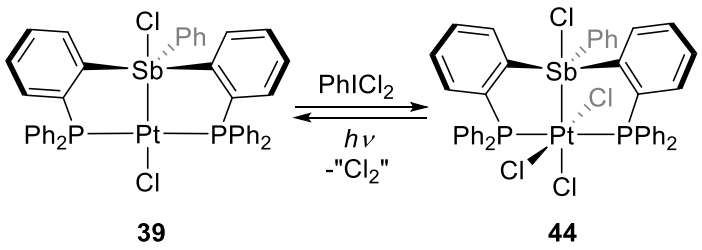

39 **44**

Figure 92. Oxidation and photoreductive regeneration of **39** as reported by Ke.[214]

With the reported success of this strategy, we next resolved to investigate the photolysis of **44** in greater detail in hopes of gleaning information that may lead to better antimony-transition metal photocages.

7.2 Photoreductive formation of a C-X bond

In an effort to better understand the photolysis of compound **44**, we sought to reinvestigate the process in the hope of observing intermediate products. To this end, a solution of **44** in CH_2Cl_2 (2.5×10^{-2} M) was photolyzed using a 75 W xenon lamp, with $^{31}P\{^1H\}$ NMR spectra being recorded at regular intervals (Figure 93). After 5 minutes of photolysis, two new resonances (**14** and **45**) appear in addition to **44 (**δ 35.03 ppm, $^1J_{P-^{195}Pt}$ = 1942 Hz) in the $^{31}P\{^1H\}$ NMR spectrum of the reaction mixture. After 20 minutes of photolysis, **44** is completely consumed. Concomitantly, the ratio of **14** to **45** begins to increase, and a pair of strongly roofed doublets (**46**) begins to grow in. After 50 minutes of photolysis, intermediate **45** is completely consumed, leaving **14** and **46** as the major photolysis products alongside a number of minor resonances.

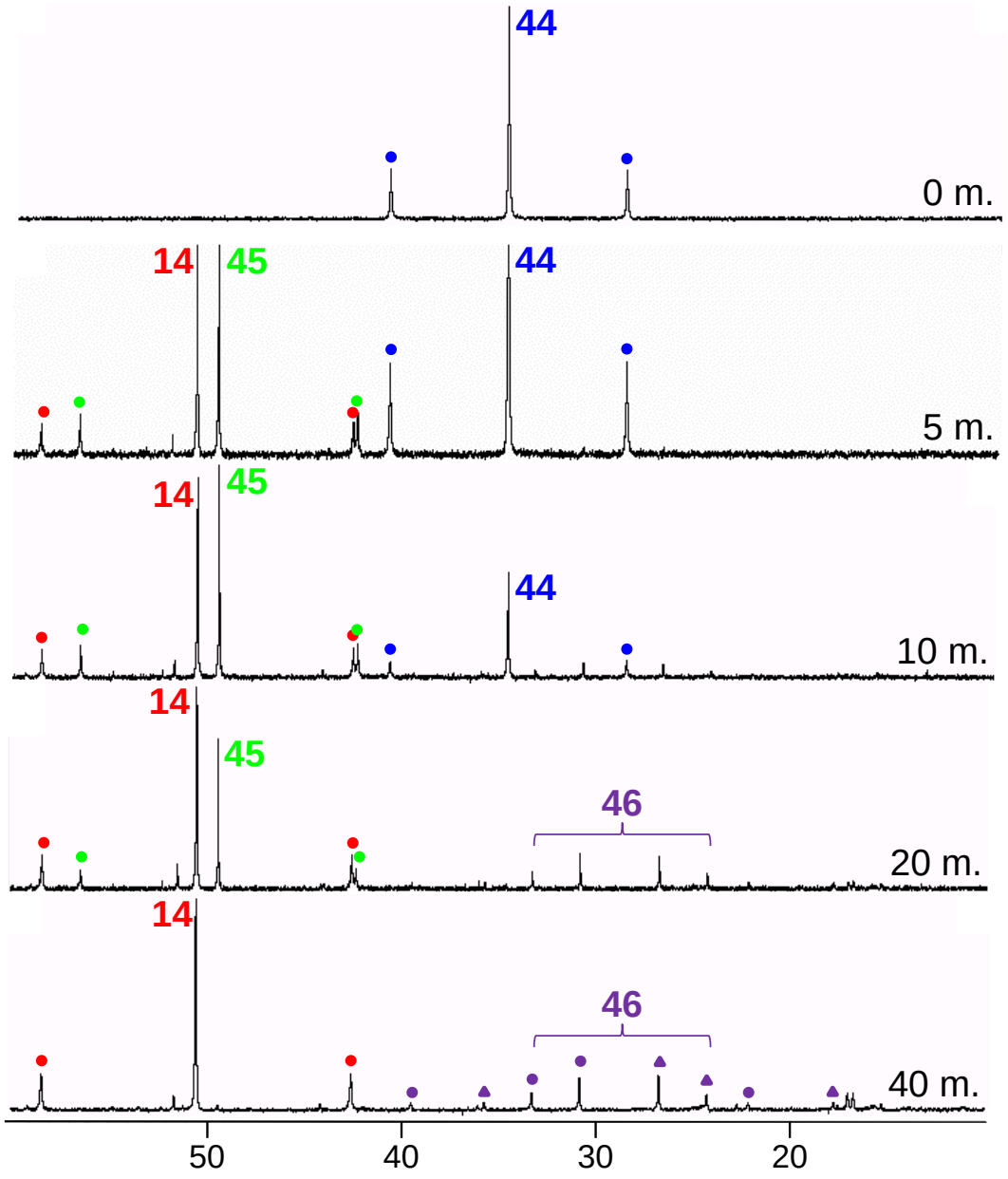

Figure 93. $^{31}P\{^{1}H\}$ NMR spectra of the reaction mixture at progressive time points during the photolysis of **44**. Principle resonances are labeled, and ^{195}Pt satellites are marked in the color corresponding to their principle resonance.

The observation of compound **14** as the major product of the photolysis, characterized by a singlet at 50.34 ppm in the $^{31}P\{^{1}H\}$ NMR flanked by ^{195}Pt satellites ($^{1}J_{P-195Pt}$ = 2560 Hz), stands at odds with the initial report that the photolysis of **44** afforded **39** (δ ($CDCl_3$) 53.95 ppm, $^{1}J_{P-195Pt}$ = 2706 Hz) as the major product.[214] The use of 2,3-dimethyl-1,3-butadiene as a radical trap did not significantly alter the fate of the reaction The identity of **14** as the major product was confirmed by a single crystal X-ray diffraction study, which produced a unit cell identical to that previously reported.[70] Instead of the expected elimination of a chlorine equivalent, the formation of compound **14** constitutes a formal elimination of chlorobenzene. The formation of chlorobenzene was confirmed by GC-MS, with the observed peak at m/z = 111.9 matching the molecular ion $[ClC_6H_5]^+$. In order to quanitfy the production of chlorobenzene, a GC of the photolyzed reaction mixture was recorded. Based on a calibration curve comparing known concentrations of chlorobenzene to 1,2-dichlorobenzene, the yield of chlorobenzene was estimated to be 37% based on the initial concentration of **44**. It is important to note that the chlorobenzene produced in the photolysis could simply be the product of phenyl radical extrusion from the antimony center, followed by chlorine abstraction from the CH_2Cl_2 solvent. Such radical extrusion has previously been demonstrated in the case of Ph_4SbOO^tBu, which was shown to produce chlorobenzene and benzene in addition to a number of antimony-containing products when irradiated in chlorinated solvents.[234]

With compound **14** firmly established as the major photolysis product, we next sought to establish the identity of the other two observed major resonances. Compound **45** displays a singlet resonance at 49.35 ppm, flanked by ^{195}Pt satellites ($^{1}J_{P-195Pt}$ = 2277 Hz).

The $^{1}J_{P-195Pt}$ value observed for **45** is greatly diminished relative to that found for **39** ($^{1}J_{P-195Pt}$ = 2706 Hz) or **14** ($^{1}J_{P-195Pt}$ = 2560 Hz), suggesting that **45** may still contain an oxidized platinum center. Unfortunately, all efforts to further characterize this intermediate failed and we are unable to further speculate on its identity. The second major product of the photolysis of **44**, compound **46**, is characterized by a pair of strongly coupled ($^{2}J_{P-P}$ = 395.71 Hz) doublets at 25.46 and 31.96 ppm. In addition, each doublet is bordered by ^{195}Pt satellites ($^{1}J_{P-195Pt}$ = 2787 Hz, $^{1}J_{P-195Pt}$ = 2886 Hz), suggesting that the phosphorus nuclei in **46** remain coordinated to a platinum center. Taken together, the spectroscopic features of **46** are strongly suggestive of a species containing a pair of nonidentical phosphine ligands situated *trans* to one another, as in the platinum PCP compound $[(C_{10}H_5(CH_2P^tBu_2)_2)Pt(Cl)]$,[235] whose naphthalene backbone renders the two phosphine groups nonidentical ($^{2}J_{P-P}$ = 395.71 Hz, $^{1}J_{P-195Pt}$ = 2858 Hz). On the basis of this $^{31}P\{^{1}H\}$ NMR data as well as the observation of **14** as the major photolysis product, we speculate that this peak corresponds to a species which arises from either the elimination or the radical extrusion of an *o*-phenylene phosphine and a chlorine atom (Figure 94). Recombination of this eliminated phosphine with the Pt(II) species formed *via* the elimination process would result in transfer of a chloride anion from antimony to platinum, a process precedented by the gold species **33**.

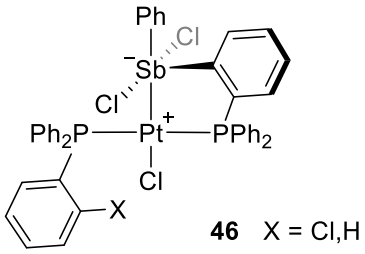

Figure 94. Speculated identity of compound **46** produced during the photolysis of **44**.

7.3 Conclusions

The photolysis of compound **44** reinvestigated with the aim of observing intermediates in the photolytic process. Two previously unreported species (**45** and **46**), were observed as intermediates in this process. Unexpectedly, we found that the major photolysis product was the formal chlorobenzene elimination product **14** rather than compound **39** as expected. The identity of **14** was corroborated by its $^{31}P\{^{1}H\}$ resonance and $^{1}J_{P-195Pt}$ value, and the formation of chlorobenzene was confirmed by GC-MS and quantified by GC studies. While the formation of chlorobenzene could be interpreted as being formed from concerted elimination of a chlorine atom and phenyl radical across the Sb-Pt bond or directly from the antimony center, we cannot exclude the possibility of phenyl radical extrusion followed by chlorine atom abstraction from CH_2Cl_2.

7.4 Experimental section

General Considerations. *Antimony compounds should be handled cautiously.* Compounds **39**[110, 214], and **44**[110, 214] were prepared according to reported procedures. Solvents were dried by passing through an alumina column (n-pentane and CH_2Cl_2) or by reflux under N_2 over Na/K (Et_2O and THF). All other solvents were used as received.

Ambient temperature NMR spectra were recorded on a Varian Unity Inova 400 FT NMR (161.74 MHz for ^{31}P) spectrometer. Chemical shifts (δ) are given in ppm and are referenced against H_3PO_4(^{31}P). GC-MS of the reaction mixture was performed on Ultra GC/DSQ (ThermoElectron, Waltham, MA). A Rxi-5ms was used as a gas chromatographic column with dimensions of 60 m length, 0.25 mm i.d., and 0.25 μm film thickness (Restek, Bellefonte, PA). Helium was used as a carrier gas at constant flow of 1.5 mL/min. Splitless and split (1:10) injection were used. Transfer line and ion source were held at 250 °C. The column temperature was maintained at 50 °C for 5 min and raised to 320 °C at 20 °C/min. Mass spectra were acquired in full scan mode in the range of 30-500 m/z. The GC of the reaction mixture was recorded using an Agilent (Santa Clara, CA) 6980 GC. A Rtx-1 was used as a gas chromatographic column with dimensions of 15 m length, 0.53 mm i.d., and 0.5 μm film thickness (Restek, Bellefonte, PA). Helium was used as a carrier gas at constant flow of 1.5 mL/min. The column temperature was maintained at 50 °C for 1 min and raised to 320 °C at 4 °C/min.

Photolysis Reactions. Photolysis reactions were performed using broad spectrum light generated from a 75 W xenon lamp integrated in a PTI QuantaMaster 40 fluorescence spectrometer. A typical photolysis reaction is documented below:

To an NMR tube charged with 21.7 mg (0.020 mmol) **44** was added 0.7 mL CH_2Cl_2 to give a yellow solution. The NMR tube was held in proximity of the lamp by means of a clamp and photolyzed in several intervals. At the conclusion of each interval, the $^{31}P\{^1H\}$ NMR was recorded. The sample was kept in the dark at all times in between photolysis.

8. SUMMARY

8.1 Origins of coordination non-innocence in transition metal stibine complexes

Spurred by the documented ability of Sb-Pd lantern complexes to serve as fluoride anion sensors, a fundamental reinvestigation into a series of nickel lantern complexes of the form [ClNi((*o*-(Ph_2P)C_6H_4)$_3$E)][Cl] (E = P ([**21**][Cl]), As ([**22**][Cl]), Sb (**23**-Cl)) first described by Venanzi was undertaken. Crystal structures of the above compounds showed that in contrast to [**21**][Cl] and [**22**][Cl], which form discrete ion pairs, the chloride anion in **23**-Cl coordinates to the basal antimony center. Comparison of the structures of the cations [**21**]$^+$, [**22**]$^+$, and [**23**]$^+$ with those of their respective free ligands found that the antimony center undergoes the greatest distortion in ∡C-E-C upon coordination.

DFT analysis of [**21**]$^+$, [**22**]$^+$, and [**23**]$^+$ finds that the E-Ni-Cl system can be viewed as a three-center four-electron bond. The LUMO energies of these complexes decreases in the order Sb > As ≈ P. Both DFT and NBO analysis finds that the E-Ni bond in the antimony derivative is considerably more polarized towards the nickel center relative to its phosphine and arsine analogues.

Model complexes of the form [ClNi(PH_3)$_3$(EH_3)]$^+$ were utilized in order to gauge the effect of changing the basal ∡C-E-C on the electronics of the lantern complexes,. Expansion of ∡C-E-C in each case causes the energy level of the LUMO to rise, concomitant with the polarization of the E-Ni bond towards Ni. These results suggest that while the geometric distortion of the basal pnictine perturbs the E-Ni-Cl system, the ability of the antimony derivative [**23**]$^+$ to incorporate a fifth ligand can likely be attributed to the steric effects of such a distortion in conjunction with electrostatic effects.

8.2 Electronic effects of coordination non-innocence in transition metal stibine complexes

In an effort to better understand the effect of anion binding events at coordination non-innocent stibines on the Sb-M bond a series of Sb-Pt complexes ([**26**][SbF_6]$_2$, [**27**][SbF_6], and **28**) separated by formal stepwise coordination of two fluoride anions at the antimony center were synthesized. The first equivalent of fluoride binds *trans* to the Sb-Pt bond, while the second equivalent binds *trans* to an Sb-C bond. Successive fluoride coordination results in significant lengthening of the Sb-Pt bond. This structural change is accompanied by an increase in $^1J_{Pt\text{-}P}$, indicating the increasing electron density at the platinum center. This view is supported by a decrease in the ν (C≡N) of the auxiliary isocyanide ligand coordinated to the platinum center across the series. For all of the metric mentioned above, the magnitude of the perturbation is largest for the coordination of the first fluoride equivalent, in line with this event populating a predominantly antibonding Sb-Pt-Cl orbital. These results are corroborated by NBO and QTAIM calculations, which show progressive weakening and polarization of the Sb-Pt bond upon successive fluoride coordination.

8.3 Preparation and characterization of gold (I) complexes featuring an ambiphilic phosphine-chlorostibine ligand

In our continuing interest in Lewis acidic main group ligands, we initiated an investigation of ambiphilic antimony ligands containing only one donor buttress. The phosphinylstibine ligand **29**-Cl, which features a mildly Lewis acidic dichloroarylstibine group was synthesized. The coordination chemistry of this ligand to gold is compared with

that of the known phosphinylstibine ligand **29**-Ph, which features a triarylstibine functionality. The resulting gold species **30** and **31** while structurally similar, show markedly different secondary aggregation in the solid state in which the antimony center in **31** acts as a Lewis acid while the antimony center in **30** acts as a Lewis base. NBO analysis of these two species finds that in both cases the antimony centers act as "confused" σ-donor-acceptor ligand, with differences in the ratio of Au→Sb/Sb→Au based on the antimony substituents. Similar to previously reported phosphinylstibine gold complexes, the antimony center in **30** undergoes oxidation by *o*-chloranil to afford the gold-stiborane complex **35**. Structural and NBO analysis of **35** suggests that in contrast to related complexes featuring 2-3 supporting phosphine buttresses, oxidation of the antimony center weakens the Au-Sb interaction.

Binding of a second phosphine ligand to the gold center in **31** was shown to result in transfer of the gold-bound chloride to the pendant stibine to form the zwitterionic antimonates **32** and **33**. Intrigued by this reactivity, we demonstrated that **30**, **31**, and **33** are active catalysts for the silver-salt free electrophilic cyclization of propargylic amides. While all catalysts investigated are less active than traditionally used gold catalysts such as $Ph_3PAuNTf_2$, these results provide proof of concept that pendant, Lewis acidic stibines can active otherwise inactive Ph_3PAuCl species for catalysis.

8.4 Redox and anion exchange chemistry of a nickel stibine complex

Having previously demonstrated the ability of coordinated stibine ligands to undergo antimony-centered redox reactions, we sought to investigate whether other valence isoelectronic fragments would display similar reactivity. To this end, a zerovalent nickel

complex (**36**) was synthesized and reacted with the two electron oxidant $PhICl_2$. The product of this reaction was found to be the divalent lantern complex **23**-Cl, which may be viewed as a product of an oxidation occurring across the Sb-Ni bond.

Treatment of **23**-Cl with catecholate dianion in the presence of cyclohexylisocyanide afforded **38**, which can be viewed as a zerovalent nickel-stiborane complex. NBO analysis is used to support the changing nature of the Sb-Ni interaction, with the best description of the Sb-Ni interaction changing from an Sb→Ni dative bond in **36**, to a Sb-Ni covalent bond in **23**-Cl, and finally to a Ni→Sb dative bond in **38**. Thus this series of compounds constitutes a series where the antimony center progressively assumes L, X, and Z ligand behavior.

8.5 Coordination non-innocence of a platinum stiboranyl complex

Continuing a prior investigation, we sought to determine whether a coordination non-innocent antimony center could act in conjunction with a redox-active platinum center to serve as an anion-responsive platform. Compound **39** was previously shown to undergo two-electron oxidation by *o*-chloranil and subsequent platinum-mediated antimony-carbon bond insertion to give **41**. In the presented results, this process was shown to proceed through the intermediate species **40**, in which the stiborane product from the initial oxidation by *o*-chloranil acts as a Z-type ligand towards the proximal platinum center.

Through a series of anion exchange and hydrolysis reactions, the covalent Pt-Sb bond in compound **41** is cleaved to form the Sb (μ_2-OH) Pt species **43**-OH, which was previously misidentified as a fluoride-bridged species. This transformation was found to

proceed through two Sb (μ_2-Cl) Pt intermediates. The chloride-for-fluoride exchange product **42**-F was isolated by treatment of **41** with methanolic KF. The partial hydrolysis product **42**-OH was isolated by treatment of **41** with an alkaline aqueous solution. NBO analysis suggests that anion coordination at antimony results triggers a reversible switch of a stiboranyl X-ligand (one electron donor) into a stiborane Z-ligand (σ-accepting ligand). As both intermediates **42**-F and **42**-OH are strongly colored, we provided proof of concept that the reversible transition from **41** to **42**-F may be applied for anion sensing. At present, however, highly competitive hydroxide binding limits the anion selectivity of **41** in such a role. In addition to anion sensing, metallostiboranes such as **41** may have the potential to be exploited as anion-actuated molecular devices.

8.6 Formal photoreductive elimination of a C-X bond from an Sb-Pt heterobimetallic platform

In our continuing interest in the photochemistry of main group-transition metal complexes, we reinvestigated the photochemistry of a Pt^{IV}-Sb compound (**44**). The photolysis of compound **44**, which was previously proposed to act as a photocage for a chloride anion, was reinvestigated with the aim of observing intermediates in the photolytic process. In addition to observing two previously unreported species (**45** and **46**), we unexpectedly observed that the major product of the photolysis was **14** rather than compound **39** as expected. The identity of **14** was corroborated by its $^{31}P\{^1H\}$ resonance and $^1J_{P-195Pt}$ value, as well as a single crystal X-ray diffraction study. The formation of chlorobenzene as a photolysis product was confirmed by GC-MS and quantified by GC studies. While the exact mechanism of chlorobenzene formation is unknown, the

formation of **14** *via* the photoreduction of **44** is intriguing, in that it confirms the direct involvement of antimony in the photolytic process.

Although compound **45** was observed as in intermediate by $^{31}P\{^{1}H\}$ NMR, no further characterization could be made. The minor photolysis product **46** was assigned as an asymmetric *trans* bis(phosphine) platinum (II) species on the basis of $^{31}P\{^{1}H\}$ NMR. If the asymmetry of the two phosphine nuclei in this species is indeed derived from cleavage of an *o*-phenylene Sb-C bond, it provides further evidence of the ability of the antimony center to directly participate in bimetallic photolysis. Much work remains to be done in order to fully elucidate the photolysis of **44**, including determining the mechanism of chlorobenzene elimination. Systematic halide substitution at both antimony and platinum could attest to the origin of the chlorine atom incorporated into the chlorobenzene product (Sb-bound, Pt-bound, or chlorine abstraction from CH_2Cl_2).

REFERENCES

(1) Levason, W.; Reid, G. *Coord. Chem. Rev.* **2006,** *250* (19–20), 2565.

(2) Bigorgne, M.; Zelwer, A. *Bull. Soc. Chim. Fr.* **1960**, 1986.

(3) Bouquet, G.; Bigorgne, M. *Bull. Soc. Chim. Fr.* **1962**, 433.

(4) Benlian, D.; Bigorgne, M. *Bull. Soc. Chim. Fr.* **1963,** (8-9), 1583.

(5) Bigorgne, M. *J. Inorg. Nucl. Chem.* **1964,** *26* (1), 107.

(6) Dunne, B. J.; Morris, R. B.; Orpen, A. G. *J. Chem. Soc., Dalton Trans.* **1991,** (S), 653.

(7) J. Holmes, N.; Levason, W.; Webster, M. *J. Chem. Soc., Dalton Trans.* **1998,** (20), 3457.

(8) M. Hill, A.; J. Holmes, N.; R. J. Genge, A.; Levason, W.; Webster, M.; Rutschow, S. *J. Chem. Soc., Dalton Trans.* **1998,** (5), 825.

(9) Schulz, S.; Kuczkowski, A.; Nieger, M. *J. Organomet. Chem.* **2000,** *604* (2), 202.

(10) Schulz, S.; Nieger, M. *J. Chem. Soc., Dalton Trans.* **2000,** (5), 639.

(11) Schuchmann, D.; Kuczkowski, A.; Fahrenholz, S.; Schulz, S.; Flörke, U. *Eur. J. Inorg. Chem.* **2007,** *2007* (7), 931.

(12) Schuchmann, D.; Schulz, S.; Florke, U. *Acta Crystallographica Section E* **2007,** *63* (6), m1606.

(13) Schulz, S.; Kuczkowski, A.; Nieger, M. *J. Chem. Crystallogr.* **2010,** *40* (12), 1163.

(14) Schulz, S.; Kuczkowski, A.; Nieger, M.; Saxell, H. *J. Organomet. Chem.* **2010,** *695* (21), 2281.

(15) Hering, C.; Lehmann, M.; Schulz, A.; Villinger, A. *Inorg. Chem.* **2012,** *51* (15), 8212.

(16) Holmes, N. J.; Levason, W.; Webster, M. *J. Organomet. Chem.* **1999,** *584* (1), 179.

(17) Green, M. L. H. *J. Organomet. Chem.* **1995,** *500* (1–2), 127.

(18) Shriver, D. F. *Acc. Chem. Res.* **1970,** *3* (7), 231.

(19) Parkin, G. *Organometallics* **2006,** *25* (20), 4744.

(20) Hill, A. F. *Organometallics* **2006,** *25* (20), 4741.

(21) Bouhadir, G.; Amgoune, A.; Bourissou, D. Chapter 1 - Phosphine-Boranes and Related Ambiphilic Compounds: Synthesis, Structure, and Coordination to Transition Metals. In *Adv. Organomet. Chem.*, F. H. Anthony; J. F. Mark, Eds. Academic Press: 2010; Vol. Volume 58, pp 1.

(22) Amgoune, A.; Bourissou, D. *Chem. Commun.* **2011,** *47* (3), 859.

(23) Braunschweig, H.; Dewhurst, R. D. *Dalton Trans.* **2011,** *40* (3), 549.

(24) Kameo, H.; Nakazawa, H. *Chem. Asian J.* **2013,** *8* (8), 1720.

(25) Rudd, P. A.; Liu, S.; Gagliardi, L.; Young, V. G.; Lu, C. C. *J. Am. Chem. Soc.* **2011,** *133* (51), 20724.

(26) Bouhadir, G.; Bourissou, D. *Chem. Soc. Rev.* **2016,** *45* (4), 1065.

(27) Harman, W. H.; Peters, J. C. *J. Am. Chem. Soc.* **2012,** *134* (11), 5080.

(28) Anderson, J. S.; Rittle, J.; Peters, J. C. *Nature* **2013,** *501* (7465), 84.

(29) Inagaki, F.; Matsumoto, C.; Okada, Y.; Maruyama, N.; Mukai, C. *Angew. Chem. Int. Ed.* **2015,** *54* (3), 818.

(30) Benjamin, S. L.; Levason, W.; Reid, G.; Warr, R. P. *Organometallics* **2012,** *31* (3), 1025.

(31) Lin, T.-P.; Wade, C. R.; Pérez, L. M.; Gabbaï, F. P. *Angew. Chem. Int. Ed.* **2010,** *49* (36), 6357.

(32) Wade, C. R.; Lin, T.-P.; Nelson, R. C.; Mader, E. A.; Miller, J. T.; Gabbaï, F. P. *J. Am. Chem. Soc.* **2011,** *133* (23), 8948.

(33) Lin, T.-P.; Nelson, R. C.; Wu, T.; Miller, J. T.; Gabbai, F. P. *Chem. Sci.* **2012,** *3* (4), 1128.

(34) Hudnall, T. W.; Chiu, C.-W.; Gabbaï, F. P. *Acc. Chem. Res.* **2009,** *42* (2), 388.

(35) Wade, C. R.; Lin, T.-P.; Nelson, R. C.; Mader, E. A.; Miller, J. T.; Gabbaï, F. P. *J. Am. Chem. Soc.* **2011,** *133*, 8948.

(36) Barnett, B. R.; Moore, C. E.; Chandrasekaran, P.; Sproules, S.; Rheingold, A. L.; DeBeer, S.; Figueroa, J. S. *Chem. Sci.* **2015,** *6* (12), 7169.

(37) Ke, I.-S.; Gabbaï, F. P. *Inorg. Chem.* **2013,** *52* (12), 7145.

(38) Yang, H.; Gabbaï, F. P. *J. Am. Chem. Soc.* **2015,** *137* (41), 13425.

(39) Sircoglou, M.; Bontemps, S.; Mercy, M.; Saffon, N.; Takahashi, M.; Bouhadir, G.; Maron, L.; Bourissou, D. *Angew. Chem. Int. Ed.* **2007,** *46* (45), 8583.

(40) Lin, T.-P.; Ke, I.-S.; Gabbaï, F. P. *Angew. Chem. Int. Ed.* **2012,** *51* (20), 4985.

(41) Tschersich, C.; Limberg, C.; Roggan, S.; Herwig, C.; Ernsting, N.; Kovalenko, S.; Mebs, S. *Angew. Chem. Int. Ed.* **2012,** *51* (20), 4989.

(42) Benjamin, S. L.; Levason, W.; Light, M. E.; Reid, G.; Rogers, S. M. *Organometallics* **2014,** *33* (11), 2693.

(43) Benjamin, S. L.; Reid, G. *Coord. Chem. Rev.* **2015,** *297–298*, 168.

(44) Ke, I.-S.; Myahkostupov, M.; Castellano, F. N.; Gabbaï, F. P. *J. Am. Chem. Soc.* **2012,** *134* (37), 15309.

(45) Pan, B.; Gabbaï, F. P. *J. Am. Chem. Soc.* **2014,** *136* (27), 9564.

(46) Hirai, M.; Cho, J.; Gabbaï, F. P. *Chem. Eur. J.* **2016,** *22* (19), 6537.

(47) Hirai, M.; Myahkostupov, M.; Castellano, F. N.; Gabbaï, F. P. *Organometallics* **2016,** *35* (11), 1854.

(48) Hirai, M.; Gabbai, F. P. *Chem. Sci.* **2014,** *5* (5), 1886.

(49) Wade, C. R.; Ke, I.-S.; Gabbaï, F. P. *Angew. Chem. Int. Ed.* **2012,** *51* (2), 478.

(50) Burton, J. W. *Sci. Synth.* **2002,** *4*, 53.

(51) Malisch, W.; Kaul, H.-A.; Gross, E.; Thewalt, U. *Angewandte Chemie International Edition in English* **1982,** *21* (7), 549.

(52) Malisch, W.; Panster, P. *Angewandte Chemie International Edition in English* **1974,** *13* (10), 670.

(53) Kaul, H.-A.; Greissinger, D.; Luksza, M.; Malisch, W. *J. Organomet. Chem.* **1982,** *228* (2), C29.

(54) Malisch, W.; Janta, R. *Angewandte Chemie International Edition in English* **1978,** *17* (3), 211.

(55) Wade, C. R.; Gabbaï, F. P. *Angew. Chem. Int. Ed.* **2011,** *50* (32), 7369.

(56) Heyduk, A. F.; Macintosh, A. M.; Nocera, D. G. *J. Am. Chem. Soc.* **1999,** *121* (21), 5023.

(57) Heyduk, A. F.; Nocera, D. G. *Science* **2001,** *293* (5535), 1639.

(58) Dempsey, J. L.; Esswein, A. J.; Manke, D. R.; Rosenthal, J.; Soper, J. D.; Nocera, D. G. *Inorg. Chem.* **2005,** *44* (20), 6879.

(59) Esswein, A. J.; Veige, A. S.; Nocera, D. G. *J. Am. Chem. Soc.* **2005,** *127* (47), 16641.

(60) Cook, T. R.; Esswein, A. J.; Nocera, D. G. *J. Am. Chem. Soc.* **2007,** *129* (33), 10094.

(61) Esswein, A. J.; Nocera, D. G. *Chem. Rev.* **2007,** *107* (10), 4022.

(62) Cook, T. R.; Surendranath, Y.; Nocera, D. G. *J. Am. Chem. Soc.* **2009,** *131* (1), 28.

(63) Teets, T. S.; Lutterman, D. A.; Nocera, D. G. *Inorg. Chem.* **2010,** *49* (6), 3035.

(64) Teets, T. S.; Cook, T. R.; McCarthy, B. D.; Nocera, D. G. *Inorg. Chem.* **2011,** *50* (11), 5223.

(65) Teets, T. S.; Nocera, D. G. *Chem. Commun.* **2011,** *47* (33), 9268.

(66) Cook, T. R.; McCarthy, B. D.; Lutterman, D. A.; Nocera, D. G. *Inorg. Chem.* **2012,** *51* (9), 5152.

(67) Carrera, E. I.; McCormick, T. M.; Kapp, M. J.; Lough, A. J.; Seferos, D. S. *Inorg. Chem.* **2013,** *52* (23), 13779.

(68) Carrera, E. I.; Seferos, D. S. *Dalton Trans.* **2015,** *44* (5), 2092.

(69) Lin, T.-P.; Gabbaï, F. P. *J. Am. Chem. Soc.* **2012,** *134* (29), 12230.

(70) Yang, H.; Gabbaï, F. P. *J. Am. Chem. Soc.* **2014,** *136* (31), 10866.

(71) Yang, H.; Lin, T.-P.; Gabbaï, F. P. *Organometallics* **2014,** *33* (17), 4368.

(72) Wu, C. Y.; Horibe, T.; Jacobsen, C. B.; Toste, F. D. *Nature* **2015,** *517* (7535), 449.

(73) Jones, J. S.; Gabbaï, F. P. *Acc. Chem. Res.* **2016,** *49* (5), 857.

(74) Politzer, P.; Murray, J. S.; Clark, T. *PCCP* **2013,** *15* (27), 11178.

(75) Politzer, P.; Murray, J.; Janjić, G.; Zarić, S. *Crystals* **2014,** *4* (1), 12.

(76) Dawson, J. W.; Venanzi, L. M. *J. Am. Chem. Soc.* **1968,** *90* (26), 7229.

(77) Higginson, B. R.; McAuliffe, C. A.; Venanzi, L. M. *Inorg. Chim. Acta* **1971,** *5*, 37.

(78) Goggin, P. L.; Knight, R. J.; Sindellari, L.; Venanzi, L. M. *Inorg. Chim. Acta* **1971,** *5*, 62.

(79) Dawons, J. W.; Lane, B. C.; Mynott, R. J.; Venanzi, L. M. *Inorg. Chim. Acta* **1971,** *5*, 25.

(80) Wade, C. R. Synthesis and study of boron and antimony Lewis acids as small anion receptors and ligands towards transition metals. Texas A&M University, College Station, TX, 2011.

(81) Sharutin, V. V.; Sharutina, O. K.; Pakusina, A. P.; Platonova, T. P.; Zadachina, O. P.; Gerasimenko, A. V. *Russ. J. Coord. Chem.* **2003,** *29* (2), 89.

(82) Alcock, N. W.; Pennington, M.; Willey, G. R. *Acta Crystallogr., Sect. C: Cryst. Struct. Commun.* **1985,** *41* (10), 1549.

(83) Neumüller, B.; Dehnicke, K. *Z. Anorg. Allg. Chem.* **2010,** *636* (8), 1516.

(84) Andratschke, M.; Dassler, A.; Klement, U.; Range, K. J. *Z. Naturforsch., B: Chem. Sci.* **1994,** *49* (4), 576.

(85) Ferguson, G.; Glidewell, C.; Lloyd, D.; Metcalfe, S. *J. Chem. Soc., Perkin Trans. 2* **1988,** (5), 731.

(86) Ziebart, C.; Federsel, C.; Anbarasan, P.; Jackstell, R.; Baumann, W.; Spannenberg, A.; Beller, M. *J. Am. Chem. Soc.* **2012,** *134* (51), 20701.

(87) Bojan, V. R.; Fernández, E. J.; Laguna, A.; López-de-Luzuriaga, J. M.; Monge, M.; Olmos, M. E.; Puelles, R. C.; Silvestru, C. *Inorg. Chem.* **2010,** *49* (12), 5530.

(88) Pimentel, G. C. *J. Chem. Phys.* **1951,** *19* (4), 446.

(89) Rundle, R. E. *J. Chem. Phys.* **1949,** *17* (8), 671.

(90) A. Landrum, G.; Goldberg, N.; Hoffmann, R. *J. Chem. Soc., Dalton Trans.* **1997,** (19), 3605.

(91) Aragoni, M. C.; Arca, M.; Devillanova, F. A.; Garau, A.; Isaia, F.; Lippolis, V.; Mancini, A. *Bioinorganic Chemistry and Applications* **2007,** *2007*, 17416.

(92) Hartley, J. G.; Venanzi, L. M.; Goodall, D. C. *Journal of the Chemical Society (Resumed)* **1963,** (0), 3930.

(93) Higginson, B. R.; McAuliffe, C. A.; Venanzi, L. M. *Inorg. Chim. Acta* **1971,** *5* (1), 37.

(94) Frisch, M. J.; Trucks, G. W.; Schlegel, H. B.; Scuseria, G. E.; Robb, M. A.; Cheeseman, J. R.; Scalmani, G.; Barone, V.; Mennucci, B.; Petersson, G. A.; Nakatsuji, H.; Caricato, M.; Li, X.; Hratchian, H. P.; Izmaylov, A. F.; Bloino, J.; Zheng, G.; Sonnenberg, J. L.; Hada, M.; Ehara, M.; Toyota, K.; Fukuda, R.; Hasegawa, J.; Ishida, M.; Nakajima, T.; Honda, Y.; Kitao, O.; Nakai, H.; Vreven, T.; Montgomery, J., J. A.; ; Peralta, J. E.; Ogliaro, F.; Bearpark, M.; Heyd, J. J.; Brothers, E.; Kudin, K. N.; Staroverov, V. N.; Kobayashi, R.; Normand, J.; Raghavachari, K.; Rendell, A.; Burant, J. C.; Iyengar, S. S.; Tomasi, J.; Cossi, M.; Rega, N.; Millam, J. M.; Klene, M.; Knox, J. E.; Cross, J. B.; Bakken, V.; Adamo, C.; Jaramillo, J.; Gomperts, R.; Stratmann, R. E.; Yazyev, O.; Austin, A. J.; Cammi, R.; Pomelli, C.; Ochterski, J. W.; Martin, R. L.; Morokuma, K.; Zakrzewski, V. G.; Voth, G. A.; Salvador, P.; Dannenberg, J. J.; Dapprich, S.; Daniels, A. D.; Farkas, Ö.; Foresman, J. B.; Ortiz, J. V.; Cioslowski, J.; Fox, D. J. *Gaussian 09*, Revision B.01, Gaussian, Inc.: Wallingford, CT: 2009.

(95) Adamo, C.; Barone, V. *J. Chem. Phys.* **1998,** *108* (2), 664.

(96) Peterson, K. A. *J. Chem. Phys.* **2003,** *119* (21), 11099.

(97) Metz, B.; Stoll, H.; Dolg, M. *J. Chem. Phys.* **2000,** *113* (7), 2563.

(98) Glendening, E. D.; Badenhoop, J. K.; Reed, A. E.; Carpenter, J. E.; Bohmann, J. A.; Morales, C. M.; Weinhold, F. *NBO 5.9*, Theoretical Chemistry Institute, University of Wisconsin, Madison, WI, 2011.

(99) Manson, J.; Webster, C. E.; Pérez, L. M.; Hall, M. B., http://www.chem.tamu.edu/jimp2/index.html.

(100) Sheldrick, G. M. *SADABS, Version 2007/4*, Bruker Analytical X-ray Systems Inc.: Madison, Wisconsin, USA, 2007.

(101) *SAINT+*, Bruker Analytical X-ray Systems Inc.: Madison, Wisconsin, USA, 2000.

(102) Sheldrick, G. M. *SHELXTL, Version 6.1*, Bruker Analytical X-ray Systems Inc.: Madison, Wisconsin, USA, 2000.

(103) Boys, S. F. *Rev. Mod. Phys.* **1960,** *32* (2), 296.

(104) Guan, W.; Yamabe, S.; Sakaki, S. *Dalton Trans.* **2013,** *42* (24), 8717.

(105) Xu, S.; Li, X.; Zhang, S.; Sun, H. *Inorg. Chim. Acta* **2015,** *430*, 161.

(106) Hope, E. G.; Levason, W.; Powell, N. A. *Inorg. Chim. Acta* **1986,** *115* (2), 187.

(107) Oberhauser, W.; Bachmann, C.; Stampfl, T.; Brüggeller, P. *Inorg. Chim. Acta* **1997,** *256* (2), 223.

(108) Oberhauser, W.; Stampfl, T.; Bachmann, C.; Haid, R.; Langes, C.; Kopacka, H.; Ongania, K.-H.; Brüggeller, P. *Polyhedron* **2000,** *19* (8), 913.

(109) Yang, H.; Gabbaï, F. P. *J. Am. Chem. Soc.* **2014,** *136*, 10866.

(110) Ke, I.-S.; Jones, J. S.; Gabbaï, F. P. *Angew. Chem. Int. Ed.* **2014,** *53* (10), 2633.

(111) Wenschuh, E.; Wilhelm, D.; Hartung, H.; Baumeister, U. *Z. Anorg. Allg. Chem.* **1994,** *620* (12), 2048.

(112) Tskhovrebov, A.; Luzyanin, K.; Haukka, M.; Kukushkin, V. *J. Chem. Crystallogr.* **2012,** *42* (12), 1170.

(113) Levason, W.; Reid, G. *Coord. Chem. Rev.* **2006,** *250* (19+20), 2565.

(114) Lane, T. M.; Grubisha, D. S.; Hu, C.; Bennett, D. W. *J. Mol. Struct.* **1994,** *328* (0), 133.

(115) Sharutin, V. V.; Sharutina, O. K.; Pakusina, A. P.; Smirnova, S. A.; Pushilin, M. A. *Russ. J. Coord. Chem.* **2005,** *31* (2), 108.

(116) Chekhlov, A. N. *Dokl. Akad. Nauk* **1993,** *328* (2), 205.

(117) Robertson, A. P. M.; Burford, N.; McDonald, R.; Ferguson, M. J. *Angew. Chem. Int. Ed.* **2014,** *53* (13), 3480.

(118) Dammann, C. B.; Hughey, J. L.; Jicha, D. C.; Meyer, T. J.; Rakita, P. E.; Weaver, T. R. *Inorg. Chem.* **1973,** *12* (9), 2206.

(119) Chan, D. M. T.; Marder, T. B. *Angew. Chem. Int. Ed.* **1988,** *27* (3), 442.

(120) Fontaine, F.-G.; Boudreau, J.; Thibault, M.-H. *Eur. J. Inorg. Chem.* **2008,** *2008* (35), 5439.

(121) Braunschweig, H.; Dewhurst, R. D.; Schneider, A. *Chem. Rev.* **2010,** *110* (4), 3924.

(122) Bouhadir, G.; Amgoune, A.; Bourissou, D. *Adv. Organomet. Chem.* **2010,** *58*, 1.

(123) Amgoune, A.; Bourissou, D. *Chem. Commun.* **2011,** *47* (3), 859.

(124) Braunschweig, H.; Dewhurst, R. D. *Dalton Trans.* **2011,** *40*, 549.

(125) Bauer, J.; Braunschweig, H.; Dewhurst, R. D. *Chem. Rev.* **2012,** *112* (8), 4329.

(126) Owen, G. R. *Chem. Soc. Rev.* **2012,** *41* (9), 3535.

(127) Mingos, D. M. P. *J. Organomet. Chem.* **2014,** *751* (0), 153.

(128) Gutmann, V. *The Donor-Acceptor Approach to Molecular Interactions*. Plenum Press: New York, 1978.

(129) Beutner, G. L.; Denmark, S. E. *Top. Organomet. Chem.* **2013,** *44* (Inventing Reactions), 55.

(130) Bader, R. W. F. *Atoms in Molecules. A Quantum Theory*. Cambridge University Press: Oxford, UK, 1991.

(131) Bader, R. F. W.; Stephens, M. E. *J. Am. Chem. Soc.* **1975,** *97* (26), 7391.

(132) Cortés-Guzmán, F.; Bader, R. F. W. *Coord. Chem. Rev.* **2005,** *249* (5–6), 633.

(133) Frisch, M. J.; Trucks, G. W.; Schlegel, H. B.; Scuseria, G. E.; Robb, M. A.; Cheeseman, J. R.; Scalmani, G.; Barone, V.; Mennucci, B.; Petersson, G. A.; Nakatsuji, H.; Caricato, M.; Li, X.; Hratchian, H. P.; Izmaylov, A. F.; Bloino, J.; Zheng, G.; Sonnenberg, J. L.; Hada, M.; Ehara, M.; Toyota, K.; Fukuda, R.; Hasegawa, J.; Ishida, M.; Nakajima, T.; Honda, Y.; Kitao, O.; Nakai, H.; Vreven,

T.; Montgomery, J. A.; Peralta, J. E.; Ogliaro, F.; Bearpark, M.; Heyd, J. J.; Brothers, E.; Kudin, K. N.; Staroverov, V. N.; Kobayashi, R.; Normand, J.; Raghavachari, K.; Rendell, A.; Burant, J. C.; Iyengar, S. S.; Tomasi, J.; Cossi, M.; Rega, N.; Millam, J. M.; Klene, M.; Knox, J. E.; Cross, J. B.; Bakken, V.; Adamo, C.; Jaramillo, J.; Gomperts, R.; Stratmann, R. E.; Yazyev, O.; Austin, A. J.; Cammi, R.; Pomelli, C.; Ochterski, J. W.; Martin, R. L.; Morokuma, K.; Zakrzewski, V. G.; Voth, G. A.; Salvador, P.; Dannenberg, J. J.; Dapprich, S.; Daniels, A. D.; Farkas; Foresman, J. B.; Ortiz, J. V.; Cioslowski, J.; Fox, D. J. Gaussian 09, Revision B.01. Wallingford CT, 2009.

(134) Figgen, D.; Peterson, K. A.; Dolg, M.; Stoll, H. *J. Chem. Phys.* **2009,** *130* (16), 164108.

(135) Keith, T. A. *AIMAll (Version 14.06.21)*, TK Gristmill Software: Overland Park KS, USA, 2014.

(136) Wagler, J.; Hill, A. F.; Heine, T. *Eur. J. Inorg. Chem.* **2008,** *2008* (27), 4225.

(137) Wagler, J.; Brendler, E. *Angew. Chem. Int. Ed.* **2010,** *49* (3), 624.

(138) Gualco, P.; Lin, T.-P.; Sircoglou, M.; Mercy, M.; Ladeira, S.; Bouhadir, G.; Pérez, L. M.; Amgoune, A.; Maron, L.; Gabbaï, F. P.; Bourissou, D. *Angew. Chem. Int. Ed.* **2009,** *48* (52), 9892.

(139) Gualco, P.; Mercy, M.; Ladeira, S.; Coppel, Y.; Maron, L.; Amgoune, A.; Bourissou, D. *Chem. Eur. J.* **2010,** *16* (35), 10808.

(140) Lin, T.-P.; Gabbaï, F. P. *Angew. Chem. Int. Ed.* **2013,** *52* (14), 3864.

(141) Stephan, D. W.; Erker, G. *Angew. Chem. Int. Ed.* **2010,** *49* (1), 46.

(142) Kehr, G.; Schwendemann, S.; Erker, G. *Top. Curr. Chem.* **2013,** *332* (Frustrated Lewis Pairs I), 45.

(143) Stephan, D. W. *J. Am. Chem. Soc.* **2015,** *137* (32), 10018.

(144) Mundt, O.; Becker, G.; Stadelmann, H.; Thurn, H. *Z. Anorg. Allg. Chem.* **1992,** *617* (11), 59.

(145) Millington, P. L.; Sowerby, D. B. *J. Organomet. Chem.* **1994,** *480* (1), 227.

(146) Levason, W.; McAuliffe, C. A. *Inorg. Chim. Acta* **1974,** *11*, 33.

(147) Baenziger, N. C.; Bennett, W. E.; Soborofe, D. M. *Acta Crystallographica Section B* **1976,** *32* (3), 962.

(148) Jones, P. *Acta Crystallogr., Sect. C: Cryst. Struct. Commun.* **1992,** *48* (8), 1487.

(149) Jones, J. S.; Wade, C. R.; Gabbaï, F. P. *Angew. Chem. Int. Ed.* **2014,** *53* (34), 8876.

(150) Hall, M.; Sowerby, D. B. *J. Organomet. Chem.* **1988,** *347* (1), 59.

(151) Schmidbaur, H.; Schier, A. *Chem. Soc. Rev.* **2012,** *41* (1), 370.

(152) Bowmaker, G. A.; Dyason, J. C.; Healy, P. C.; Engelhardt, L. M.; Pakawatchai, C.; White, A. H. *J. Chem. Soc., Dalton Trans.* **1987,** (5), 1089.

(153) Sircoglou, M.; Bouhadir, G.; Saffon, N.; Miqueu, K.; Bourissou, D. *Organometallics* **2008,** *27* (8), 1675.

(154) Sircoglou, M.; Mercy, M.; Saffon, N.; Coppel, Y.; Bouhadir, G.; Maron, L.; Bourissou, D. *Angew. Chem. Int. Ed.* **2009,** *48* (19), 3454.

(155) Devillard, M.; Nicolas, E.; Appelt, C.; Backs, J.; Mallet-Ladeira, S.; Bouhadir, G.; Slootweg, J. C.; Uhl, W.; Bourissou, D. *Chem. Commun.* **2014,** *50* (94), 14805.

(156) Hashmi, A. S. K.; Hutchings, G. J. *Angew. Chem. Int. Ed.* **2006,** *45* (47), 7896.

(157) Pflasterer, D.; Hashmi, A. S. K. *Chem. Soc. Rev.* **2016,** *45* (5), 1331.

(158) Guérinot, A.; Fang, W.; Sircoglou, M.; Bour, C.; Bezzenine-Lafollée, S.; Gandon, V. *Angew. Chem. Int. Ed.* **2013,** *52* (22), 5848.

(159) Zhdanko, A.; Maier, M. E. *ACS Catalysis* **2015,** *5* (10), 5994.

(160) Ranieri, B.; Escofet, I.; Echavarren, A. M. *Org. Biomol. Chem.* **2015,** *13* (26), 7103.

(161) Hu, X.; Martin, D.; Bertrand, G. *New J. Chem.* **2016,** *40* (7), 5993.

(162) Wegener, M.; Huber, F.; Bolli, C.; Jenne, C.; Kirsch, S. F. *Chem. Eur. J.* **2015,** *21* (3), 1328.

(163) Fang, W.; Presset, M.; Guérinot, A.; Bour, C.; Bezzenine-Lafollée, S.; Gandon, V. *Chem. Eur. J.* **2014,** *20* (18), 5439.

(164) Fang, W.; Presset, M.; Guerinot, A.; Bour, C.; Bezzenine-Lafollee, S.; Gandon, V. *Organic Chemistry Frontiers* **2014,** *1* (6), 608.

(165) Smirnova, E. S.; Echavarren, A. M. *Angew. Chem. Int. Ed.* **2013,** *52* (34), 9023.

(166) Fisher, S. P.; El-Hellani, A.; Tham, F. S.; Lavallo, V. *Dalton Trans.* **2016,** *45* (24), 9762.

(167) Bastin, S.; Barthes, C.; Lugan, N.; Lavigne, G.; César, V. *Eur. J. Inorg. Chem.* **2015,** *2015* (13), 2216.

(168) Kronig, S.; Theuergarten, E.; Daniliuc, C. G.; Jones, P. G.; Tamm, M. *Angew. Chem. Int. Ed.* **2012,** *51* (13), 3240.

(169) Hornberger, K. R.; Hamblett, C. L.; Leighton, J. L. *J. Am. Chem. Soc.* **2000,** *122* (51), 12894.

(170) Wipf, P.; Graham, T. H. *J. Am. Chem. Soc.* **2004,** *126* (47), 15346.

(171) Hashmi, A. S. K.; Weyrauch, J. P.; Frey, W.; Bats, J. W. *Org. Lett.* **2004,** *6* (23), 4391.

(172) Milton, M. D.; Inada, Y.; Nishibayashi, Y.; Uemura, S. *Chem. Commun.* **2004,** (23), 2712.

(173) Weyrauch, J. P.; Hashmi, A. S. K.; Schuster, A.; Hengst, T.; Schetter, S.; Littmann, A.; Rudolph, M.; Hamzic, M.; Visus, J.; Rominger, F.; Frey, W.; Bats, J. W. *Chem. Eur. J.* **2010,** *16* (3), 956.

(174) Oliver-Meseguer, J.; Cabrero-Antonino, J. R.; Domínguez, I.; Leyva-Pérez, A.; Corma, A. *Science* **2012,** *338* (6113), 1452.

(175) Anton, D. R.; Crabtree, R. H. *Organometallics* **1983,** *2* (7), 855.

(176) Widegren, J. A.; Finke, R. G. *J. Mol. Catal. A: Chem.* **2003,** *198* (1–2), 317.

(177) Uson, R.; Laguna, A.; Laguna, M.; Briggs, D. A.; Murray, H. H.; Fackler, J. P. (Tetrahydrothiophene)Gold(I) or Gold(III) Complexes. In *Inorg. Synth.*, John Wiley & Sons, Inc.: 2007; pp 85.

(178) Adamo, C.; Barone, V. *J. Chem. Phys.* **1999,** *110* (13), 6158.

(179) DesEnfants Ii, R. E.; Gavney Jr, J. A.; Hayashi, R. K.; Rae, A. D.; Dahl, L. F.; Bjarnason, A. *J. Organomet. Chem.* **1990,** *383* (1–3), 543.

(180) Malisch, W.; Panster, P. *Angew. Chem. Int. Ed.* **1974,** *13* (10), 670.

(181) Ke, I.-S.; Jones, J. S.; Gabbaï, F. P. *Angew. Chem. Int. Ed.* **2014,** *53*, in press.

(182) Wade, C. R.; Gabbaï, F. P. *Angew. Chem. Int. Ed.* **2011,** *50*, 7369.

(183) Garrou, P. E. *Chem. Rev.* **1981,** *81* (3), 229.

(184) Tsay, C.; Peters, J. C. *Chem. Sci.* **2012,** *3* (4), 1313.

(185) CCDC 995209 (**1**-Et_2O), 995210 (**2**), 995211 (**3**-0.5 C_6H_6) and 995212 (**4**-3.5 C_6H_6) contain the supplementary crystallographic data for this paper. These data can be obtained free of charge from The Cambridge Crystallographic Data Centre via www.ccdc.cam.ac.uk/data_request/cif.

(186) Fox, B. J.; Millard, M. D.; DiPasquale, A. G.; Rheingold, A. L.; Figueroa, J. S. *Angew. Chem. Int. Ed.* **2009,** *48* (19), 3473.

(187) Bontemps, S.; Sircoglou, M.; Bouhadir, G.; Puschmann, H.; Howard, J. A. K.; Dyer, P. W.; Miqueu, K.; Bourissou, D. *Chem. Eur. J.* **2008,** *14* (2), 731.

(188) Kameo, H.; Nakazawa, H. *Organometallics* **2012,** *31* (21), 7476.

(189) Bond, G. C. *Platinum Met. Rev.* **2000,** *44* (4), 146.

(190) Lin, T.-P.; Nelson, R. C.; Wu, T.; Miller, J. T.; Gabbaï, F. P. *Chem. Sci.* **2012,** *3*, 1128.

(191) Sircoglou, M.; Bontemps, S.; Bouhadir, G.; Saffon, N.; Miqueu, K.; Gu, W.; Mercy, M.; Chen, C.-H.; Foxman, B. M.; Maron, L.; Ozerov, O. V.; Bourissou, D. *J. Am. Chem. Soc.* **2008,** *130* (49), 16729.

(192) Brendler, E.; Wächtler, E.; Heine, T.; Zhechkov, L.; Langer, T.; Pöttgen, R.; Hill, A. F.; Wagler, J. *Angew. Chem. Int. Ed.* **2011,** *50*, 4696.

(193) Ittel, S. D.; Berke, H.; Dietrich, H.; Lambrecht, J.; Härter, P.; Opitz, J.; Springer, W. Complexes of Nickel(0). In *Inorg. Synth.*, John Wiley & Sons, Inc.: 2007; pp 98.

(194) Zhao, X.-F.; Zhang, C. *Synthesis* **2007,** (4), 551.

(195) Petersson, G. A.; Bennett, A.; Tensfeldt, T. G.; Al-Laham, M. A.; Shirley, W. A.; Mantzaris, J. *J. Chem. Phys.* **1988,** *89* (4), 2193.

(196) Kendall, R. A.; Dunning, T. H.; Harrison, R. J. *J. Chem. Phys.* **1992,** *96* (9), 6796.

(197) Peterson, K. A. *J. Chem. Phys.* **2003,** *119* (21), 11099.

(198) Metz, B.; Stoll, H.; Dolg, M. *J. Chem. Phys.* **2000,** *113* (7), 2563.

(199) Glendening, E. D.; Badenhoop, J. K.; Reed, A. E.; Carpenter, J. E.; Bohmann, J. A.; Morales, C. M.; Weinhold, F. *NBO 5.9*, Theoretical Chemistry Institute.

(200) Jørgensen, C. K. *Coord. Chem. Rev.* **1966,** *1* (1), 164.

(201) Kaim, W.; Schwederski, B. *Coord. Chem. Rev.* **2010,** *254* (13–14), 1580.

(202) Chirik, P. J. *Inorg. Chem.* **2011,** *50* (20), 9737.

(203) Kaim, W. *Inorg. Chem.* **2011,** *50* (20), 9752.

(204) Chirik, P. J.; Wieghardt, K. *Science* **2010,** *327* (5967), 794.

(205) Luca, O. R.; Crabtree, R. H. *Chem. Soc. Rev.* **2013,** *42* (4), 1440.

(206) Eisenberg, R.; Gray, H. B. *Inorg. Chem.* **2011,** *50* (20), 9741.

(207) Eisenberg, R. *Coord. Chem. Rev.* **2011,** *255* (7–8), 825.

(208) Sproules, S.; Wieghardt, K. *Coord. Chem. Rev.* **2011,** *255* (7–8), 837.

(209) Jones, J. S.; Wade, C. R.; Gabbaï, F. P. *Organometallics* **2015,** *34* (11), 2647.

(210) Chao, S. T.; Lara, N. C.; Lin, S.; Day, M. W.; Agapie, T. *Angew. Chem. Int. Ed.* **2011,** *50* (33), 7529.

(211) Ni, Z.; McDaniel, A. M.; Shores, M. P. *Chem. Sci.* **2010,** *1* (5), 615.

(212) Riis-Johannessen, T.; Schenk, K.; Severin, K. *Inorg. Chem.* **2010,** *49* (20), 9546.

(213) Riis-Johannessen, T.; Severin, K. *Chem. Eur. J.* **2010,** *16* (28), 8291.

(214) Ke, I. S. Organoantimony Lewis Acids as Fluoride Receptors and Ligands Towards Transition Metals. Texas A&M University, College Station, TX, 2013.

(215) Cordero, B.; Gomez, V.; Platero-Prats, A. E.; Reves, M.; Echeverria, J.; Cremades, E.; Barragan, F.; Alvarez, S. *Dalton Trans.* **2008,** (21), 2832.

(216) Hall, M.; Sowerby, D. B. *J. Am. Chem. Soc.* **1980,** *102* (2), 628.

(217) Fukin, G. K.; Zakharov, L. N.; Domrachev, G. A.; Fedorov, A. Y.; Zaburdyaeva, S. N.; Dodonov, V. A. *Russ. Chem. Bull.* **1999,** *48* (9), 1722.

(218) Hirai, M.; Gabbaï, F. P. *Angew. Chem. Int. Ed.* **2015,** *54* (4), 1205.

(219) Rheingold, A. L.; Doerrer, L. H.; Lum, J. S. Private communication to the Cambridge Structural Database, deposition number 651013, 2004.

(220) Scriban, C.; Glueck, D. S.; Golen, J. A.; Rheingold, A. L. *Organometallics* **2007,** *26* (7), 1788.

(221) Karplus, M. *J. Chem. Phys.* **1959,** *30* (1), 11.

(222) Karplus, M. *J. Am. Chem. Soc.* **1963,** *85* (18), 2870.

(223) Crespo, M.; Sales, J.; Solans, X.; Altaba, M. F. *J. Chem. Soc., Dalton Trans.* **1988,** (6), 1617.

(224) Khanna, A.; Khandelwal, B. L.; Saxena, A. K.; Singh, T. P. *Polyhedron* **1995,** *14* (19), 2705.

(225) Albrecht, M.; Rodríguez, G.; Schoenmaker, J.; van Koten, G. *Org. Lett.* **2000,** *2* (22), 3461.

(226) Conzelmann, W.; Koola, J. D.; Kunze, U.; Strähle, J. *Inorg. Chim. Acta* **1984,** *89* (2), 147.

(227) Silvestru, C.; Rösler, R.; Haiduc, I.; Toscano, R. A.; Sowerby, D. B. *J. Organomet. Chem.* **1996,** *515* (1), 131.

(228) Becke, A. D. *Phys. Rev. A* **1988,** *38* (6), 3098.

(229) Perdew, J. P. *Phys. Rev. B* **1986,** *33* (12), 8822.

(230) Figgen, D.; Peterson, K. A.; Dolg, M.; Stoll, H. *J. Chem. Phys.* **2009,** *130* (16), 164108.

(231) Marenich, A. V.; Cramer, C. J.; Truhlar, D. G. *The Journal of Physical Chemistry B* **2009,** *113* (18), 6378.

(232) Lee, S.; Flood, A. H. *J. Phys. Org. Chem.* **2013,** *26* (2), 79.

(233) Klán, P.; Šolomek, T.; Bochet, C. G.; Blanc, A.; Givens, R.; Rubina, M.; Popik, V.; Kostikov, A.; Wirz, J. *Chem. Rev.* **2013,** *113* (1), 119.

(234) Razuvaev, G.; Razuvaev. *Doklady Akademii nauk SSSR* **1970,** *193* (2), 355.

(235) Schwartsburd, L.; Poverenov, E.; Shimon, L. J. W.; Milstein, D. *Organometallics*